A Search for Young Galactic Supernova Remnants

Zdenka Misanovic

A thesis
submitted for the degree of
Master of Science
at the
University of Sydney

April, 2001

Abstract

A sample of 9 small-diameter radio sources has been selected from the Molonglo Galactic Plane Survey (MGPS) and observed with the Australia Telescope Compact Array (ATCA) in the radio recombination line (RRL) at 5 GHz, in a search for young Galactic SNRs. Since the RRL emission is an unambiguous indicator of a thermal source, this method has been used to eliminate HII regions from the selected sample. In addition, the IRAS and MSX infrared data and spectral index measurements have been combined with the RRL studies to distinguish thermal and non-thermal sources in the selected sample.

One source (G282.8-1.2) is identified here as a possible new young Galactic supernova remnant, based on its relatively weak infrared emission, steep radio spectrum and possible x-ray emission. However, the ATCA data are inconclusive and further studies are needed to confirm this result.

Radio recombination line emission (H107α) has been detected in 3 of the selected sources, eliminating them from the sample of SNR candidates. In addition, the parameters of the RRL emission from the identified HII regions have been used to estimate their properties.

The RRL data are inconclusive for the remaining low brightness, extended sources in the sample. However, some of these sources are likely to be thermal HII regions according to the infrared and spectral index data.

The selected method for distinguishing thermal and non-thermal Galactic radio sources seems promising. The selected ATCA configuration was appropriate for imaging relatively bright, compact sources, but a slightly modified observing technique is needed to successfully image low surface brightness, extended sources.

Preface

Acknowledgements

The list of people I wish to thank starts with my supervisor, Lawrence Cram, who made a major contribution by providing the initial idea for this project. I would also like to thank him for many helpful discussions about all aspects of the project, and comments on the drafts of the thesis. His help and advice were invaluable during this project.

I am also grateful to Anne Green and Dick Hunstead for particularly helpful discussions and for reading the drafts (at a short notice). I really appreciate their assistance and advice.

I would also like to thank Bob Sault from the ATNF who made helpful suggestions about ATCA data reduction.

The staff and students of the Department of Astrophysics have all been helpful. I would, especially like to thank Julia Bryant for help with many practical things and helpful advice, and also David Blank for reading the parts of the thesis.

The selection of objects for this project, and the ATCA observations were made by Dr Anne Green and Professor Lawrence Cram.

The reduction and analysis of radio data were made using MIRIAD software. A computer program for calculating the Galactic distances was provided by Anne Green.

The Molonglo Observatory Synthesis Telescope is funded by the Australian Research Council and the Science Foundation for Physics. The Australia Telescope is operated in association with the Division of Radiophysics by the CSIRO.

Statement of Originality

This thesis describes work carried out in the Department of Astrophysics at the University of Sydney. The content describes entirely my own work except where duly acknowledged. None of the work has been presented for any previous degree.

Zdenka Misanovic

Astronomical Units

For consistency with much of the published work in astronomy, the following non-SI units are used in this thesis:

- The parsec (pc):

$$1\,\mathrm{pc} = 3.086 \times 10^{16}\,\mathrm{m} \tag{0.1}$$

- The solar mass ($\mathrm{M}_\odot$):

$$1\,\mathrm{M}_\odot = 1.989 \times 10^{30}\,\mathrm{kg} \tag{0.2}$$

Contents

1 Searches for Young Galactic Supernova Remnants **1**

1.1 Supernova explosions in the Galaxy 2
1.1.1 Brief summary of supernovae 2
1.1.2 Estimates of the supernova rate in our Galaxy 3
1.2 Young supernova remnants 5
1.2.1 Young SNRs and the interstellar medium 5
1.2.2 Radio emission from young SNRs 7
1.2.3 The historical supernova remnants 9
1.3 Searching for young SNRs 12
1.3.1 Previous searches 12
1.3.2 Challenges and problems of searching for young SNRs 13
1.4 Distinguishing SNRs and HII regions by FIR/radio ratio 15
1.5 Distinguishing SNRs and HII regions by MIR/radio ratio 16
1.6 Distinguishing HII regions from SNRs by detecting RRL emission . . 17
1.6.1 HII regions 17
1.6.2 Photoionisation structure of HII regions 18
1.6.3 Radio continuum emission from HII regions 18
1.6.4 RRL emission from HII regions 19
1.6.5 Line to continuum ratio 21
1.6.6 Line intensity under non-LTE conditions 21
1.7 Scope of this thesis 23
1.7.1 Aim, method, and source selection 23
1.7.2 Thesis outline 24

2 Observations **27**

2.1 843 MHz continuum data 28
2.2 60 μm infrared data 28
2.2.1 Identification with far-infrared counterparts 29
2.3 8.3 μm infrared data 33
2.4 The ATCA radio continuum and spectral line data 33
2.4.1 Line to continuum ratio 37
2.4.2 Sensitivity 37

2.4.3 Largest angular scale 39
2.4.4 Imaging 40
2.5 Possible x-ray identifications 41

3 Results and Discussion **43**
3.1 843 MHz flux densities and sizes 43
3.2 FIR to radio ratio 43
3.3 MIR to radio ratio 45
3.4 Continuum and line emission at 5 GHz 46
3.5 Properties of the sources with detected line emission 46
3.6 Individual sources 48
3.6.1 G267.9-1.1 48
3.6.2 G282.8-1.2 50
3.6.3 G302.4-0.1 53
3.6.4 G304.5-0.1 56
3.6.5 G313.8+0.7 59
3.6.6 G323.8+0.0 62
3.6.7 G331.7-0.1 65
3.6.8 G337.4-0.4 68
3.6.9 G358.6+0.1 (SgrE19) 72
3.7 The experimental design 75

4 Conclusion and suggestions for further work **77**

Bibliography **79**

A RRL emission from HII regions **85**
A.1 Equation of radiative transfer 85
A.2 Rayleigh-Jeans law and the brightness temperature 86
A.3 Equation of radiative transfer for line emission 86
A.4 Line intensity under conditions of LTE 87
A.5 Line intensity under non-LTE conditions 88

List of Tables

1.1 The remnants of historical supernovae 9
1.2 Ratio of infrared to radio emission for HII regions and SNRs 16
1.3 Galactic and Equatorial coordinates of the ATCA pointings 24

2.1 Parameters of the ATCA observations 39
2.2 The calibrators 40

3.1 Flux densities and sizes of the selected sources at 843 MHz 44
3.2 The IRAS infrared data of the selected sources at 60 μm. 44
3.3 The MSX infrared data of the selected sources at 8.3 μm. 45
3.4 Flux densities of continuum and H107α emission 46
3.5 Properties of the sources with detected line emission 47

List of Figures

1.1 Observational manifestations of a young SNR 6
1.2 A schematic representation of a typical HII region 19
1.3 Theoretical line to continuum ratios for model HII regions 22
1.4 One of the MGPS mosaics 25

2.1 G267.9-1.1 overlaid on the IRAS source 08573-4718 30
2.2 The IRAS 60 μm image of G282.8-1.2 30
2.3 G302.4-0.1 overlaid on the IRAS source 12440-6242 31
2.4 G313.8+0.7 overlaid on the IRAS source 14170-6002 31
2.5 G323.8+0.0 overlaid on the IRAS source 15272-560 32
2.6 G337.4-0.4 overlaid on the IRAS source 16352-4721 32
2.7 G282.8-1.2 overlaid on the MSX grayscale image 34
2.8 G302.4-0.1 overlaid on the MSX grayscale image 34
2.9 G304.5-0.1 overlaid on the MSX grayscale image 35
2.10 G323.8+0.0 overlaid on the MSX grayscale image 35
2.11 G337.4-0.4 overlaid on the MSX grayscale image 36
2.12 SgrE19 overlaid on the MSX grayscale image 36

3.1 The MOST image of G267.9-1.1 49
3.2 Integrated spectrum of G267.9-1.1 49
3.3 The MOST image of G282.8-1.2 51
3.4 The ATCA image of G282.8-1.2 52
3.5 Integrated spectrum of G282.8-1.2 52
3.6 The MOST image of G302.4-0.1 54
3.7 The ATCA image of G302.4-0.1 55
3.8 Integrated spectrum of G302.4-0.1 55
3.9 The MOST image of G304.5-0.1 57
3.10 The ATCA image of G304.5-0.1 58
3.11 Integrated spectrum of G304.5-0.1 58
3.12 The MOST image of G313.8+0.7 60
3.13 The ATCA image of G313.8+0.7 61
3.14 Integrated spectrum of G313.8+0.7 61
3.15 The MOST image of G323.8+0.0 63
3.16 The ATCA image of G323.8+0.0 64
3.17 Integrated spectrum of G323.8+0.0 64

3.18 The MOST image of G331.7-0.1 66
3.19 The ATCA image of G331.7-0.1 66
3.20 Integrated spectrum of G331.7-0.1 67
3.21 Spectrum of G331.7-0.1 with a 2σ detection 67
3.22 The MOST image of G337.4-0.4 69
3.23 The ATCA image of G337.4-0.4 69
3.24 The ATCA image of G337.4-0.4 overlaid on the MOST radio contours of G337.4-0.4 70
3.25 The ATCA image of G337.4-0.4 convolved with the MOST beam . . 70
3.26 Integrated spectrum of G337.4-0.4 71
3.27 The MOST image of SgrE19 73
3.28 The ATCA image of SgrE19 74
3.29 Integrated spectrum of SgrE19 74

Chapter 1

Searches for Young Galactic Supernova Remnants

Supernova (SN) explosions mark the violent endpoints of stellar evolution. The ejected material from the exploded star expands in a shell around the progenitor, interacting with the interstellar medium (ISM). The ejecta continue to expand for thousands of years as a supernova remnant (SNR) until it incorporates into the surrounding ISM.

Young remnants, which have been observed throughout the electromagnetic spectrum, occupy a special place in studies of stellar explosions and their influence on the ISM. However, a number of young SNRs in our Galaxy apparently remains undiscovered. According to various authors there should be between 20 - 50 SNRs younger than 1000 years, but only a fraction of these have been identified despite many searches.

The explosions of 6 nearby, optically bright SNe (known as historical) had been seen and recorded in the past 1000 years (Clark and Stephenson 1977) [26], while those further away had probably been obscured by the dusty ISM in the Galactic disk.

By studying the historical SNRs and a number of detected extragalactic SNe it has been established that young SNRs are non-thermal radio sources and that radio emission can be detected from SNRs with ages in excess of 100-300 years (Weiler and Sramek 1988 [120], Brown and Marscher 1978 [15]). Furthermore, radio emission from some extragalactic SNe had been detected only several years after the initial outburst (eg. from SN1987A, Staveley-Smith et al. 1992 [101]). Hence, many radio searches have been conducted to identify these missing young but distant Galactic SNRs from samples of compact small-diameter radio sources in the Galactic plane. Various methods have been used in these searches to distinguish young SNRs from other discrete components of the Galactic radio source population (eg. HII regions). However, the most recent catalogues of SNRs are still incomplete with respect to small-diameter SNRs (Green 2000 [48], Whiteoak and Green 1996 [126]), and the search for young Galactic SNRs remains an important theme in SNR research.

This chapter summarises current observational data and theoretical models on

young SNRs, including the discussion about the Galactic SN rate and the methods and results of previous searches for young Galactic SNRs. A short overview of the theory of radio recombination line emission, which is used here to distinguish HII regions and SNRs is also included.

1.1 Supernova explosions in the Galaxy

1.1.1 Brief summary of supernovae

The explosion of a supernova marks either the complete disruption of a star or the ejection of its outer layers as its core collapses, due to the loss of thermal and mechanical stability at the endpoint of stellar evolution. The matter thrown off expands into gas that left the surface of the progenitor at some previous stage of development, sweeping it up and communicating the energy of the explosion to the surrounding medium (Lozinskaya 1992) [69].

The classification of supernovae is based on spectral features, light curves, and luminosity near maximum light. However, this classification scheme is not purely phenomenological but gives an insight into the relationship between SN type and its precursor and the physical processes occurring during the outburst.

The first SN classification, proposed by Minkowski and in use until 1985, was based on the presence (SN I) or absence (SN II) of hydrogen lines in the spectrum near maximum light. The large variations in the light curves and spectra and the spread in luminosity within a single type suggested further separation of SNs (Shklovskii 1984 [97], Oemler and Tinsley 1979 [76]) and a new system of classification was introduced, with three types of supernovae: SN Ia, SN Ib, and SN II.

This new classification scheme is again based manly on spectral features - SN Ib are characterised by the absence of Si II absorption at $\lambda = 615$ nm near maximum light (Bertola et al. 1965) [8]. In the later stages spectra of SN Ia are dominated by lines of Fe II, while lines of O I dominate the spectra of SN Ib (Gaskell et al. 1986) [39]. In addition, SN Ib are weaker and redder than SN Ia, showing strong non-thermal radio emission near optical maximum (Lozinskaya 1992) [69].

Analyses of the spectra and light curves of various SN types have been used to propose the models for their progenitor stars and outburst evolution. For example, SN Ia are believed to be the results of the detonation of white dwarfs - low-mass degenerate stars that have lost their external hydrogen layers in the process of evolution. The progenitors of the SN Ib are most probably more massive stars, also without the hydrogen layers, which can be in a binary system with a supergiant companion. An explosion of a supergiant, which retained its outer hydrogen layers up to the moment of explosion, will produce a type II supernova (Lozinskaya 1992) [69].

This present classification scheme is not entirely definite as there remain anomalous and unclassified objects.

1.1.2 Estimates of the supernova rate in our Galaxy

The Galactic supernova rate has been determined by observations of extragalactic supernovae, by studying distribution of young supernova remnants within our Galaxy - the remnants of so-called "historical" supernovae, and by counting non-thermal radio sources in the Galaxy. Supernova rates are quoted per unit galactic luminosity or per unit galactic mass, since the number of SN outbursts is correlated with galactic mass and luminosity (Lozinskaya 1992) [69].

Various limitations are imposed on the statistical studies of SNRs, their distribution and birthrates. Firstly there are significant selection effects that apply to current SNR catalogues, and secondly, SNRs show a wide range of intrinsic properties so that "average" properties, derived from statistical studies, may be inappropriate.

SN rate from the distribution of extragalactic supernovae

The mean interval between supernova outbursts in our Galaxy can be determined from the distribution of extragalactic supernovae in galaxies of different morphological types. To estimate the SN rate in the Milky Way Galaxy from external galaxy rates requires knowledge of the spiral classification and luminosity of our Galaxy.

To determine the rate of SN in galaxies of different morphological types it is necessary to consider various selection effects, which corrupt the observed distribution of supernovae. In addition to general astronomical selection effects (completeness of the sample depending on the limit of detectability), there are observational biases peculiar to supernovae. For example, it is necessary to correct observations for the inclination to the line of sight of spiral galaxies. This is due to the fact that most SNe are concentrated in the galactic plane which reduces detectability of supernovae in edge-on spirals. This and other selection effects have been discussed by Tammann (1977 [106], 1982 [107]), van den Bergh and Maza (1976) [113], Shklovskii (1976) [96], and others.

Systematic searches for extragalactic SNe have detected several hundreds outbursts in galaxies of different morphological types:

- **Tammann 1982 [107]:** in the period of 1960-1976, a total of 77 supernovae was detected in a sample of 400 galaxies from the Shapley-Ames catalogue. In addition 173 SN were detected in a sample of 2955 galaxies from the list of Vaucouleurs et al. 1976.
- **Cappellaro and Turatto 1988 [16]:** a total of 51 SN have been discovered from 1959 to 1988 in 736 galaxies from the catalogue of Vaucouleurs (1976).
- **van den Bergh et al. 1987 [114]:** a total of 15 SN discovered from visual observations of 1017 galaxies by Evans, in the period of 1980-1985.
- **Cappellaro et al. 1993 [17]:** a total of 65 SNe detected by analysing data for 2461 searched galaxies.
- **Tammann et al. 1994 [108]:** A total of 96 known SNe have been analysed from the selected 330 galaxies with reliably known parameters.

From these samples of the detected extragalactic SNe it was found that SNe of all types occur in spiral galaxies, with the SN II rate approximately equal to the overall type I rate. Type II supernovae are found to be correlated with HII regions and occur primarily in spiral arms suggesting that their progenitors are short-lived massive stars. Type Ib also occur in spiral arms, while Ia supernovae are evenly distributed throughout the disk of their host galaxy (Lozinskaya 1992 [69], Tammann 1982 [107]).

Analysing these extragalactic SN rates, it is possible to predict the mean interval between supernovae outbursts in a galaxy with known mass and luminosity with an uncertainty of at most 50 percent (Lozinskaya 1992) [69]. Extrapolation of these estimates for our own Galaxy ($L = 2 \times 10^{10} L_{B_\odot}$) the number of SN Ia, SN Ib and SN II per 100 years was calculated to be $0.6h^2$, $0.8h^2$, and $1.2h^2$, respectively[1] (van den Bergh et al. 1987 [114]). For $h = 0.75$ the predicted total number of SN in the Galaxy is about two per century (the mean interval between outbursts is $\tau = 50$ years) which is in agreement with the result of Cappellaro and Turatto (1988) [16]. Similarly, using the extragalactic SN rate, Tammann et al. (1994) [108] has calculated that our Galaxy should be producing 4 SNe per century, while Cappellaro et al. (1993) [17] calculated a Milky Way rate of 1 - 3 SNe per 100 years.

SN rate from the distribution of young SNRs in our Galaxy

Only six SNe have been observed in our Galaxy in the last 1000 years. These are known as "historical supernovae". Remnants of the historical supernovae have been observed and studied and their distances from the Sun have been determined. All historical SNe are closer than 5 kpc to the Sun and they occupy a wedge-shaped sector of the Galactic disk with an apex angle of 50°. Using the radial distribution of SN in spiral galaxies (eg. Tammann 1982) [107] it is possible to estimate how many unobserved SN there may have been in the same sector but more than 5 kpc from the Sun.

Using this method Tammann (1982) [107] has found that there have been approximately 60 Galactic SNe in the last thousand years (the mean interval between SN explosions is $\tau = 16$ years). Using the same argument Shklovskii (1960) [95] has obtained $\tau = 60$ years, Pskovskii (1978) [78] $\tau = 50 - 100$ years, and Clark and Stephenson (1977) [26] $\tau = 10 - 15$ years. The differences among the various authors are the result of using different corrections for the observational selection effects (Lozinskaya 1992) [69].

SN rate from the counts of non-thermal radio sources

Milne (1970) [75] has introduced a method to estimate the Galactic SN rate through counts of non-thermal radio sources (remnants). According to Milne, the mean time

[1] $h = H/100$ kms^{-1}/Mpc, and H is the Hubble constant.

between SN explosions τ can be calculated from:

$$N(< D) = t(D)/\tau, \tag{1.1}$$

where $N(< D)$ is the number of remnants with diameter less than D, and $t(D)$ is the age of a shell of diameter D. Calculating $t(D)$ using the standard adiabatic model, various authors found τ to be 35 years (Downes 1971) [32], 150 years (Clark and Caswell 1976) [24], and 25 years (Mills et al. 1984) [74].

Lozinskaya (1992) [69] has suggested that the estimate of τ, obtained from counts of non-thermal radio-sources, has been affected by the large scale fluctuations in the Galactic disk density. A large fraction of the Galactic disk is filled with hot, tenuous gas, in which a SNR lasts longer according to the adiabatic model. Applying this correction, Lozinskaya (1992) [69] has found $\tau = 25 - 30$ years, a value consistent with the rate extrapolated from the extragalactic SN rate.

Conclusion

The combined evidence from external galaxies, from the observed historical SNe in our Galaxy, and from the estimated number of radio remnants gives an estimate of the Galactic SN frequency of one event every 20-50 years, or 2-5 SNe per century. That means that there should be 20-50 SNRs in our Galaxy that are younger than 1000 years. Only six of these had been seen in the past and recorded in old historical manuscripts.

The last supernova to be observed in our Galaxy appeared nearly four centuries ago. Clark, Andrews, and Smith (1981) [23] showed that the estimated total rate of 1 SN every 20 years is consistent with local detection rate of 6-7 SN in the last 1000 years in the Sun neighbourhood. They modelled SNe as random events in the Galaxy and determined local rate of detection allowing for light travel time. For a constant rate of 1 SN every 20 years, the local detection rate per millennium peaked at about 7, but fluctuated from 2 to 15.

1.2 Young supernova remnants

1.2.1 Young SNRs and the interstellar medium

Young SNRs are observed to have complex structures, and there are marked differences between them. It is believed that these differences and the complexity of their structures reflect the interaction between the ejected matter and asymmetric, possibly clumpy structures in the stellar wind and interstellar medium around the exploded star.

Figure 1.1 shows a model of a young SNR based on the current observational data (Lozinskaya 1992) [69]. The matter ejected in the SN explosion expands into the ambient gas, consisting of the ISM and the circumstellar material (CSM) that left the surface of the progenitor at some previous stage. This process is accompanied by two

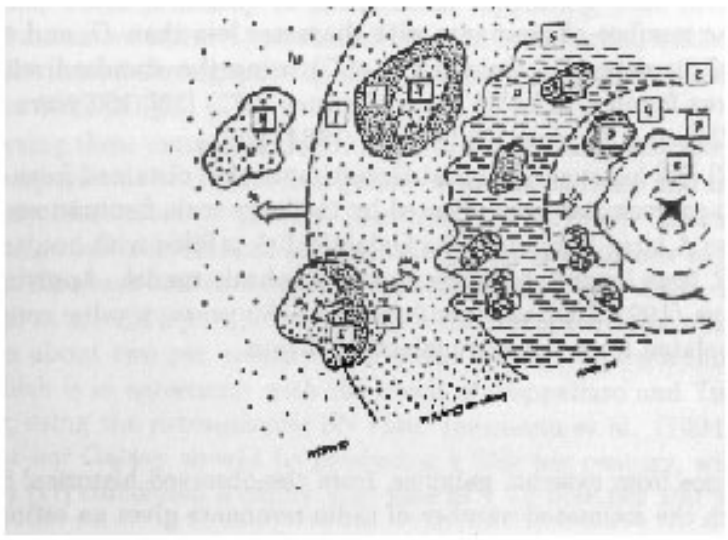

Figure 1.1 Observational manifestations of a young SNR in different spectral ranges (Lozinskaya 1992) [69].

shock waves - the blast wave (1) that propagates outward into the surrounding gas at velocity v_s, and the reverse shock (2) moving back inward through the expanding ejecta with velocity v_r. A secondary shock wave (3) moving into a dense cloud with a velocity v_{cl}, and a shock reflected into the intercloud gas (4) are the results of the inhomogeneity of the ISM/CSM. A connective layer (5) forms at the contact discontinuity between the swept-up gas and the SN ejecta due to Rayleigh-Taylor instability. For SNRs with a pulsar there is also a contact discontinuity (6) between the SN ejecta and a cloud of relativistic particles and magnetic field produced by the pulsar.

The model of a young SNR shown in Figure 1.1 can explain the mechanisms for radiation at different spectral ranges (McKee and Cowie 1975 [71], Sgro 1975 [91]). According to the model, thermal x-ray emission is produced by the swept-up gas heated by the blast wave (i), and by the ejecta heated by the reverse shock (d). Optical emission emerges from dense clumps of ejecta (e) heated by the reverse shock, and from dense ambient clouds heated by the secondary shock wave (j). Synchrotron radio emission with shell-like morphology is generated by relativistic electrons accelerated by the blast wave and moving in the magnetic field produced at the contact discontinuity (5). The source of infrared radiation from young SNRs is ejected and swept-up dust heated by hot x-ray plasma. Synchrotron x-ray and optical radiation may also be produced by SNRs with a pulsar (a).

1.2.2 Radio emission from young SNRs

All young Galactic SNRs (historical) were observed to be non-thermal radio sources. However, since these Galactic remnants are older than 300 years the properties of radio emission of much younger remnants can only be studied by observing young extragalactic SNRs.

By observing a number of young extragalactic SNe it was found that their explosions were accompanied by outbursts of radio emission which gradually declined over a period of a few weeks or months (Weiler and Sramek 1988 [120], while some SNe remain radio emitters for at least several years after optical maximum (Cowan et al. 1991).

However, it has been suggested that radio emission from very young remnants remains intrinsically weak for up to 100 years (Brown and Marscher 1978) [15], but observations of SN 1987A detected radio emission from this young remnant only 3.5 years after the initial outburst (Staveley-Smith et al. 1992 [101]).

It is believed that synchrotron emission from young SNRs is produced by relativistic electrons moving in a magnetic field. According to the theory of synchrotron emission one electron produces radiation in a series of harmonics of its cyclotron frequency around a magnetic field line. These harmonics will be smeared into a continuum with the frequency of peak emission depending on the energy of the electron. A collection of electrons with a power low distribution in energy, $N(E) = CE^{-\gamma}$, will then produce a continuum radiation with a power law spectrum of the form:

$$S_\nu \propto \nu^\alpha \tag{1.2}$$

where S_ν is the observed flux density at frequency ν, and the power α is called the spectral index where $\alpha = -(\gamma - 1)/2$. The origin of the magnetic field and source of acceleration of the electrons is still not entirely explained. However, there are some mechanisms that can account for the generation of synchrotron radio emission from some types of SNRs, at some stages of their evolution.

Most SNRs in our and other galaxies have been identified from the catalogues of non-thermal radio sources (Green 1988 [45], Mathewson et al. 1985 [70], Goss and Viallefond 1985 [50]). Their radio emission has been studied at various frequencies and radio-spectra have been constructed for more than 100 sources. The observed properties of radio emission from SNRs can be summarised as: a power-law spectrum $S_\nu \propto \nu^\alpha$ ($-0.8 \leq \alpha \leq 0$), a decrease in flux density with time[2], and linear polarisation (Lozinskaya 1992) [69]. These properties can satisfactorily be explained by the theory of synchrotron radiation (Kardashev 1962 [58], Shklovskii 1976a [96]).

Studying their radio emission it has been found that radio remnants can be classified into two categories - classical shells and plerions or filled remnants, while some objects, exhibiting properties of both, fall into class of composite remnants. SNRs are classed as shells if (Lozinskaya 1992) [69]:

[2]The decrease in flux density has been measured in eg. Tycho, Cas A, Crab. In contrast, observations of 3C 58 show that its flux density increases. This irregular jump in radio luminosity is believed to be associated with the passage of the reverse shock (Lozinskaya 1992) [69].

- the radio brightness increases from the centre toward the periphery, forming a complete or an incomplete shell;
- the spectral index α is less than -0.2, the mean is -0.5;
- a weak linear polarisation is observed, $p = 3 - 15\%$
- the magnetic field has quasi-regular structure.

The plerions are objects with the following characteristics:

- the brightness increases toward the centre;
- the spectral index α is in the range -0.3 to 0, with a mean of about -0.26 to -0.13;
- the magnetic field is regular, in most cases tangentially oriented;
- the linear polarisation is $20 - 30\%$ at high frequencies.

The fraction of plerions (produced in the SN type II explosions) is only $5 - 10\%$ of all detected SNRs in the Galaxy, despite the fact that their birth rate is approximately equal to that of shells. Hence, it has been proposed that plerions turn into classical shell objects as the radio emission from the central region fades (Lozinskaya 1980 [68]). Following this hypothesis, such objects, in a transitional stage between a shell and a plerion, have been identified (Helfand and Becker 1987 [53], Becker and Helfand 1984 [6], Becker et al. 1983 [5]).

Our present understanding of how radio synchrotron emission is generated by plerions and shells can be outlined in the following way (Lozinskaya 1992) [69]: the main energy source for the synchrotron emission from plerions is a pulsar, which produces magnetic field and injects particles. In the first stage (about 100 years or less after the explosion) the plerion may not be visible at radio-frequencies due to free-free absorption or intrinsically weak emission (Brown and Marscher 1978 [15]). In the next stage, the magnetic field and particles are produced at a constant rate and the plerion is observable. Approximately $10^3 - 10^4$ years after the explosion, injection falls off due to the pulsar spin-down but the emission is enhanced from swept-up field and particles. The remnant is in a transition between a plerion and a shell. In the last stage the remnant is observable as a shell; the injection from the pulsar is negligible and the radiation comes from the swept-up field and particles.

In the first evolutionary stage of shell remnants synchrotron radiation is produced by field and particles accelerated by the shock wave in the wind of the pre-SN. The most predominant acceleration mechanism is believed to be Fermi type I, which gives the observed energy spectrum. In the next stage the field is enhanced and the particles are accelerated in the connective layer at the boundary of the ejecta. Compressed interstellar field and particles accelerated behind the shock front in dense clouds are responsible for the radiation after $10^3 - 10^4$ years, while the last evolutionary phase is characterised by the radiation from field and particles in the swept-up shell during the radiative stage.

1.2.3 The historical supernova remnants

Details of the remnants of the five Galactic SN that have been seen and recorded in the old manuscripts and historical chronicles in the last millennium, together with Cas A[3], are given in Table 1.1 (Green 1984) [43].

Tycho, Kepler and SN 1006 have been classified as type I SN explosions. The SN I are characterised by a low-mass shell that is thrown off by the explosion. No neutron star is formed, which is suggested by the lack of a compact x-ray source and the fact that the radio and thermal x-ray emission originate from the shell (Lozinskaya 1992) [69].

Young historical SN II remnants (The Crab Nebula, 3C 58) are powered by a central pulsar, which produces the magnetic field and relativistic particles responsible for the synchrotron radiation, while in contrast to the young SN I remnants, radiation from the gas behind the shock front induced by expansion of the shell is negligible (Lozinskaya 1992) [69].

Source	Date	S_{408} (Jy)	Size ($'$)	Distance (kpc)	S_{408} (Jy) (if at 20 kpc)	Size ($'$) (if at 20kpc)
	1006	33	34	1	0.08	1.5
Crab	1054	1300	5	2	12	0.5
3C58	1181	68	6	2.6	0.7	0.8
Tycho	1572	92	8	2.3	1	0.5
Kepler	1604	33	3.2	4.4	1.6	0.7
Cas A	1680	6700	5	2.8	150	0.8

Table 1.1 The remnants of historical supernovae (adopted from Green 1984) [43].

Tycho's Supernova Remnant (A.D. 1572)

Tycho's SN from 1572 has been classified as a type I explosion, based on its light curve and colour reconstructed from eyewitness observations (Clark and Stephenson 1977) [26].

The first optical image of Tycho's SNR was obtained using the Hale telescope at Mount Palomar, showing a shell with a diameter of about 8 arcmin, with long, thin, bright filaments. The Balmer Hα and Hβ lines were detected in the optical spectrum (Kirshner and Chevalier 1987 [60], Chevalier et al. 1980 [22]). The Balmer lines of hydrogen dominate the spectra of all young remnants of SNI (Tycho, Kepler, and Remnant of SN 1006) despite the fact that their spectra are characterised by the absence of hydrogen lines. The hydrogen lines in the spectra of young remnants are the result of the collisional excitation at the shock front. They are not emitted

[3]The explosion of Cas A had probably been observed by Flamsteed in 1680, but this has never been reliably confirmed.

by the matter ejected by the explosion, which cannot be seen at optical wavelengths (Chevalier et al. 1980 [22]).

The remnant was observed with high-resolution radio-telescopes revealing a homogeneous shell surrounded by a thin rim (Henbest 1980 [56], Klein et al. 1979 [61], Dickel and Jones 1985 [30]). The radio spectrum has been found to be non-thermal, with the spectral index $\alpha = -0.61 \pm 0.03$.

The expansion rate of Tycho ($\mu = 0.256 \pm 0.026$) arcsec per year has been measured by comparing the position of the bright filaments in 1971 and 1979 (Strom et al. 1982) [103]. This result is in a good agreement with the average expansion rate ($|\mu| = R/t = 0.55$ arcsec per year), if the remnant has already been decelerated and entered the adiabatic expansion stage[4]. Another explanation would be that the measured expansion rate μ represents the velocity of the reverse shock rather than the blast wave.

The remnant has also been observed in x-rays (Fabbiano et al. 1980 [35], Becker et al. 1983 [5], Smith et al. 1988 [98]). The x-ray observations place an upper limit on the surface temperature ($T < (1.1 - 1.8) \times 10^6$ K) of any neutron star remaining after the explosion.

Kepler's Supernova Remnant (A.D. 1604)

Kepler's SNR, which exploded in 1604, has also been classified as type I SN, and is one of the best studied of any of the historical SNRs in our Galaxy.

Optical images of Kepler's SNR show bright filaments located in the northern part of the shell (Blair et al. 1991 [9]). Spectra of the filaments contain bright lines of Hα , [NII], [OII], [OIII], and [SII].

Radio observations of Kepler (Strom and Sutton 1975 [104], White and Long 1983 [124], Dickel et al. 1988 [31]) have shown that the radiation is non-thermal with $\alpha = -0.58$, polarised, and that the shell is expanding asymmetrically, which is the result of ambient gas being inhomogeneous.

The x-ray emission from this object was detected in 1979 (Tuohy et al. 1979) [111], revealing a thin shell coinciding with the radio image. The x-ray spectrum has a high and a low-temperature component, typical of young SNR. The high-temperature plasma is, probably, swept-up interstellar gas heated by the blast wave, while the low-temperature component is matter thrown off in the explosion and heated by the reverse shock (White and Long 1983) [124]. Gamma-ray emission was also discovered from this remnant (Kinugasa et al. 1999).

The remnant of SN 1006

The SN explosion that occurred in the year 1006 was the brightest supernova outburst, and was recorded in many Asiatic, Arabic, and European chronicles. According to its light curve this SN has also been classified as type I.

[4]In the adiabatic expansion stage $\mu/|\mu| = 0.4$ (Lozinskaya 1992) [69].

Radio observations of SN 1006 show a shell with a fine filamentary structure and a spectral index $\alpha = -0.6$ (Stephenson et al. 1977 [102], Green 1988 [45]). High resolution radio observations show a "barrel-like" axially symmetric morphology, which is probably the result of an asymmetric SN explosion (Roger et al. 1988) [83].

X-ray observations of the remnant show a prominent x-ray source with a similar structure to the radio source: a symmetric shell with a diameter of about 30 arcmin (Galas et al. 1982 [38], Vartanian et al. 1985 [115]).

An optical source has been identified with SN 1006 by van den Bergh in 1976 [112], showing a nebula with a very thin and long filament localised at the periphery of the shell where the x-ray and radio emission are weak, in contrast to other remnants.

Proper motion measurement obtained from the comparison of 1980 and 1979 plates yield $\mu = 0.30 \pm 0.04$ arcsec per year, while the mean expansion rate $|\mu| = 0.83$ arcsec per year (Long et al. 1988) [67].

The x-ray spectrum of SN 1006 suggests that the radiation is thermal with $T_e = 5 \times 10^7$ K at the edge, and $T_e = 1.8 \times 10^6$ K within the shell, assuming a plasma in ionisation equilibrium with density of $0.3 - 0.6$ cm^{-3} (Pye et al. 1981 [79], Galas et al. 1982 [38], Vartanian et al. 1985 [115]). Non-thermal x-ray (Koyama et al. 1995) [63] and gamma-ray emission (Tanimory et al. 1998) [109] were also detected from this remnant.

As in the case of Tycho and Kepler, the stellar remnant of SN 1006 has never been found. An upper limit on the surface temperature of a possible neutron star has been determined as $T < 8 \times 10^5$ K (Pye et al. 1981) [79].

The Crab Nebula (SN 1054)

The Crab Nebula was discovered by John Bevis, rediscovered by Messier and catalogued as the first entry in his famous catalogue. Almost 200 years later the connection between the nebula and the SN 1054 was recognised by Hubble.

The Crab Nebula is a composite remnant: a plerion powered by a pulsar, surrounded by a shell in the process of formation. The pulsar is the source of its relativistic particles and magnetic field, which generate the synchrotron radiation observed over the entire range of wavelengths from radio to x and gamma rays.

The optical emission from this remnant consists of the bright filaments, the diffuse synchrotron emission from the amorphous nebula and a faint jet.

The x-ray emission from the Crab Nebula is concentrated in a smaller region then the radio emission, forming a torus around the pulsar. It is strongly polarised, which confirms its synchrotron origin (Weisskopf et al. 1978) [121]. Recent high resolution x-ray observations with the Chandra X-Ray Observatory (Weisskopf et al, 2000) show a rich x-ray structure of this remnant: an x-ray inner ring within the torus, and x-ray knots along the inner ring. These observations also show that there are systematic variations of the x-ray spectrum throughout the nebula.

Radio maps are consistent with the details observed at optical wavelengths. These maps show enhanced radio emission associated with the optical filaments (Velusamy 1985) [117] and the jet (Velusamy 1984) [116]. The observed value of

the secular decrease in the flux density (-0.16%) agrees with the rate predicted by theoretical models (Aller and Reynolds 1985) [2].

1.3 Searching for young SNRs

1.3.1 Previous searches

High resolution radio observations have been used to study small compact radio sources, in search for young Galactic SNRs, underrepresented in current SNR catalogues. The results of several searches conducted in the last two decades are presented:

- **Helfand et al. 1984 [54]:** A sample of 19 sources was selected from the Caswell, Haynes and Clark (1975) [18] catalogue of small-diameter Galactic radio sources ($< 1.5'$). The sources were observed with the VLA at 5 GHz, in a search for plerions (Crab-like SNRs) in the Galaxy. Classification of the observed objects was based on their morphologies and polarisation characteristics. Only one object (previously identified as a SNR) had been found to have properties of the Crab-like remnants: centrally peaked brightness distribution and integrated polarisation greater than 5%. The remaining sources were classified as either compact HII regions or extragalactic sources. Based on these results a limit of 5 was set on the number of undiscovered Crab-like SNRs in the Galaxy above a 6 cm flux density of 1 Jy.
- **Green and Gull 1984 [49]:** A list of 32 small-diameter objects was selected from the Galactic plane radio surveys at 408 MHz and 5 GHz (Green 1974 [41], Caswell, Haynes and Clark 1975 [18]). Candidate young SNRs were selected on the criteria that their spectral indices are between - 0.8 and 0, which covers the expected range for both plerions and shell-type remnants. The selected sources were observed with the Cambridge 5-km telescope at 2.7 GHz and with the VLA at 4.9 GHz. Two objects in this survey were classified as possible young SNRs: G1.9+0.3 and G227.1+1.0. The first source has a shell-like morphology and its spectral index is about - 0.7, as expected for shell remnants. An upper distance limit of $\sim$30 kpc implies a diameter of less than 10 pc, which means that the age of this remnant would be between 400 and 1000 years. The non-thermal nature of the second source[5] was confirmed by its high degree of polarisation.
- **Green 1985 [44]:** High-resolution radio observations of 44 compact sources, using the VLA and the Cambridge 5-km telescope with a resolution of a few arcsec, identified two candidates (discussed by Green and Gull 1984 [49]). The remaining sources are found to be extragalactic or thermal sources (HII regions), based on their spectral indices and degree of polarisation. One of

[5]Green and Gull suggested this source was very young SNR still in free expansion, but this source is now believed to be extragalactic (Channan et al. 1986) [20].

these sources was later classed as a new small-diameter "filled centre" remnant (Reich et al. 1985) [80].

- **Green 1989 [46]:** Sources for this survey were selected because their infrared to radio flux density ratio was similar to those of known Galactic remnants. The infrared emission at 60 μm from the IRAS point source catalogue (Beichman et al. 1988) [7] was compared with the radio flux densities at 5 GHz where infrared/radio-source positional agreement was better than $1'$. The ratio of infrared to radio emission at $\sim$5 GHz is expected to be in the range 5 - 50 for SNRs, while HII regions are expected to have much stronger infrared emission. A sample of 11 small-diameter Galactic plane sources selected using this criterion was observed with the VLA at 4.86 GHz with a resolution of $4''$. None of the selected sources were found to have morphological characteristics of young shell remnants (the limb-brightened edges). Filled-centre remnants larger than $1.5'$ would not have been recognised in this survey (not expected to have bright features).
- **Sramek et al. 1992 [99]:** In this survey, 290 compact (radius $< 2'$) Galactic plane radio sources were observed at 20 cm and 6 cm using the VLA. The sources were selected from a 408 MHz survey (Clark and Crawford 1974) [25], a 5 GHz survey (Haynes et al. 1979) [52], and a 4.9 GHz survey (Altenhoff et al. 1979) [3]. The H110α radio-recombination line survey of Downes et al. 1980 [33] was first used to eliminate HII regions in the sample. The remaining sources were first observed at 20 cm to select sources with a shell-like morphology. Follow-up observations of 14 candidate shell sources were made at 6 cm to determine their spectral index and eliminate HII regions and the background extragalactic sources. In addition, radio-recombination line observations were made of three sources with shell structure and flat spectra (which established their thermal nature), and neutral hydrogen 21 cm observations of two sources with steep spectra (established their extragalactic nature). At the end, only one source was classed as a possible very young Galactic SNR, showing no RRL emission. However, this source was later (Subrahmanyan et al. 1993) [105] detected in H105α and H106α radio recombination line emission using the ATCA, which confirmed its thermal nature.
- **Gray 1994 [40]:** A total of 14 small-diameter sources, selected from the 408 MHz catalogue of Clark and Crawford (1974) [25], was observed with the ATCA at 5 GHz. Only one source was found to be a candidate small diameter SNR, based on its spectral index and polarisation of 15%. However, its structure and properties have not been determined well enough to distinguish it from extragalactic objects.

1.3.2 Challenges and problems of searching for young SNRs

The identification of SNRs is generally made from radio surveys of the Galactic plane and is limited by the sensitivity of the observation and by its resolution. In

such surveys only remnants with surface brightness above the sensitivity limit, and the angular size several times greater than the resolution, can be detected.

The criteria usually used to identify SNRs in radio surveys has been defined by (Clark and Caswell 1976 [24], Reich et al. 1985) [80]):

- identification with an historically recorded SN event (only for young SNRs);
- identification with an optical filamentary structure (optical remnant);
- non-thermal spectrum and linear polarisation, which indicate synchrotron process; radio recombination lines, which accompany free-free continuous radio emission are not expected to be present;
- shell or partial shell structure (for shell type remnants);
- proximity to the Galactic plane.

Young Galactic SNRs, the majority of which are expected to be radio emitters, appear as small-diameter, compact radio sources, and can be identified from images of the Galactic plane. Green (1984) [43] has discussed the sizes and flux densities expected for these young but distant Galactic SNRs. For example, remnants similar to Tycho or Kepler would have $S_{1\,\mathrm{GHz}} \sim 1$ Jy and a diameter of less than $1'$, if at a distance of 20 kpc (Table 1.1).

However, radio images of the Galactic plane contain other components of similar size, including Galactic HII regions, planetary nebulae, and background extragalactic radio sources. Hence, their identification entails distinguishing the young SNRs from other similar discrete components of the Galactic radio source population. This is particularly difficult for small-diameter remnants because high resolution observations are needed to determine their morphologies.

One approach to distinguish between SNRs and HII regions is to use radio spectra; HII regions have flat, thermal spectra, while spectra of SNR are steep, non-thermal. However, the physics of the interaction between the ejecta and the ISM from the small number of detected young SNRs is not well understood, and some young SNRs (eg. plerions) may have flat spectra and amorphous morphology similar to HII regions (Lozinskaya 1992) [69]. Hence, previous searches for young Galactic SNRs, based on spectral index and morphology, would miss these objects.

Previous searches also used the relative weakness of infrared emission from SNRs to distinguish them from thermal HII regions (Green 1989) [46], or the detection of radio recombination line (RRL), as an indicator of a thermal source, to eliminate HII regions from a sample of young SNR candidates (Sramek et al. 1992) [99].

Current catalogues of Galactic SNRs (Green 2000 [48], Whiteoak and Green 1996 [126]) contain less than 10 small-diameter SNRs, estimated to be younger than 1000 years, while about 20-40 young remnants await identification. As discussed by Green (1985) [44] it is difficult to estimate how many of these young remnants can be detected, either because some of them may be too faint to be detected in current radio surveys (eg. SN 1006 if at 20 kpc), or because very young remnants (< 100 years) are not radio sources. However, there are certainly several undiscovered young Galactic SNRs that can be identified from radio images of the Galactic plane.

1.4 Distinguishing SNRs and HII regions by FIR/radio ratio

It has been known from various studies that the ratio of far-infrared (FIR) to radio flux density is significantly different for thermal and non-thermal sources. Consequently, this ratio has been used to distinguish Galactic HII regions and SNRs.

In the Westerbork Synthesis Radio Telescope 327 MHz Survey of the Galactic Plane (Taylor et al. 1996) [110] it has been found that the value $R_{327\,\mathrm{MHz}} = S_{60\mu m}/S_{327\,\mathrm{MHz}} = 200$ can be used as a boundary between thermal and non-thermal radio emitters.

Fürst et al. (1987) [37] give values $R_{2.7\,\mathrm{GHz}} = 500 - 1500$ for HII regions, and $R_{2.7\,\mathrm{GHz}} \sim 10$ for SNRs, by comparing their 60 μm infrared and 2.7 GHz radio emission.

By comparing the 60μm infrared to 5 GHz radio flux density of 11 known small-diameter SNRs, Green (1989) [46] has found this ratio to be in the range of 5 to 50.

Whiteoak and Green (1996) [126] give typical values of the ratio $R_{843\,\mathrm{MHz}}$ of 60μm to 843 MHz emission for various objects including compact HII regions ($R_{843\,\mathrm{MHz}} =$ 1000), extended HII regions ($R_{843\,\mathrm{MHz}} = 500$), extragalactic objects ($R_{843\,\mathrm{MHz}} = 0$ - 200), planetary nebulae ($R_{843\,\mathrm{MHz}} = 50$ - 400), and SNRs ($R_{843\,\mathrm{MHz}} < 50$).

In an infrared survey of Galactic SNR which includes 157 objects, Arendt (1989) [4] has found that the infrared emission, revealed in about 30% of the known Galactic SNR, appears to be the result of thermal emission from dust grains which are swept by the SNR ejecta. Comparing the infrared and radio emission of Galactic SNRs (Arendt 1989) [4] has also found that young Galactic remnants (CasA, Tycho, Kepler, Crab) have $R_{1\,\mathrm{GHz}} = S_{60\mu m}/S_{1\,\mathrm{GHz}} < 1$, while $R_{1\,\mathrm{GHz}}$ for older remnants can be as large as several hundreds. For example, SNR G23.6+0.3 has $S_{1\,\mathrm{GHz}} = 8$ Jy and $S_{60\mu m} = 5300$ Jy, which gives $R_{1\mathrm{GHZ}} = 670$. This is much larger than expected by comparing it with the value of $R_{2.7\,\mathrm{GHz}}$ found by Fürst et al. (1987) [37], and it has been argued by Arendt (1989) [4] that Fürst et al. (1987) [37] used a much smaller sample of SNRs which was heavily biased toward young Galactic remnants.

These results are summarised in Table 1.2 which lists ratios of infrared to radio emission for HII regions and Galactic SNRs as found by observing these objects at various radio frequencies.

The distinction between young and old SNRs according to their ratio of infrared to radio emission can be explained by the decrease of radio emission in more evolved remnants (Chevalier 1982) [21], while their infrared luminosity will increase proportionally to the mass of the swept-up dust at a constant temperature (Arendt 1989) [4]. It has been estimated (Chevalier 1982 [21], Arendt 1989 [4]) that a remnant can arrive at an "old age" in terms of its IR-to-radio luminosity ratio after a time of < 2000 years.

Hence, the ratio of infrared to radio emission can be used to identify young SNRs, while more evolved remnants (older than about 2000 years) can be confused with

	HII regions	SNRs	Ref.
$R_{327\,\mathrm{MHz}}$	> 200	< 200	(Taylor et al. 1996) [110]
$R_{843\,\mathrm{MHz}}$	500 - 1000	< 50	(Whiteoak and Green 1996) [126]
$R_{1\,\mathrm{GHz}}$		< 1 young SNRs	(Arendt 1989) [4]
$R_{1\,\mathrm{GHz}}$		< 1000 old SNRs	(Arendt 1989) [4]
$R_{2.7\,\mathrm{GHz}}$	500-1500	$\sim$10	(Fürst et al. 1987) [37]
$R_{5\,\mathrm{GHz}}$		5-50 young SNRs	(Green 1989) [46]

Table 1.2 Ratio of infrared to radio emission for HII regions and SNRs

HII regions.

1.5 Distinguishing SNRs and HII regions by MIR/radio ratio

In addition to FIR/radio ratio thermal and non-thermal Galactic sources can also be distinguished by comparing their mid-infrared (MIR) and radio emission.

In a recent study (Cohen and Green 2001) [27] a detailed comparison of radio (843 MHz) and MIR (8.3 μm) images of a region of the Galactic Plane has been made to find global characteristics for different types of sources, and establish possible criteria for their identification.

The Molonglo Galactic Plane Survey (MGPS) at 843 MHz (Green et al. 1999) [42] and the Midcourse Space Experiment (MSX) at 8.3 μm (Egan et al. 1999) [34] were used for this comparison, which showed that thermal sources have significantly larger MIR/radio flux density ratios than non-thermal emitters. The value $R = S_{8.3\mu m}/S_{843\,\mathrm{MHz}}$ was determined for a limited number of previously independently identified sources (Whiteoak et al. 1994) [125], and the results can be summarised as (Cohen and Green 2001) [27]):

- $R = S_{8.3\mu m}/S_{843\,\mathrm{MHz}} = 27 \pm 3$ (standard error of the mean) for 33 identified HII regions (with R in the range $6.2 - 73.4$). The MSX counterparts are in the form of a polycyclic aromatic hydrocarbon (PAH) halo surrounding the Stromgren sphere, and thermal emission by dust grains.
- $R = S_{8.3\mu m}/S_{843\,\mathrm{MHz}} = 18 \pm 3$ for 21 planetary nebulae.
- Upper limits of $R = S_{8.3\mu m}/S_{843\,\mathrm{MHz}}$ for the non-thermal sources in the sample were found to be in the range $0.15 - < 6.2$.

The calculation of R was made using the spatially integrated flux density measurements at 8.3μm from preliminary MSX images with 46″ resolution, which matches the resolution of MGPS survey.

1.6 Distinguishing HII regions from SNRs by detecting RRL emission

HII regions are thermal radio sources and their free-free continuum emission is accompanied by radio recombination line (RRL) emission which is a result of electronic transitions between high energy levels in excited atoms. The RRL emission is observed as a narrow feature superimposed upon the continuum spectrum.

The detection of RRL can be used to distinguish thermal and non-thermal radio sources in the images of the galactic plane (HII regions and SNRs). In addition, observed line parameters such as velocity, intensity, and line width can be interpreted in terms of the properties of the detected HII regions such as density, temperature and elemental abundances.

The theory of continuum and RRL emission from HII regions is discussed in Aller (1956) [1], Osterbrock (1974) [77], Rohlfs (1986) [84], Brocklehurst and Seaton (1972) [11], Brown, Lockman and Knapp (1978) [14], Brown (1980) [12], Roelfsema and Goss (1992) [82] etc. Only a few general properties of HII regions and their continuum and line emission will be summarised in this section (with more detail in the Appendix).

1.6.1 HII regions

Galactic HII regions or gaseous nebulae are regions of ionised interstellar gas with temperatures of $3-5\times10^3$K. Some gaseous nebulae are observed as bright extended objects in the sky (Orion nebula NGC 1976, Ring nebula NGC 672), but many other, intrinsically less luminous or more distant nebulae are affected by interstellar extinction and faint in the optical part of the spectrum.

Based on the observational evidence a typical HII region consists of hydrogen, the various elements which are present according to their stellar abundances, and a certain amount of dust. Throughout the nebula, H is ionised, He is singly ionised, and other elements are mostly singly or doubly ionised. Typical densities in the ionised part of the nebula are of order $10-10^3$ cm^{-3}, decreasing outwards from the centre. In addition, large density variations can exist within some nebulae, which includes extremely compact features having electron densities of 10^4 cm^{-3}, and globules or filaments detected in optical and in high-resolution radio observations. Typical masses of observed HII regions are of order 10^2-10^4 $M_\odot$.

In the optical part of the spectrum, HII regions have relatively weak continuous spectra due to free-bound transitions. In addition, many nebulae have reflection continua consisting of starlight scattered by dust. The continuum emission extends to the infrared part of the spectrum and is largely thermal radiation emitted by dust. Emission line spectra of HII regions in the optical part of the spectrum are dominated by the forbidden lines of ions of common elements such as O, N, and He.

In the radio-frequency part of the spectrum, HII regions have strong continuum due to free-free emission (bremsstrahlung) of thermal electrons accelerated in the

Coulomb field of protons, and weak emission lines of H, resulting from bound-bound transitions between high atomic levels. Weaker radio recombination lines of He and other elements can also be observed.

1.6.2 Photoionisation structure of HII regions

The source of ionisation of HII regions is ultraviolet radiation from one or more O or B-type stars with temperatures of $3-5\times10^4$K, within or near the nebula. The ultraviolet photons from these stars transfer energy to HII regions by photoionisation. Photons with energy greater than 13.6 eV, the ionisation potential of hydrogen, are absorbed and the excess energy of each absorbed photon, over the ionisation potential, appears as kinetic energy of a liberated photoelectron. This energy is distributed by collisions between electrons and between electrons and ions. In such a way a Maxwellian velocity distribution is maintained with temperature in the range of $5000-10000$K. This temperature is fixed by the equilibrium between heating by photoionisation and cooling by radiation from the nebula.

In a typical HII region, the ultraviolet radiation field is so intense that the hydrogen in the nebula is almost completely ionised. The ionised part (*"Stromgren sphere"*) is separated by a thin transition region from an outer neutral gas cloud or HI region.

HII regions also consist of helium (about 10%) and other elements. These elements will be ionised too if there is enough high energy photons ($E > 24.6$ eV for He) from the ionising star.

A simplified version of the ionisation structure of an HII region is shown at Figure 3.1 (Roelfsema and Goss 1992 [82]) where the main components, including hydrogen R_H and helium R_{He} Stromgren radius can be seen.

1.6.3 Radio continuum emission from HII regions

At low frequencies radiation of an HII region can be described as a black body radiation (the total flux density is proportional to the square of the frequency and the HII region is opaque), while at high frequencies (above the so called 'turnover frequency') an HII region is semi-transparent and the flux density is approximately constant.

Mezger and Henderson (1967) [73] give an expression for the brightness temperature of an HII region for the optically thin case:

$$T_b = 8.235\cdot10^{-2}\left(\frac{T_e}{K}\right)^{-0.35}\left(\frac{\nu}{GHz}\right)^{-2.1}\left(\frac{EM}{pc\cdot cm^{-6}}\right)\cdot a(\nu,T) \tag{1.3}$$

where the dimensionless correction $a(\nu,T)$[6] is close to 1, for densities and temperatures of typical HII regions, and the *emission measure* EM is defined as

$$\frac{EM}{pc\cdot cm^{-6}} = -\int_0^s \left(\frac{N_e}{cm^{-3}}\right)^2 d\left(\frac{s}{pc}\right). \tag{1.4}$$

[6]Values of $a(\nu,T)$ have been tabulated by Mezger and Henderson (1967) [73].

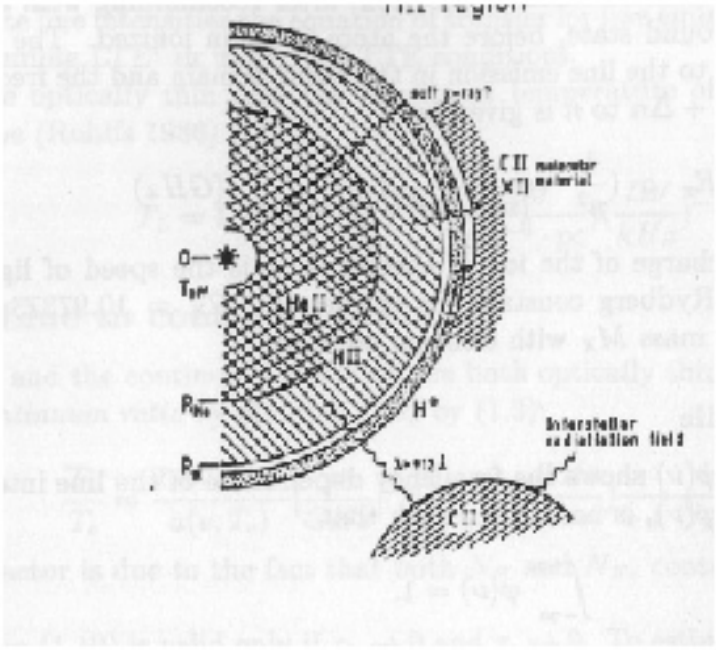

Figure 1.2 A schematic representation of a typical HII region and its surroundings (Roelfsema and Goss 1992) [82].

In the derivation of the formula for the brightness temperature the assumption is made that the plasma is macroscopically neutral and that the chemical composition is given approximately by $N_H : N_{He} : N_{other} = 10 : 1 : 10^{-3}$, which implies $N_i = N_e$. In addition, the electron temperature T_e is assumed to be constant along the line of sight.

1.6.4 RRL emission from HII regions

Radio recombination line (RRL) emission from HII regions is a result of electronic transitions between high energy levels in excited atoms of hydrogen and other elements. Lines corresponding to the transitions $n+1 \rightarrow n$ are strongest and called α lines; those for transitions $n+2 \rightarrow n$ are β lines; $n+3 \rightarrow n$ produce γ lines; etc. Following this notation, $H107\alpha$ is the line corresponding to the transition $108 \rightarrow 107$ of H. High α transitions with $n \geq 60$ produce lines in the radio wavelength range.

RRLs are weak compared with the continuum radio emission. RRLs from heavier elements, present as singly ionised ions, are much less intense than H lines because of their low abundances.

Frequency of the emitted line

Recombination lines are emitted when an electron, after recombining with an ion, cascades down to the ground state, before the atom is again ionized. The higher level transitions give rise to the line emission in the radio domain and the frequency ν for a transition from $n + \Delta n$ to n is given by

$$\nu = Z^2 \cdot R_x \cdot c \cdot (\frac{1}{n^2} - \frac{1}{(n + \Delta n)^2}) \qquad (GHz) \qquad (1.5)$$

where Z is the nuclear charge of the ion of species X, c is the speed of light (in kms^{-1}), and R_x is the Rydberg constant for species X: $R_X = 10.97373 \cdot (1 + m_e/M_X)^{-1}$, for a nuclear mass M_X with electron mass m_e.

Shape of the line profile

The line profile function $\varphi(\nu)$ shows the frequency dependence of the line intensity. The line profile function $\varphi(\nu)$, is normalised such that

$$\int_{-\infty}^{+\infty} \varphi(\nu) = 1. \qquad (1.6)$$

Because the natural line width is negligible compared to the Doppler broadening caused by thermal motions in the gas the basic line profile for a homogeneous ionised gas is Gaussian with the FWHM (full width at half intensity) given by (Rohlfs 1986) [84]:

$$\Delta\nu = \frac{2\nu}{c}(\frac{2kT_e}{M} log_e 2)^{1/2}. \qquad (1.7)$$

where k is the Boltzmann constant.

Comparing the line width calculated by (1.7) with the observed values it was suggested that a non-thermal motion (called "micro-turbulence") contribute to the broadening, and the linewidth can be generalised to (Rohlfs 1986) [84]:

$$\Delta\nu = \frac{2\nu}{c}[2(\frac{kT_e}{M} + {v_t}^2) log_e 2]^{1/2}. \qquad (1.8)$$

This is a non-thermal part of the Doppler broadening, which causes a broader Gaussian shape of the line profile.

In higher density gas electrons are more likely to collide with ions. As a result the energy levels become smeared and less discrete, leading to a broader line of the Lorentzian shape *(pressure broadening)*. If pressure broadening is significant the line profile becomes a Voigt function (convolution of the Gaussian and Lorentzian shape) (Rybicki and Lightman 1979 [86]). Pressure broadening depends strongly on the observing frequency (Roelfsema and Goss 1992 [82]).

In HII regions with an inhomogeneous density distribution the observed RRL will be Gaussian in shape and with a decreased peak line intensity due to pressure broadening. Voigt profiles will only be observed in relatively homogeneous clumps of ionised gas (Shaver 1979) [92].

Line intensity under conditions of LTE

To calculate line intensities the equation of transfer for line emission has to be solved, either assuming LTE[7] or under non-LTE conditions.

For the optically thin case the brightness temperature of the line emission is found to be (Rohlfs 1986) [84]:

$$T_L = 1.92 \cdot 10^3 (\frac{T_e}{K})^{-3/2} (\frac{EM}{cm^{-6} \cdot pc})(\frac{\Delta\nu}{kHz})^{-1}. \quad (1.9)$$

1.6.5 Line to continuum ratio

If the line and the continuous radiation are both optically thin it is possible to find *line to continuum ratio* by dividing (1.9) by (1.3):

$$\frac{T_L}{T_c} = \frac{2.330 \cdot 10^4}{a(\nu, T_e)} [\frac{\nu}{GHz}]^{2.1} [\frac{T_e}{K}]^{-1.15} (\frac{kHz}{\Delta\nu}) \frac{1}{1 + N_{He}/N_H}. \quad (1.10)$$

The last factor is due to the fact that both N_H and N_{He} contribute to the electron density.

Relation (1.10) is valid only if $\tau_L \to 0$ and $\tau_c \to 0$. To estimate the line emission for some finite optical depth we suppose that the line and the continuous radiation are emitted by the same HII region with an electron temperature T_e. In that case the temperature observed at the line centre is $T_{bL} = T_e(1 - e^{-(\tau_L + \tau_c)})$, and the temperature of the continuum is $T_{bc} = T_e(1 - e^{-\tau_c})$. The brightness temperature of the line alone is then:

$$T_L = T_{bL} - T_{bc} = T_e e^{-\tau_c}(1 - e^{-\tau_L}). \quad (1.11)$$

Hence, for $\tau_c \gg 1$ (optically thick case), no RRLs are visible (black-body). Hence, RRLs cannot be observed at low frequencies at which the continuous radiation becomes optically thick. But there are also limits for the highest frequency because $\Delta\nu$ increases with frequency and hence T_L/T_c decreases. For example, a frequency of ~5 GHz (H107α) is high enough so that the radiation is optically thin and the line to continuum ratio is high enough so that the RRL emission can be observed.

1.6.6 Line intensity under non-LTE conditions

The relative importance of non-LTE effects, pressure broadening and non-zero optical depth is shown at Figure 1.3 (Roelfsema and Goss 1992) [82] where line to continuum ratios were calculated for model HII regions. As Figure 1.3 shows the non-LTE effect is almost completely counteracted by pressure broadening so that RRL radiation appears to be emitted under near-LTE conditions. In addition, for the 5 orders of magnitude range in emission measures[8] observed in the majority

[7] Local thermodynamic equilibrium, for more details see the Appendix.

[8] Typically, $EM = 10^3 - 10^8$ $pc\ cm^{-6}$

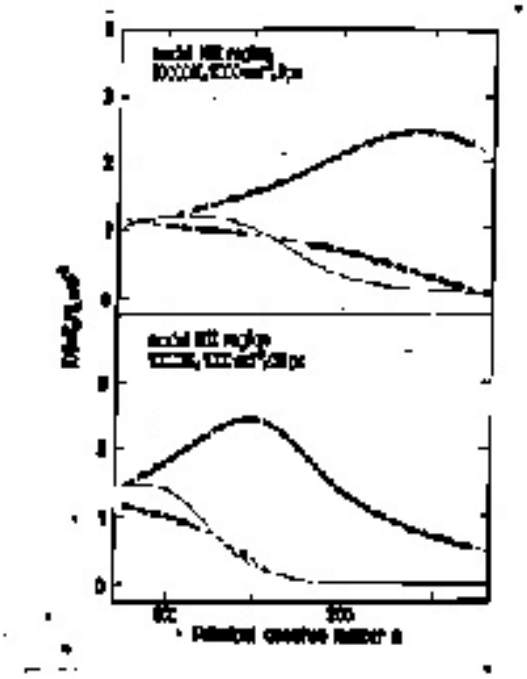

Figure 1.3 Theoretical line to continuum ratios for model HII regions. The quantity $100T_L/(T_c\nu)$ (in GHz) is shown as a function of principal quantum number for density, temperature, and optical depth as indicated. The full curve shows the solution assuming non-LTE effects and pressure broadening. The dashed curve shows the solution assuming LTE and no pressure broadening. The dash-dotted curve shows the solution assuming non-LTE effects but neglecting pressure broadening. (Roelfsema and Goss, 1992 [82]).

of Galactic HII regions RRLs at frequencies $\nu \geq 1$ GHz are, in fact, emitted under near-LTE conditions (Shaver 1980) [93] and no non-LTE correction needs to be applied to obtain physical parameters from the observed line radiation.

1.7 Scope of this thesis

1.7.1 Aim, method, and source selection

A sample of 9 small but spatially resolved Southern Galactic radio sources have been selected from the Molonglo Galactic Plane Survey (MGPS) (Green et al. 1999) [42]. These sources have been selected as possible young Galactic supernova remnants on the basis on their diameter ($< 4'$). To eliminate the possibility that some of them are HII regions, observations in H107α ($\sim$ 5 GHz) were attempted by Dr Anne Green and Professor Lawrence Cram, using the Australia Telescope Compact Array (ATCA). These observations will be analysed and the detection of radio recombination line emission will indicate that the observed source is thermal (HII region). This will eliminate HII regions from the sample. Lack of detectable RRL emission will indicate a non-thermal source (a young Galactic SNR candidate) if the expected strength of any possible line emission from that source is above the sensitivity limit. The theory of RRL emission from HII regions will be used to calculate the expected line strength of the selected sources.

The available infrared (IRAS and MSX) data will be used to determine the ratio of infrared to radio emission of the selected sources. Relative weakness of the infrared emission at 60μm and 8.3μm will also indicate a potential non-thermal source.

In addition, the parameters of the detected line emission will be used to estimate properties of the identified Galactic HII regions from the sample. Their velocities, distances and temperatures will be calculated.

The source selection has been based on apparent size. According to the adiabatic model of SNR evolution apparent size of a SNR less than 1000 year old at a distance of about 10-20 kpc, will be less than $4'$. This agrees with the observations of young Galactic (historical) remnants (Table 1.1). Spatially resolved radio continuum sources from the MGPS were selected so that the majority of unresolved background extragalactic objects are excluded from the sample. However, this will also exclude a small number of very young Galactic SNRs, which are unresolved in the MGPS images. Previously observed source SgrE19 (G358.6+0.1) (Cram et al. 1996) [28], with no detected RRL in H92α at 8 GHz, and hence suggested to be non-thermal, was also included in the sample to confirm this result. Source G267.9-1.1, a well known HII region (Caswell and Haynes 1987) [19], was included in the sample as a test source to ensure that the observational method could be verified. The Galactic and Equatorial J2000 coordinates of the selected sources are given in Table 1.3.

There are more than one hundred slightly resolved radio sources in the MGPS which are potential young Galactic SNRs. Figure 1.4 shows one of the MGPS mosaics with four such sources. A sample of approximately 10% (9 sources) have been selected to test and refine the observing technique, before observing a larger sample from the MGPS. The observations of these sources will be used to compare the expected strength of the line emission with the sensitivity of the ATCA observations.

Source	Galactic coordinates		Equatorial (J2000)	
G267.9-1.1	267.94743	-1.06542	08:59:05.00	-47:31:16.00
G282.8-1.2	282.83542	-1.24960	10:11:15.00	-57:43:50.00
G302.4-0.1	302.44671	-0.10533	12:47:10.00	-62:58:23.00
G304.5-0.1	304.47466	-0.05328	13:04:59.00	-62:53:04.00
G313.8+0.7	313.79102	0.71361	14:20:43.00	-60:15:44.00
G323.8+0.0	323.79902	0.01327	15:30:58.00	-56:15:14.00
G331.7-0.1	331.74725	-0.07245	16:13:08.00	-51:17:38.00
G337.4-0.4	337.43014	-0.40349	16:38:57.00	-47:26:55.00
G358.6+0.1*	358.63390	0.06262	17:42:05.00	-30:04:00.00

Table 1.3 The selected sources - Galactic and Equatorial (J2000) coordinates of the ATCA pointings. *Cram et al. [28] designation of this source (SgrE19) will also be used.

1.7.2 Thesis outline

- **Chapter 2** presents MOST observations (843 MHz) from the Molonglo Galactic Plane Survey, the infrared (IRAS and MSX) emission, and the ATCA continuum and spectral line data ($H107\alpha$ at $\sim$5 GHz). Observing methods and the data reduction techniques are presented and discussed.
- **Chapter 3** discusses the results and proposes a classification of each of the individual sources. It also discusses the selected ATCA configuration in terms of the sensitivity.
- **Chapter 4** summarises the thesis and presents suggestions for future work.
- **Appendix** gives a short overview of the theory of radio recombination line emission from HII regions.

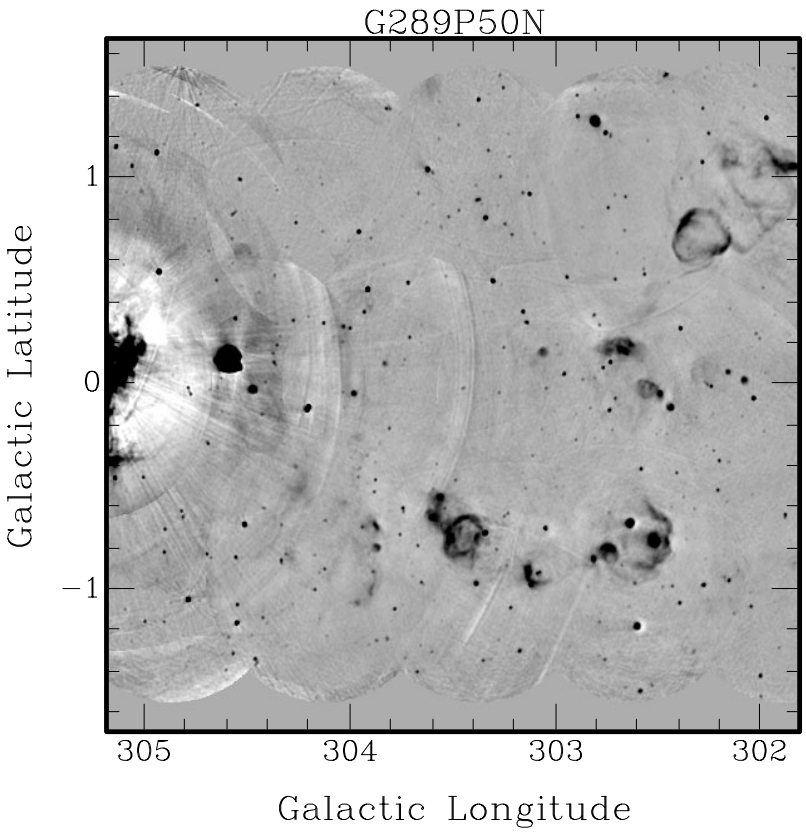

Figure 1.4 One of the MGPS mosaics (Green et al. 1999) [42] showing a section of the Galactic Plane, with compact small-diameter sources appearing as black disks. Four possible young SNR candidates are marked with arrows. Grayscale is clipped in range -17 to 41 mJy/beam.

Chapter 2

Observations

Young SNR candidates, including a test source G267.9-1.1, have been selected from the Molonglo Galactic Plane Survey (MGPS) (Green et al. 1999) [42]. A total of 9 small but spatially resolved sources, with a diameter smaller than $4'$, have been selected for this project. Spatially resolved sources have been chosen so that the majority of the unresolved extragalactic objects are excluded from the sample.

According to the adiabatic model of SNR evolution the mean expansion rate of a typical young SNR is 10^4 km s^{-1} or approximately 1 pc per century (Lozinskaya 1992) [69]. That means that the angular diameter of a 1000 year old remnant at a distance of 10-20 kpc would be less than $4'$[1]. Hence, size of a radio source has been used as an approximate selection criterion. This selection criterion should include all young Galactic SNRs, in the surveyed region, which have been developing in the past 1000 years, providing they are sufficiently bright to be detected[2]. Visual inspection of MGPS shows about 4-6 small but spatially resolved shells and disks ($4' \sim 5$ HPBW) per $3^o \times 3^o$ mosaic (Figure 1.4).

The selected sample, which includes a previously observed source SgrE19, believed to be non-thermal (Cram et al. 1996) [28], has been observed with the Australian Telescope Compact Array (ATCA) in the $H107\alpha$ transition at $\sim$5 GHz. The sample is distributed close to the Galactic Equator ($|b| < 1.5^o$) and covers the range RA 08:00 to 18:00 and Dec -30^o to -65^o. The Galactic and Equatorial J2000 coordinates of the selected telescope pointings are given at Table 1.3. The selected sources have also been identified with their infrared counterparts from the IRAS catalogues of infrared sources.

This chapter presents the MOST observations (843 MHz) from the Molonglo Galactic Plane Survey, the infrared (IRAS and MSX) emission, and the ATCA continuum and spectral line data ($H107\alpha$ at 5 GHz) and describes the techniques used to examine the selected sources.

[1] For example, Kepler's SN1604 is about 4 kpc away and $3'$ across. At a distance of 20 kpc this 400 year old remnant would have a size of $0.7'$ (Table 1.1)

[2] Only a small number of very young Galactic SNRs, which are unresolved in MGPS images, will not be in this sample.

2.1 843 MHz continuum data

The Molonglo Galactic Plane Survey (MGPS) (Green et al. 1999) [42] is a radio continuum survey made using the Molonglo Observatory Synthesis Telescope (MOST).

The MOST[3] operates at 843 MHz and has a resolution of $43'' \times 43'' cosec|\delta|$. As an east-west array, the telescope forms an elliptical synthesised beam that is elongated by a factor $cosec|\delta|$ in declination relative to right ascension.

The sensitivity (1σ) of the Molonglo Galactic Plane Survey is 1-2 mJy/beam and the positional accuracy is about $1''$ for point sources brighter than 20 mJy.

The survey covers a region of 330 deg^2, between $245^o < l < 355^o$ and ($|b| < 1.5^o$), with over 1.2×10^4 sources. It includes extended objects (diffuse emission from thermal complexes and ISM, discrete HII regions, planetary nebulae, and supernova remnants) and extragalactic objects, the majority of which are unresolved or barely resolved.

More than 450 overlapping fields (original $70' \times 70'$ images) have been assembled as a series of 37 ($3^o \times 3^o$) mosaics presented in Galactic coordinates. Figure 1.4 shows one of the mosaics with compact small-diameter sources which appear as black disks. The majority of MGPS sources are unresolved extragalactic objects.

The mosaics, as well as the original MGPS images are available in FITS format from the MGPS Web site[4].

The continuum pixel and contour maps of the selected sources are presented in Chapter 3. The selected regions have been displayed from the original $70' \times 70'$ MGPS images, downloaded from the MGPS Web site. The images have been regridded to J2000, using *miriad* synthesis imaging package (Sault and Killeen 1998) [88].

2.2 60 μm infrared data

The sources selected for this projects have been identified with their far-infrared counterparts to compare their infrared and radio emission and calculate the ratio $R = S_{60\mu m}/S_{843\,\mathrm{MHz}}$. The infrared counterparts have been found in the IRAS Catalogue of Point Sources (Beichman et al. 1988) [7], the IRAS Serendipitous Survey Catalogue (Kleinmann et al. 1986) [62], and the IRAS Small Scale Structure Catalogue (Helou and Walker 1988) [55].

The IRAS Catalogue of Point Sources (PSC) (Beichman et al. 1988) [7] is a catalogue of 250 000 well-confirmed infrared point sources (with angular extents less than approximately 0.5, 0.5, 1.0, and $2.0'$ at 12, 25, 60, and 100μm, respectively) observed by the Infrared Astronomical Satellite (IRAS). The survey is complete to about 0.4, 0.5, 0.6, and 1.0 Jy at 12, 25, 60, and 100 μm, respectively. Typical

[3]The MOST is operated by the University of Sydney with support from the Australian Research Council and the Science Foundation for Physics within the University of Sydney.

[4]The page is located at *http://www.astrop.physics.usyd.edu.au/MGPS*.

position uncertainties are about 2 to 16′. The catalogue contains positions, flux densities, uncertainties, and associations with known astronomical objects.

The IRAS Serendipitous Survey Catalogue (SSC) (Kleinmann et al. 1986) [62] is a catalogue of 43 866 point-like sources previously detected in the IRAS Pointed Observation Programme and observed with a longer integration time. Relative to PSC, the SSC is characterised by: increased sensitivity, reliability in uncrowded fields, uneven sky coverage and completeness, improved photometric accuracy, and reduced positional accuracy.

The IRAS Small Scale Structure Catalogue (SSSC) (Helou and Walker 1988) [55] is a catalogue of 16740 "small extended sources" containing sources resolved by the IRAS in any band but smaller than 8′. Positional accuracy is about 1′ and flux densities are accurate to about 50% (or better at high signal to noise ratios). Incompleteness is a complex function of wavelength band, brightness, and location, so that the absence of an entry in the catalogue does not necessarily imply the lack of detectable extended emission.

2.2.1 Identification with far-infrared counterparts

Comparison of MOST sources selected for this project with the IRAS Point Source Catalogue (PSC) (Beichman et al. 1988) [7] revealed 7 identifications. One source (G304.5-0.1) has been identified with an extended IRAS source catalogued in the IRAS Small Scale Structure Catalogue (Helou and Walker 1988) [55], while G282.8-1.2 most probably does not have any significant infrared emission. Source G267.9-1.1 has been identified with the IRAS source 08573-4718 catalogued in the IRAS Catalogue of Point Sources (PSC) (Beichman et al. 1988) [7] and The IRAS Serendipitous Survey Catalogue (SSC) (Kleinmann et al. 1986) [62]. However, the listed flux density is too low, since the extended infrared emission from this source is ignored in the PSC.

The positional agreements between the MOST and the associated IRAS sources are within 30″. The positional uncertainties in this comparison are dominated by the IRAS uncertainties. Figure 2.1 to 2.6 show some of the identified IRAS sources (Wheelock et al. 1991) [123] overlaid on the associated radio source contour map (843 MHz). The IRAS images in FITS format have been obtained from the Skyview web site (Wheelock et al. 1991) [123].

No PSC IRAS source, above the detection limit of 0.6 Jy/beam at 60 μm, has been detected close to the position of G282.8-1.2. The closest IRAS source 10090-7638, with an offset of r = 3.8′ is, most probably, not associated with G282.8-1.2 (Figure 2.2). Considering the size of the source and the fact that the infrared emission is not expected to extend much beyond the radio source, any significant infrared emission from this source would have been detected.

One possible explanation is that the infrared emission from this source is too extended so that its peak is below the sensitivity limit of the PSC (0.6 Jy/beam). However, the infrared emission is not expected to extend much beyond the radio source. Since the size of the radio source at 843 MHz is only 1.6′ x 1.2′, any significant

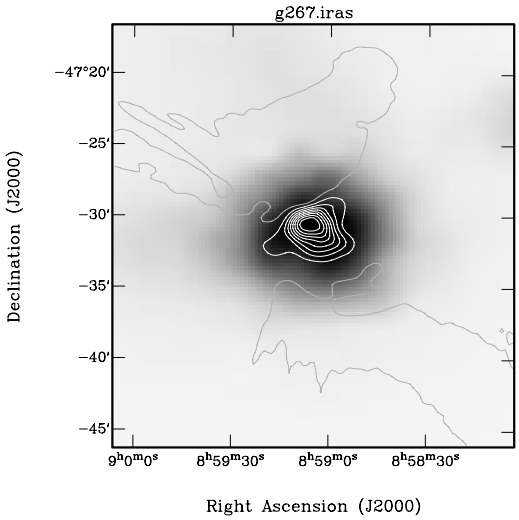

Figure 2.1 The G267.9-1.1 radio contours (843MHz) overlaid on the IRAS 60μm grayscale image of 08573-4718 (Wheelock et al. 1991) [123]. Resolution of the IRAS image is 2′. Grayscale is clipped in range = 22 to 15000 MJy/sr; contour image: contours x 87 mJy/beam; contours = 10, 20, 30, 40, 50, 60, 70, 80.

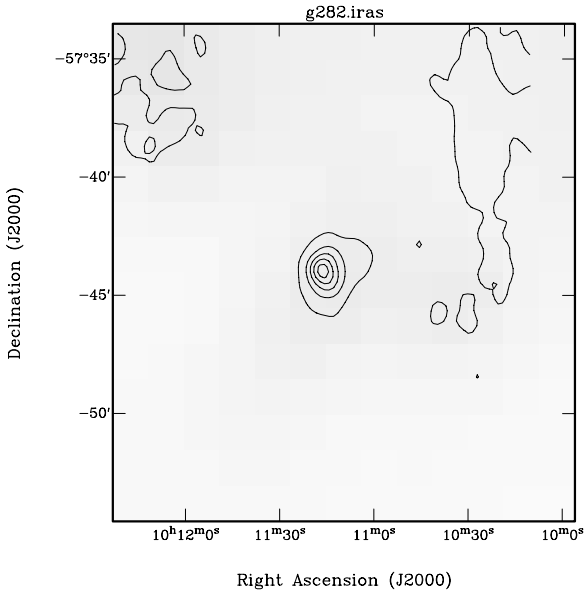

Figure 2.2 The IRAS 60 μm grayscale image, with a resolution of 2′, (Wheelock et al. 1991) [123] shows the region surrounding the radio source G282.8-1.2 (843 MHz, contours). Grayscale is clipped in range = 5 to 3000 MJy/sr; contour image: contours x 9 mJy/beam, contours = 2, 10, 14, 18, 22. There is no significant infrared emission at the position of G282.8-1.2 (above the sensitivity limit of 600 mJy/beam).

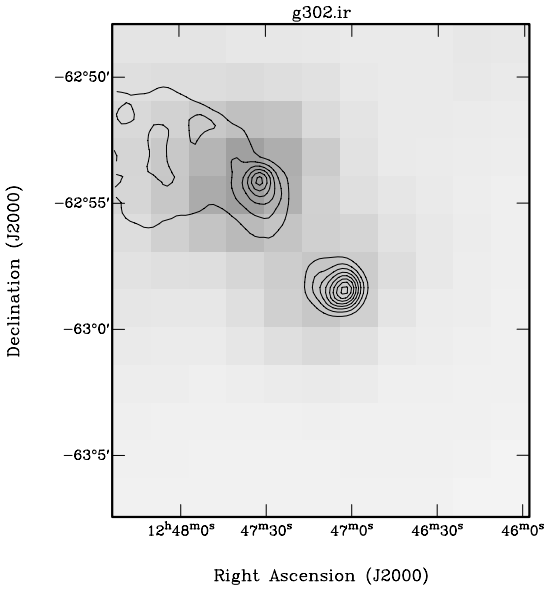

Figure 2.3 The G302.4-0.1 radio contours at 843 MHz overlaid on the 60 μm image of the IRAS source 12440-6242 (Wheelock et al. 1991) [123]. Resolution of the IRAS image is 2′. Grayscale is clipped in range 9 to 1400 MJy/sr (lin). Contour image: contours x 3 mJy/beam; contours = 2, 6, 8, 14, 26, 36, 42.

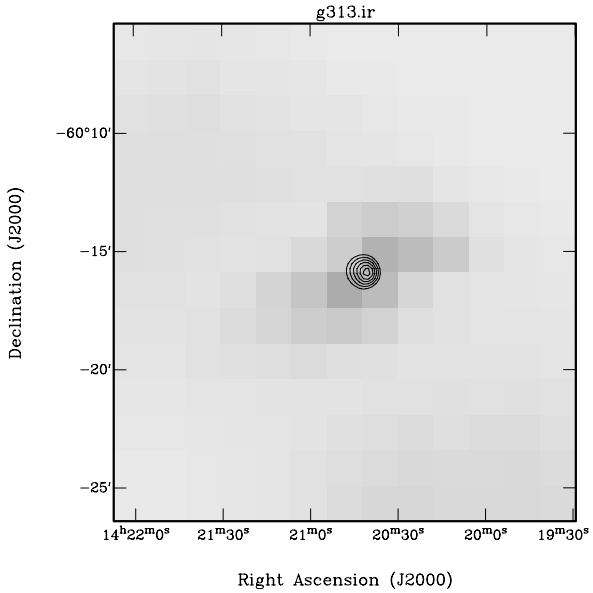

Figure 2.4 The G313.8+0.7 radio contours at 843 MHz overlaid on the 60 μm image of the IRAS source 14170-6002 (Wheelock et al. 1991) [123]. Resolution of the IRAS image is 2′. Grayscale clipped in range 11 to 1700 MJy/sr. Contour image: contours x 13 mJy/beam; contours = 2, 4, 8, 12, 16, 18.

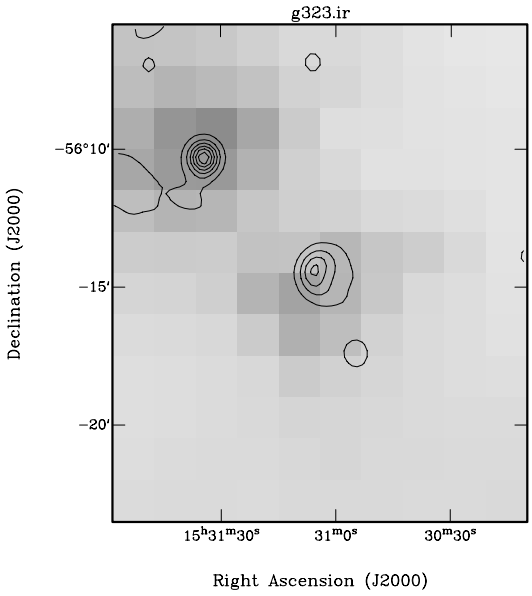

Figure 2.5 The G323.8+0.0 radio contours overlaid on the 60 μm image of the IRAS source 15272-5604 (Wheelock et al. 1991) [123]. Resolution of the IRAS image is 2′. Grayscale clipped in range 10 to 1200 MJy/sr. Contour image: contours x 10 mJy/beam, contours: 2, 8, 14, 18.

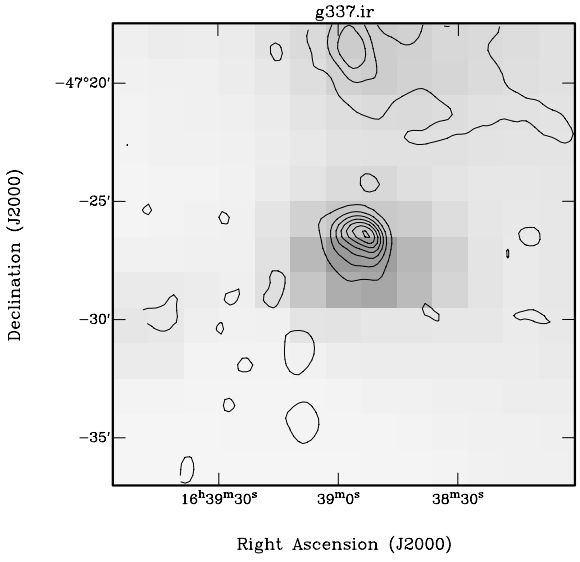

Figure 2.6 The G337.4-0.4 radio contours at 843 MHz overlaid on the 60 μm image of the IRAS source 16352-4721 (Wheelock et al. 1991) [123]. Resolution of the IRAS image is 2′. Grayscale clipped in range 19 to 7300 MJy/sr. Contour image: contours x 34 mJy/beam, contours = 1, 3, 5, 7, 9, 11, 13.

infrared emission from G282.8-1.2 would have been detected.

Source G304.5-0.1 has been identified with the infrared source X1301-625 catalogued in the IRAS Small Scale Structure Catalogue (SSSC) (Helou and Walker 1988) [55]. The infrared counterpart X1301-625 has the average non-colour corrected, spatially integrated flux density of 1620 Jy at 100 μm. However, the 60 μm flux density of this source is not listed in the catalogue.

2.3 8.3 μm infrared data

The sources selected for this projects have been identified with their mid-infrared counterparts, to compare their infrared and radio emission and calculate the ratio $R = S_{8.3\mu m}/S_{843\,\mathrm{MHz}}$. The infrared counterparts have been found in the Midcourse Space Experiment Point Source Catalogue (Egan et al. 1999) [34].

The Midcourse Space Experiment (MSX) Point Source Catalogue (Egan et al. 1999) [34] is a catalogue of mid-infrared point sources ($4.2 - 25$ μm), which includes the areas missed by the IRAS mission, and the Galactic Plane where the sensitivity of IRAS was degraded by extended emission. The MSX survey is complete to about 0.1 Jy at 8.3 μm and has the resolution of 18.3″ in the final images.

All of the sources selected for this projects have been identified with their mid-infrared counterparts. Figure 2.7 to 2.12 show some of the identified MSX sources (Egan et al. 1999) [34] overlaid on the associated radio source contour map (843 MHz). The MSX images in FITS format have been obtained from the IPAC web site (http://irsa.ipac.caltech.edu/applications/MSX/).

2.4 The ATCA radio continuum and spectral line data

This experiment aims to eliminate thermal sources from the sample of SNR candidates by detecting their RRL. This is possible if the RRL emission is above the sensitivity limit of the ATCA observations. Hence, the expected line strength has been calculated using the theory of HII regions, and compared with the sensitivity of the survey.

The selected sources have been observed, in the H107α transition at 5 GHz. This radio recombination line emission corresponds to the transition $108 \rightarrow 107$ of hydrogen. Using (1.5) the rest frequency of the emitted H107α line has been calculated to be $\nu_0 = 5.2937332$ GHz. The observations were performed with a 512 channel receiver and a total bandwidth of 16 MHz, using the 0.750A ATCA configuration (with antenna 6). The parameters of the observations are given in Table 2.1.

Short observations ("*snapshots*") have been made with 5−6 pointings per source and about 25 minutes observing time for each pointing, evenly spread over 12 hours. The theoretical rms noise, which depends on the weighting scheme applied when

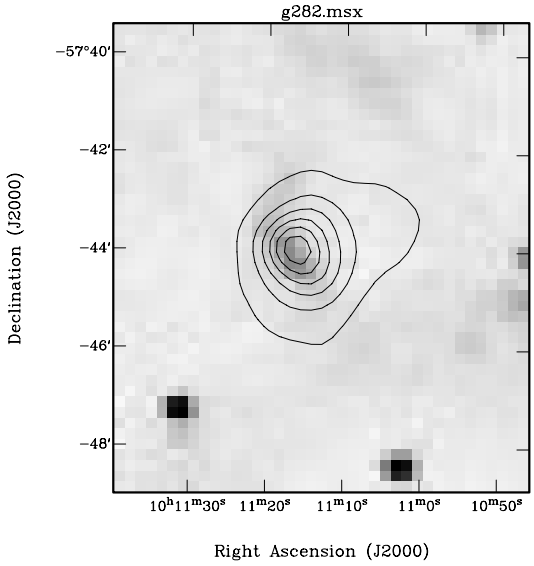

Figure 2.7 The G282.8-1.2 radio contours at 843 MHz overlaid on the 8.3 μm image of the MSX source. Resolution of the MSX image is 18.3″. Grayscale is clipped in range 4.22 x 10^{-7} to 1.54 x 10^{-5} W m^{-2} sr^{-1} (lin). Contour image: contours x 9 mJy/beam; contours = 2, 10, 14, 18, 22.

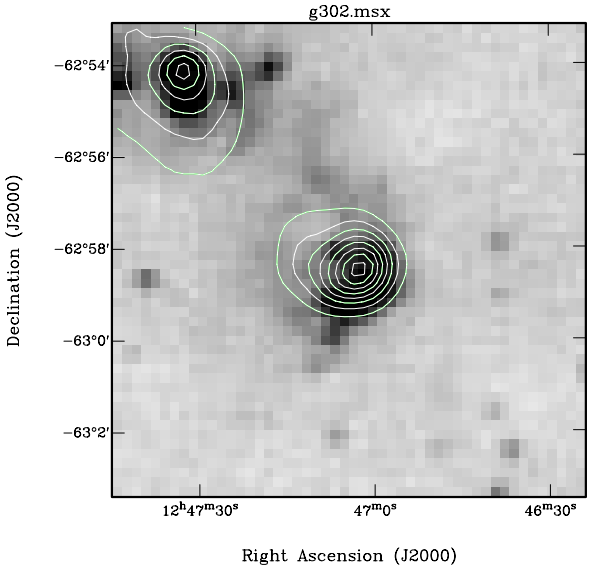

Figure 2.8 The G302.4-0.1 radio contours at 843 MHz overlaid on the 8.3μm image of the MSX source. Resolution of the MSX image is 18.3″. Grayscale is clipped in range 6.59 x 10^{-7} to 8.25 x 10^{-6} W m^{-2} sr^{-1} (lin). Contour image: contours x 3 mJy/beam; contours = 2, 6, 8, 14, 26, 36, 42.

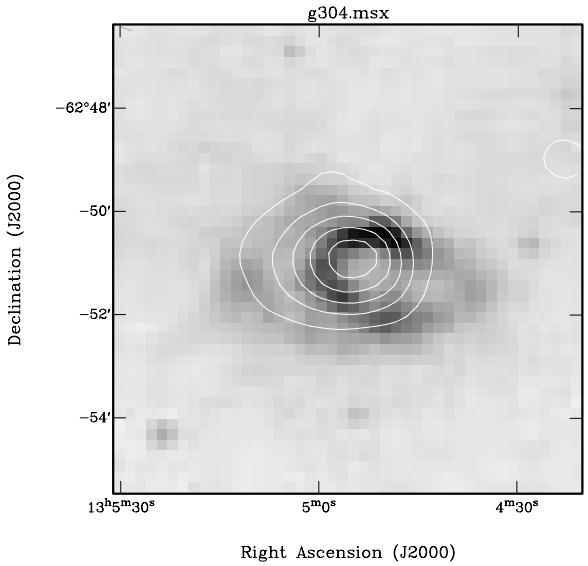

Figure 2.9 The G304.5-0.1 radio contours at 843 MHz overlaid on the 8.3μm image of the MSX source. Resolution of the MSX image is 18.3″. Grayscale is clipped in range 7.98 x 10^{-7} to 1.48 x 10^{-6} W m^{-2} sr^{-1} (lin). Contour image: contours x 6 mJy/beam; contours = 4, 6, 10, 14, 20.

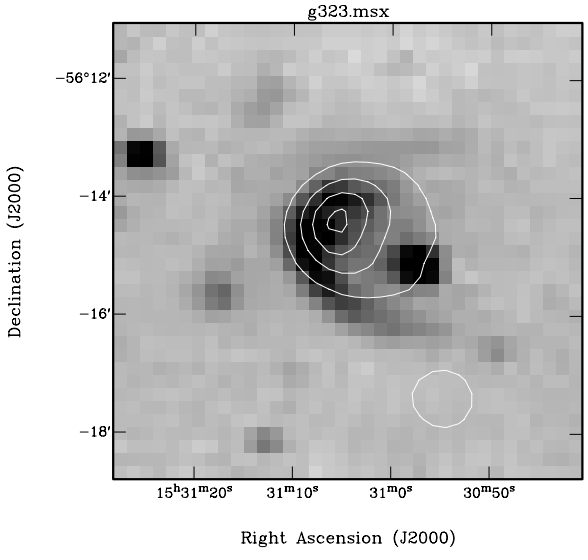

Figure 2.10 The G323.8+0.0 radio contours overlaid on the 8.3 μm image of the MSX source. Resolution of the MSX image is 18.3″. Grayscale clipped in range 7.32 x 10^{-7} to 9.60 x 10^{-6} W m^{-2} sr^{-1}. Contour image: contours x 10 mJy/beam, contours: 2, 8, 14, 18.

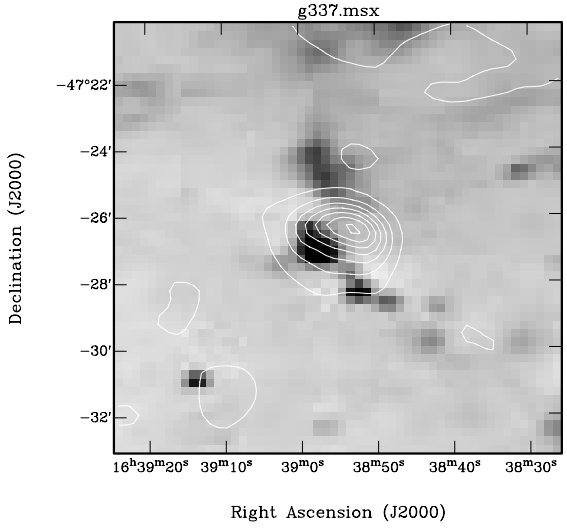

Figure 2.11 The G337.4-0.4 radio contours at 843 MHz overlaid on the 8.3 μm image of the MSX source. Resolution of the MSX image is 18.3″. Grayscale clipped in range 1.40 x 10^{-6} to 2.04 x 10^{-5} W m^{-2} sr^{-1}. Contour image: contours x 34 mJy/beam, contours = 1, 3, 5, 7, 9, 11, 13.

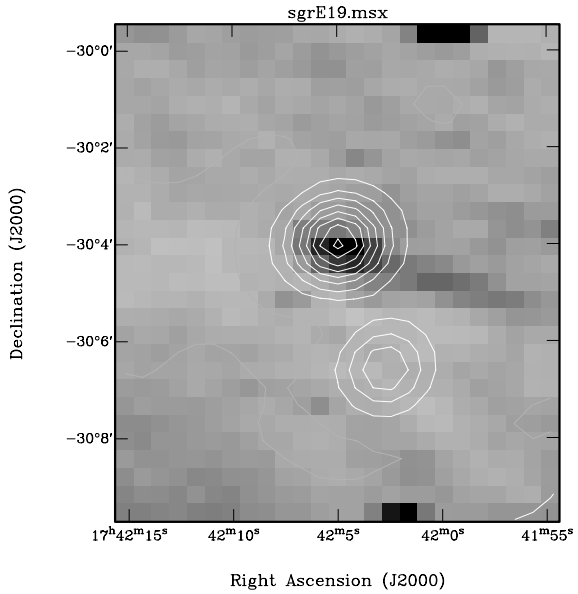

Figure 2.12 The SgrE19 radio contours at 843 MHz overlaid on the 8.3 μm image of the MSX source. Resolution of the MSX image is 18.3″. Grayscale clipped in range 1.82 x 10^{-6} to 2.05 x 10^{-5} W m^{-2} sr^{-1}. Contour image: contours x 43 mJy/beam, contours = 1, 2, 3, 4, 5, 6, 7, 8.

producing an image, has been calculated for each source field using *miriad* synthesis imaging package. Approximately, theoretical rms noise in a single channel image is 3 mJy/beam for an integration time of 140 minutes per source, and a channel bandwidth of 31.3 kHz.

This section describes the observing and imaging techniques used to obtain the continuum images and line spectra of the selected sources at 5 GHz.

2.4.1 Line to continuum ratio

At 5 GHz Galactic HII regions will be optically thin and under this condition line to continuum ratio can be calculated using (1.10).

The observed linewidths of Galactic HII regions at 5 GHz are in the range of 14-56 km s^{-1} (Caswell and Haynes 1987) [19]. In this experiment a single channel width is 1.77 km s^{-1} or 31.3 kHz (Table 2.1), which gives 247-990 kHz for an expected linewidth in this range. Putting these values into the formula, the line to continuum ratio was calculated to be between 2% and 7%, assuming a typical HII region with the electron temperature $T_e = 10^4$ K and relative helium abundance $N_{He}/N_H = 0.1$. This agrees with the line to continuum ratio calculated for a typical HII region by Roelfsema and Goss (1992) [82] (shown at Figure 1.3). For comparison, the values of T_L/T_C, for about 300 Galactic HII regions observed at 5 GHz, were found to be in the range from 2.2% to 20%, with a median value of 6.5% (Caswell and Haynes 1987) [19].

In high density HII regions ($n = 10^4$ cm^{-3}) linewidths could be affected by pressure broadening. However, the extended objects selected for this project are not likely to be ultra-compact, high density HII regions. In addition the pressure broadening depends strongly on the observing frequency and it is not significant at high frequencies (> 1 GHz) (Roelfsema and Goss 1992) [82].

It can be concluded that the H107α line peak emission of any observed HII region in this sample is expected to be about 5–6% and certainly not less than 2% of the continuum emission, spatially integrated over the source region.

2.4.2 Sensitivity

For an extended source larger than the synthesised beam area and having a constant surface brightness of I_m (mJy/arcsec^2), the flux density per synthesised beam is $I_m\Omega$ where Ω is the synthesised beam area (in arcsec^2). Hence, the signal to noise ratio for such a source is defined as (Crane and Napier 1994) [29]:

$$\frac{S}{N} = \frac{I_m\Omega}{\Delta I_m}, \tag{2.1}$$

where ΔI_m is the rms noise (1σ) in the image, (in mJy/beam).

Therefore, to increase the signal to noise ratio of an extended source, the synthesised beam has to be made larger, under the condition that the rms noise in the image does not increase significantly. In general, the beam size increases by

decreasing the resolution, scaling the array so that its beam matches the size of the source[5]. To some extent, the beam size can also be modified by applying an imaging technique called *tapering*.

Tapering is an imaging technique in which the visibility data are weighted by a Gaussian (or similar function) of specified FWHM, to weight down the data at the outer edge of the (u, v) coverage, suppressing small-scale sidelobes and increasing the beamwidth (Sramek and Schwab 1994) [100]. By applying a tapering function the rms noise usually increases but can remain constant, or even slightly decrease, for a particular range of the dispersion of the applied Gaussian taper function (Crane and Napier 1994) [29].

The signal to noise ratio of an extended source can also be improved by decreasing the rms noise ΔI_m in the image. The rms noise in an image made with an N-antenna array can be calculated as (Bridle 1994) [10]:

$$\Delta I_m = F_w \Delta S / \sqrt{\frac{nN(N-1)t\Delta\nu}{2}}, \tag{2.2}$$

where t is the total integration time, $\Delta\nu$ is bandwidth, $n = 2$ for images of Stokes I, ΔS is the single-interferometer sensitivity per unit time and per unit frequency, $F_w = 1$ for natural weighting, and $F_w > 1$ for other weightings.

Using the formula, the theoretical rms noise (1 σ) in the source-free part of a continuum image ($\Delta\nu = 13$ MHz[6]) is 0.1 mJy/beam (corresponding to the brightness temperature of 0.8 K), while in a single spectral line channel image ($\Delta\nu = 31.3$ kHz) it is about 3.2 mJy/beam (16.3 K), calculated for the integration time of about 140 minutes and the ATCA system sensitivity of about 357 Jy at 5.293 GHz[7].

According to (2.2) the rms noise in an image can be reduced by increasing the observing time and by increasing the channel width. However, the channel width is also determined by the required velocity resolution. Since RRL can be as narrow as 14-15 kms^{-1} (Caswell and Haynes 1987) [19], to achieve the required resolution the channel width has to be less than ~ 10 km s^{-1}.

The theoretical rms noise was calculated, and compared with the actual measured rms noise using *miriad*. The S/N measured in the single channel images was used to determine the upper limits of any undetected RRL. For example, to detect a minimum expected RRL emission (2% of the continuum) the S/N in each single channel image of a cube has to be 150, before continuum subtraction. The faintest source in the sample (G282.8-1.2) has S/N = 15, which means that the upper limit of the RRL emission is 20% of the continuum emission, or the (3σ) integrated channel sensitivity is $\Delta S = 20\%$ of the integrated continuum flux density.

The sensitivity can be estimated before the RRL observation considering the 843 MHz flux densities. For example G302.4-0.1, has the 843 MHz peak flux density of

[5]The resolution of an array decreases linearly with its size.

[6]This is the effective continuum bandwidth, which corresponds to the central 81.25% of the total bandwidth of 16 MHz.

[7]The ATCA web page is located at http://www.narrabri.atnf.csiro.au

Parameters of the ATCA observations :

Velocity rest frame	: Local Standard of Rest
Rest frequency (GHz)	: 5.2937332
Start channel	: 1
Number of channels	: 512
Start frequency (GHz)	: 5.3010000
Frequency increment (kHz)	: −31.3
Start velocity (km s^{-1})	: −391.297
End velocity (km s^{-1})	: 515.626
Velocity increment (km s^{-1})	: 1.770
ATCA configuration	: 0.750A (with antenna 6)
Primary beam HPBW	: 10'
Flux density calibrator	: B1934-683
Phase calibrator (day1)	: B1740-517
Phase calibrator (day2)	: B0537-441, B1549-790
Bandpass calibrator	: B1934-683
Observing date	: 1998, Apr 2 and Apr 3
Observer	: A. Green, L. Cram

Table 2.1 Parameters of the ATCA observations

100 mJy/beam. This flux density will be reduced to about 15 mJy/beam when the size of the synthesised beam is reduced from 43″ (the MOST beamsize) to about 16″ (the beam size of the 0.750A configuration), under the condition that the source has approximately flat spectrum (eg. a HII region) and the integrated flux density does not change with frequency. Comparing this with the theoretical rms noise in the image, the signal to noise ratio can be estimated.

2.4.3 Largest angular scale

The apparent brightness of an extended emission region will also depend on how well the visibility function is sampled by the observation. The shortest baseline length that has to be present in the data to image a source of size θ (source diameter in arcsec) is determined by $91000/\theta$ (in units of λ) (Bridle 1994) [10].

Using this formula it can be calculated that for a source with a diameter of 2′ the shortest projected baseline needed is 45.5 m, while 91 m is enough for a 1′ source.

The shortest baseline in the 0.750A ATCA configuration is 77 m, which means that sources like eg. G358.6+0.1 (SgrE19) will be adequately imaged. However, due to gaps in (u,v) coverage corresponding to missing interferometer short spacings, only central part of an extended ($\theta > 1'$) source will be imaged. As a result, the

measured total flux density of the largest sources is expected to be reduced.

2.4.4 Imaging

This section describes imaging techniques used to produce continuum images and line spectra of the selected sources.

To detect and measure the $H107\alpha$ line emission from the low-brightness sources, observed in this experiment, many synthesis imaging parameters have to be adjusted to achieve an optimal sensitivity and increase the signal-to-noise ratio. To detect the faintest expected RRL emission (2% of the continuum flux density integrated over the source), or to eliminate the possibility that there is any significant RRL emission, the signal to noise ratio measured in each channel, before the continuum subtraction, has to be at least 150.

The required sensitivity has not been achieved in some of the observed sources because of the fact that the same observing technique was used for sources with relatively wide range of characteristics, including their sizes and surface brightness. However, this was done intentionally, to test and refine the observing parameters before observing a larger sample.

The detected visibilities were calibrated and imaged using *miriad* synthesis imaging package. Flux density and bandpass calibration was carried out using observations of B1934-638, while three secondary calibrators were used to correct for changes in gain and phase caused by receiver and atmospheric instabilities. The calibrators with their total observing time and nominal flux densities at 4.8 GHz are shown in Table. 2.2.

Calibrator	Observing time	Flux density at 4.8 GHz
B1934-683	22 min	6.28 Jy
B0537-441	25 min	4.41 Jy
B1549-790	45 min	5.01 Jy
B1740-517	78 min	3.98 Jy

Table 2.2 The calibrators

After calibration the detected visibilities were imaged using the *miriad* task *invert* to produce a data cube of each source, a series of single channel, two-dimensional images at each of the frequencies, corresponding to the central 350 channels[8]. The cubes were then deconvolved using the tasks *clean* and *restor*. The continuum images were produced by averaging all individual channel images in a data cube. The line spectra are displayed as the integrated flux density versus the velocity (LSR)[9]. The

[8]The first and the last 80 channels have been discarded because of the gain instability.

[9]Local Standard of Rest - a velocity rest frame corrected for the *standard Solar motion* ($\leq 20 kms^{-1}$), a systematic motion of Sun relative to nearby stars.

frequency at which a spectral line is observed is associated with the radial velocity of the emitting source relative to the observer, using the formula for the Doppler effect:

$$v = c\frac{\nu_0 - \nu}{\nu_0}, \tag{2.3}$$

where ν_0 and ν are the rest frequency of the line, and the observing frequency, respectively.

A slightly different data reduction technique had to be used for each of the observed fields because of their different characteristics. To obtain an optimal signal to noise ratio, in some of the images, the visibilities using the baselines with the antenna 6 were excluded from the data, and the tapering functions of different FWHM were tested, to further increase the beam size. However, it was found that the best signal to noise ratio was obtained by applying the untapered natural weighting. Applying a Gaussian taper of a FWHM that matches the size of the source reduced the apparent flux density significantly, decreasing the signal to noise ratio. This flux density decrease is, probably, due to the inadequate (u, v) coverage. In some of the images the rms noise has been further reduced by increasing the single channel bandwidth, by averaging two, or sometimes more channels. However, this procedure has reduced the velocity resolution.

After an optimal signal to noise ratio was obtained the data cubes without the continuum contribution have been produced. The continuum emission has been subtracted in the (u, v) plane using the *miriad* task *uvlin*, which fits a low order polynomial to the line-free channels of a spectrum, representing the continuum.

Spectra of the sources with no detected line emission are presented without subtracting the continuum emission to show the optimal signal to noise ratio achieved.

2.5 Possible x-ray identifications

X-ray catalogues have been searched to find potential x-ray counterparts of the selected sources.

The Rosat All Sky Survey Bright Source Catalogue (Voges et al. 1999) [118] is derived from from the all-sky survey performed during the first half year of the ROSAT mission. It contains 18 811 sources down to a limiting count-rate of 0.05 cts/sec in the 0.1-2.4 keV energy band. For 94% of the sources visual inspection confirmed the detections.

The ROSAT All Sky Survey Faint Source Catalogue (Voges et al. 2000) [119] is the faint extension to the ROSAT Bright Source Catalogue.

The Second ROSAT Source Catalogue of Pointed Observations with the Position Sensitive Proportional Counter (ROSAT Consortium) [85] contains arcsec positions and count rates of 95 331 detected sources and covers 14.5% of the sky.

No catalogued x-ray source has been found in the vicinity of the selected sources (within 15′), except for G282.8-1.2. An x-ray source (J101123.3-574149) close to the position of G282.8-1.2 has been found in the The Second ROSAT Source Catalogue

(ROSAT Consortium) [85]. This x-ray source is close to the position of G282.8-1.2 with an offset of $2'$ and almost on the edge of the source. This could indicate a possible x-ray emission from G282.8-1.2.

Chapter 3

Results and Discussion

This chapter presents and discusses the results (843 MHz data, infrared data, and ATCA observations) and offers tentative conclusions about each of the selected objects.

3.1 843 MHz flux densities and sizes

Flux densities and sizes at 843 MHz, measured from the original MGPS images, are listed in Table 3.1. Listed peak flux densities and sizes have been determined after fitting the sources by Gaussians (using IMFIT) and measuring peaks and widths at half intensity of the equivalent deconvolved Gaussian sources (the major and minor axes and position angles are listed). Integrated flux densities have been measured using a summation of the pixel values. The error of this measurement has been estimated by measuring the integrated flux, by the same method, in several regions surrounding the source. The integrated intensities in the control, source-free regions have been fit to a constant offset and the error calculated from this fit was about 5%.

3.2 FIR to radio ratio

The properties of the 60μm far-infrared emission of the selected sources are summarised in Table 3.2, which gives the MOST source name, the IRAS source name, position, and 60 μm flux density. Table 3.2 also lists calculated values, $R_{843\,\mathrm{MHz}} = S_{60\mu m}/S_{843\,\mathrm{MHz}}$ and the offset r between the radio and the IRAS source. The last column gives the IRAS catalogue in which the source has been found.

The comparison of the infrared and radio emission of the sources selected for this project reveal objects with a wide range of $R_{843\,\mathrm{MHz}}$, from $\sim$1 (G282.8-1.2) to $>$ 1000 (G337.4-0.4, G358.6+0.1). According to the studies of Whiteoak and Green (1996) [126] these extremely low and high ratios of FIR/radio emission can be used as a diagnostic tool to distinguish SNRs and HII regions. However, the intermediate values of $R_{843MHz} \sim 500$ are inconclusive and other tests need to be applied.

Source name	Peak position J2000	Peak flux (mJy/beam)	S (mJy)	Size (deconv.)	p.a (degree)
G267.9-1.1	08:59:05 -47:30:52	8350	63600	$2.5' \times 2.0'$	20
G282.8-1.2	10:11:15 -57:44:02	219	680	$1.6' \times 1.2'$	1
G302.4-0.1	12:47:04 -62:58:25	105	370	$1.4' \times 1.4'$	-86
G304.5-0.1	13:04:56 -62:50:56	148	760	$1.9' \times 1.6'$	87
G313.8+0.7	14:20:42 -60:15:53	239	660	$1.3' \times 1.3'$	78
G323.8+0.0	15:31:04 -56:14:29	176	550	$1.5' \times 1.3'$	-2
G331.7-0.1	16:13:06 -51:17:41	252	390	$1.1' \times 1.0'$	19
G337.4-0.4	16:38:54 -47:26:29	426	1270	$1.7' \times 1.4'$	60
G358.6+0.1	17:42:05 -30:03:57	367	380	$1.4' \times 0.8'$	-1

Table 3.1 Flux densities and sizes of the selected sources at 843 MHz. The error of the integrated flux measurements is about 5%.

Radio source	IRAS source	IRAS position	r ($'$)	$S_{60\mu m}$ (Jy)	$R_{843\,\mathrm{MHz}} = S_{60\mu m}/S_{843\,\mathrm{MHz}}$	Cat.
G282.8-1.2	-			< 0.6	~ 1	
G302.4-0.1	12440-6242	12:47:04 -62:58:55	0.49	244	658	PSC
G304.5-0.1	X1301-625	13:04:53 -62:51:22	0.57			SSSC
G313.8+0.7	14170-6002	14:20:41 -60:16:02	0.20	396	598	PSC
G323.8+0.0	15272-5604	15:31:06 -56:14:31	0.28	295	534	PSC
G331.7-0.1	16093-5110	16:13:07 -51:17:49	0.23	297	756	PSC
G337.4-0.4	16352-4721	16:38:56 -47:26:57	0.59	3690	2915	PSC
G358.6+0.1	17388-3002	17:42:03 -30:04:11	0.45	455	1185	PSC

Table 3.2 The IRAS infrared data of the selected sources at 60 μm.

3.3 MIR to radio ratio

The properties of the 8.3μm mid-infrared emission of the selected sources are summarised in Table 3.3 which gives the catalogued 8.3 μm spatially integrated flux densities of all MSX point sources within the radio source area, for each of the MOST sources. The last column gives the value of $R = S_{8.3\mu m}/S_{843\,\mathrm{MHz}}$, where $S_{8.3\mu m}$ is the total flux of all MSX sources identified with the radio source. These ratios are only the lower limits, since the resolution of the MSX images is 18.3″ and the extended infrared emission is probably not fully imaged.

Source	$S_{8.3\mu m}$ (Jy)	$R = S_{8.3\mu m}/S_{843\,\mathrm{MHz}}$
G282.8-1.2	0.73	1.1
G302.4-0.1	1.53 0.29	4.9
G304.5-0.1	0.94 0.19 0.69 0.19	2.7
G313.8+0.7	0.67 1.93 0.48	4.7
G323.8+0.0	0.70 0.68 3.67	9.2
G331.7-0.1	0.79 0.14	2.4
G337.4-0.4	1.11 4.93 0.35 2.21 0.91	7.5
G358.6+0.1	2.13 0.42	6.7

Table 3.3 The MSX infrared data of the selected sources at 8.3 μm.

The results of the comparison of the mid-infrared and radio emission agree with the 60μm IRAS data - G282.8-1.2, which is not detected in 60μm, has the smallest MIR/radio ratio of only 1.1, while strong IRAS sources (eg. G337.4-0.4 and SgrE19) have significantly higher MIR/radio ratios.

3.4 Continuum and line emission at 5 GHz

Flux densities of the H107α line and continuum emission at 5 GHz are shown in Table 3.4. The line emission has been measured in the centre of the line (peak emission of the Gaussian fit), spatially integrated over the same source region as the continuum emission.

Source	S_C (mJy)	S_L (mJy)	T_L/T_C (%)	Peak mJy/beam	Beam (")
G267.9-1.1	103000±500	4300±200	4.2		
G282..8-1.2	106±7	<22	<20	45	26.69×11.90
G302.4-0.1	152±8	<24	<16	16	18.56×13.68
G304.5-0.1	137±8	<24	<17	14	18.75×13.62
G313.8+0.7	386±15	48±3	12.4	52	21.93×12.85
G323.8+0.0	250±9	<27	<10	32	21.32×13.56
G331.7-0.1	362±12	<36	<10	37	8.79×8.03
G337.4-0.4	259±9	<27	<10	35*	18.76×16.03
G358.6+0.1	367±11	38±4	9.6	158	8.81×8.36

Table 3.4 Flux densities of the selected sources of H107α and continuum emission at ~5 GHz. *The peak of the point source in the image of G337 is 90 mJy/beam.

3.5 Properties of the sources with detected line emission

The recombination lines can usually be characterised as Gaussian profiles with peak S_L, central velocity v and width at half-intensity Δv.

Table 3.5 lists measured and derived properties of the sources with detected line emission, after Gaussian fitting. Columns 1 - 3 give the source name, the integrated continuum flux at 5 GHz, and the line flux density at the centre of the line (the Gaussian peak) spatially integrated over the same region. The line to continuum ratio, S_L/S_{5GHz}, is given in column 4, while columns 5 and 6 give the line central velocity and the line width. The last three columns list derived properties; electron temperature T_e estimated from the line to continuum ratio and the line width, the distance to the emitting source estimated from the central velocity of the line v_{LSR}, and the velocity of a non-thermal motion called "micro-turbulence".

The electron temperatures T_e have been estimated from the line to continuum ratio and the line width, on an LTE approximation using:

$$\frac{T_e^*}{K} = [\frac{2.330 \cdot 10^4}{a(\nu,T)}(\frac{\nu}{GHz})^{2.1}\frac{1}{1+\frac{N_{He}}{N_H}}(\frac{\Delta\nu}{kHz})^{-1}(\frac{T_c}{T_L})]^{0.87}. \quad (3.1)$$

derived from (1.10). For the majority of Galactic HII regions, RRLs at $\nu > 1$ GHz are emitted under near-LTE conditions (Shaver 1980 [93], Roelfsema and Goss (1992) [82]) so that this estimate of T_e is often close to the true electron temperature.

The Gaussian shape of the RRL profiles is determined by the Doppler broadening, which usually consists of two components: a thermal broadening and a non-thermal motion (micro-turbulence). The thermal broadening is characterised by the electron temperature of the gas T_e, and its FWHM can be calculated by (1.7). The velocity v_t of the micro-turbulence within the gas can be calculated by subtracting this thermal broadening quadratically from the measured linewidth (1.8). This is listed in column 9 of Table 3.5.

If the radial velocities are dominated by differential Galactic rotation they can be used to estimate kinematic distances. The distances from the Sun to the emitting sources, listed in column 8, have been calculated using the best-fitting model for Galactic rotation (Fich et al. 1989) [36] and adopting standard IUA parameters for the orbital velocity of the Sun (220 kms^{-1}) and the Galactic centre distance (8.5 kpc).

Source name	S_C (mJy)	S_L (mJy)	S_L/S_C %	v_{LSR} (km/s)	Δv (km/s)	$T_{e,LTE}$ (K)	d (kpc)	v_t (km/s)
G267	103000±500	4300±300	4.2	3.0±3.4	35.1±4.3	7200±500	< 1.4	20
G313	386±15	48∓3	12.4	-53.4±5.2	26.5±5.2	3600±400	4.3±0.8 7.4±0.6	15
SgrE19	367±11	38±4	9.6	3.2±3.6	26.1±4.3	4300±600	< 1.0	16

Table 3.5 Measured and derived properties of the sources with detected $H107\alpha$ line emission.

3.6 Individual sources

3.6.1 G267.9-1.1

Source G267.9-1.1 has been observed as a test source. It is a well known HII region with a total flux of 160 Jy at 5 GHz, the averaged H109α and $H110\alpha$ line emission of 4.15% of the continuum, at velocity of +1 km s^{-1}, and a linewidth of about 34 km s^{-1} (Caswell and Haynes 1987) [19]. It has been identified with the optical nebula R38 (Rodgers et al. 1960) [81].

The MOST (843 MHz) continuum image of this source is shown at Figure 3.1. The source is surrounded by a "bowl" of apparently negative flux density. This is an artifact due to incomplete cleaning and deconvolution of bright, extended sources in the MGPS images (Green et al. 1999) [42]. This image was used to measure the integrated 843 MHz flux density of 63.6 Jy.

The 5 GHz flux density, measured from the ATCA continuum image is 103 Jy. This flux density is also reduced because the source is not fully imaged due to missing short interferometer spacings in the data. Only the central ($1' \times 1'$) part of this strong, extended ($2.5' \times 2.0'$ at 843 MHz) source has been detected in the ATCA image. Due to the partial imaging at 843 MHz and 5 GHz, because of the missing short spacings, no attempt has been made to calculate the spectral index.

Although, the IRAS source 08573-4718 catalogued in the IRAS Point Source Catalogue (Beichman et al. 1988) [7] and the IRAS Serendipitous Survey Catalogue (Kleinmann et al. 1986) [62] is in the vicinity of G267.9-1.1 its listed flux density is too low to represent the infrared integrated flux density of G267.9-1.1, since the extended infrared emission from this source is ignored in the PSC (Figure 2.1).

The ATCA observations confirmed the thermal nature of this source by detecting its H107α emission. The measurements (Table 3.5) agree with the results of Caswell and Haynes (1987) [19]. A strong (4.3 Jy) $H107\alpha$ line (Figure 3.2) has been detected at the velocity of 3.0$\pm$3.4 km s^{-1}. This small radial velocity is probably due to the Galactic rotation and can be used to estimate the distance to the source. Using one of the models of the Galactic rotation (Fich et al. 1989) [36] the distance to this HII region was estimated to be less than 1.4 kpc (d = 0.6 kpc in Caswell and Haynes 1987) [19]. The line to continuum ratio of 4.2% (not affected by the missing short spacings), and the linewidth of 35.1 km s^{-1} have been used to estimate the temperature of this HII region to be about 7200 K (7500 K in Caswell and Haynes 1987 [19]). The temperature has been calculated using formula (3.1), assuming an LTE condition. Figure 3.2 shows the spectrum of G267.9-1.1 after subtraction of the continuum emission.

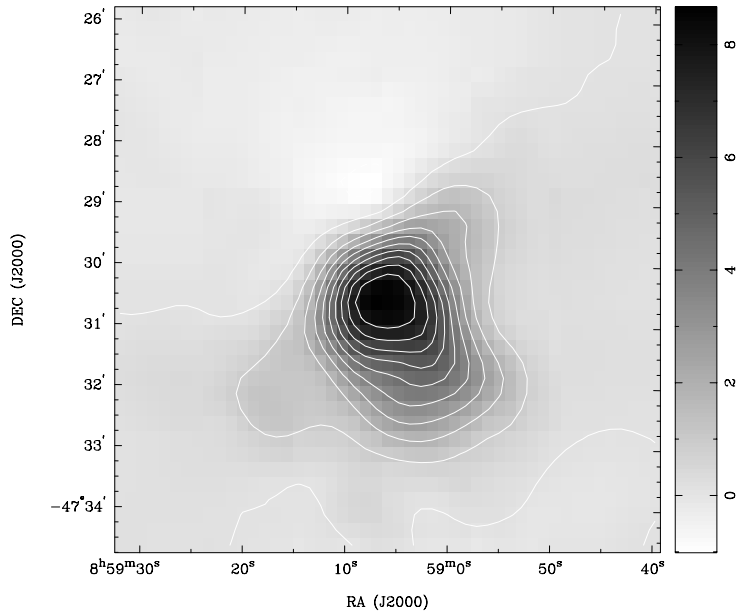

Figure 3.1 The MOST image of G267.9-1.1. Pixel map image: min/max=-1.02/8.67, range=0 to 8 Jy/beam (lin). Contour image: *contours* $\times$ 0.087 Jy/beam; contours: -10, 1, 10, 20, 30,40, 50, 60, 70, 80. Beam = $43'' \times 58''$.

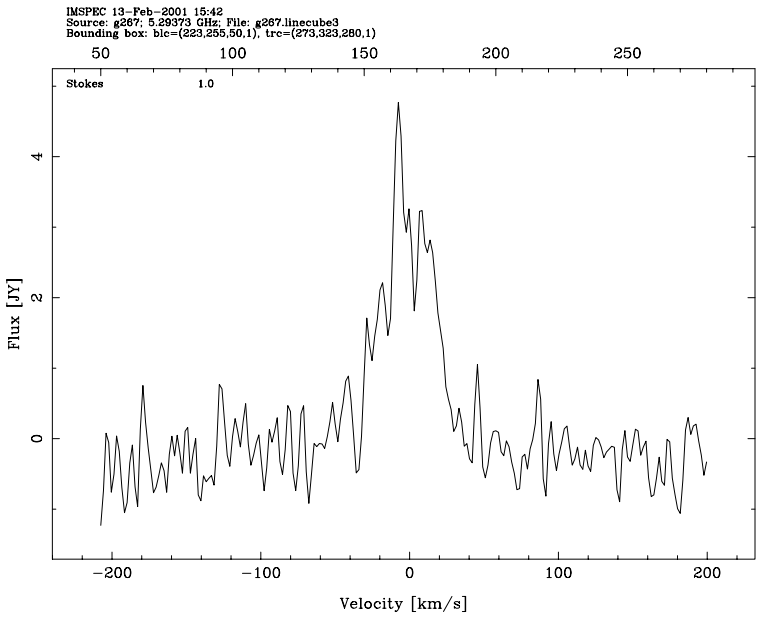

Figure 3.2 Integrated spectrum of G267.9-1.1 after the continuum subtraction, centred in the maximum of the H107α line emission. The line parameters determined after fitting with a Gaussian are listed in Table 3.5. The velocity axis has been Hanning smoothed over 3 channels. The continuum level appears to be negative due to incomplete imaging of this extended source.

3.6.2 G282.8-1.2

This source has been observed in the Parkes-MIT-NRAO 4.85 GHz Southern Survey and catalogued with a flux density of 391 mJy (Wright et al. 1994) [128]. It has also been catalogued in the Parkes-MIT-NRAO Catalogue of radio sources (Gregory et al. 1994) [51] with a flux density of 399 mJy at 4.85 GHz.

The MOST image of this source is shown at Figure 3.3. The 843 MHz flux density is 684 mJy. The size of the source is $1.6' \times 1.2'$, determined from the widths at half intensity of the equivalent deconvolved Gaussian source.

The spectral index of G282.8-1.2 has been estimated to be $\alpha = -0.31$, using the measurements from the Parkes catalogues (Wright et al. 1994 [128], Gregory et al. 1994) [51] at 4.85 GHz and the value of 684 mJy from the MGPS image at 843 MHz.

The ATCA continuum image at 5.293 GHz shows an irregular brightness distribution (Figure 3.4). The flux density of 106 mJy, measured from the continuum image, is reduced because short baseline data are missing and the extended features of this object have not been fully imaged.

No $H107\alpha$ emission has been detected above the sensitivity limit of $\Delta S = 22$ mJy (3σ), or above 20% of the continuum emission, averaged spatially over the detected region of the source (Figure 3.5). However, this non-detection is not significant, since the sensitivity is too low to allow an RRL to be detected.

No IRAS source has been detected close to the position of G282.8-1.2. Figure 2.2 shows the IRAS 60μm image of the region surrounding G282.8-1.2 (Wheelock et al. 1991) [123], overlaid on the radio contours at 843 MHz with no significant infrared emission detected near the position of G282.8-1.2. Sensitivity limit of PSC (0.6 Jy/beam at 60μm) (Beichman et al. 1988) [7] implies $R = S_{60\mu m}/S_{843\,\mathrm{MHz}} \leq 1$. According to Whiteoak and Green (1996) [126], SNRs have $R_{843\,\mathrm{MHz}} = S_{60\mu m}/S_{843\,\mathrm{MHz}} < 50$. Estimated spectral index of G282.8-1.2 $\alpha = -0.31$ implies its flux density of about 650 mJy at 1 GHz. Using this value and the IRAS sensitivity limit of 0.6 Jy/beam, it can be estimated that $R_{1GHz} = S_{60\mu m}/S_{1GHz} \leq 1$, a value typically found in young (historical) Galactic remnants (CasA, Tycho, Kepler, Crab) (Arendt 1989) [4].

Only one MSX point source has been catalogued close to the position of G282.8-1.2 (Figure 2.7). The calculated ratio $R = S_{8.3\mu m}/S_{843\,\mathrm{MHz}} = 1.1$ suggests that the source is probably non-thermal (Cohen and Green 2001) [27], even if some extended emission from the infrared source was not fully imaged.

There is a possible x-ray counterpart of G282.8-1.2. The ROSAT source (J101123.3-674149) has been found in the The Second ROSAT Source Catalogue of Pointed Observations (ROSAT Consortium, 2001) [85]. This x-ray source has an offset of $2.4'$ from the radio peak emission and is close to the edge of G282.8-1.2.

The ratio of infrared to radio emission of G282.8-1.2 together with its relatively steep spectrum ($\alpha = -0.31$) and a possible x-ray emission suggest this source may be a young Galactic SNR. However, the ATCA H107α data are not conclusive and further, more sensitive RRL observations could confirm the non-thermal nature of this source (by not detecting an RRL emission above 2% of the continuum emission).

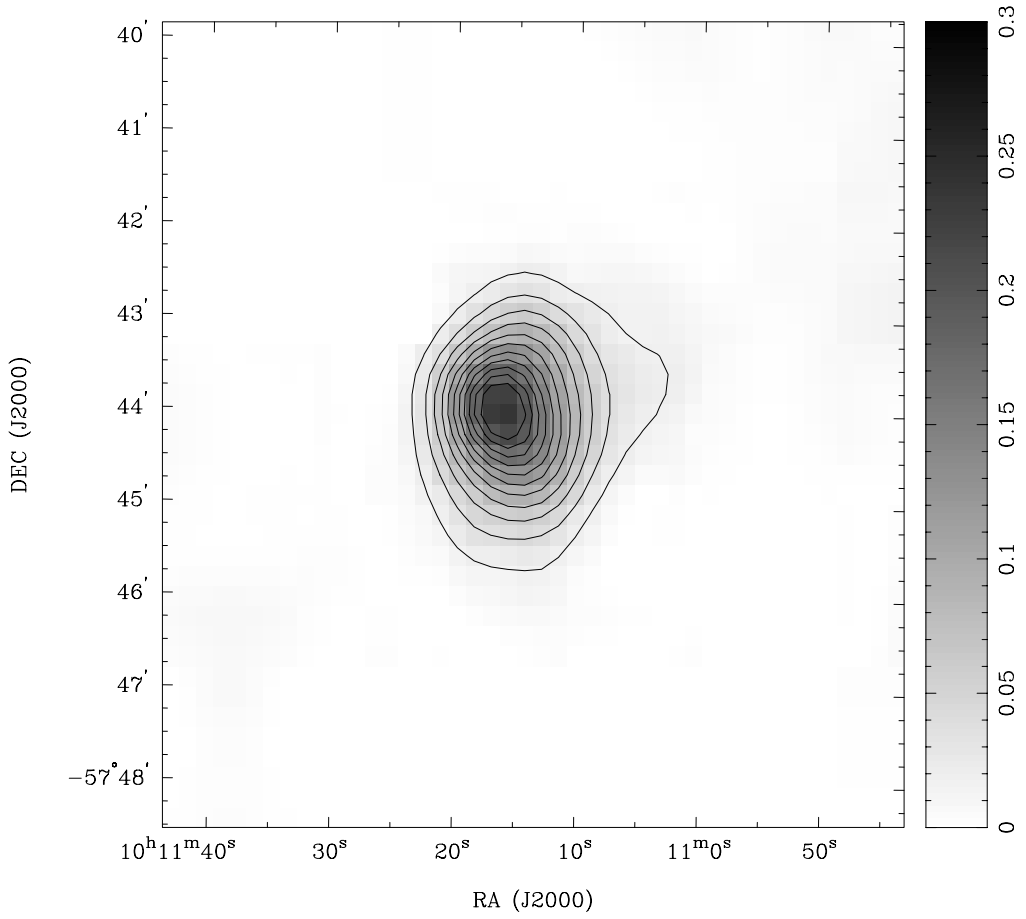

Figure 3.3 The MOST image of G282.8-1.2. Pixel map image: min/max = - 0.013 / 0.237, range=0 to 0.3 Jy/beam (lin). Contour image: *contours* $\times$ 9 $\times$ 10^{-3} Jy/beam; contours: 2, 4, 6, 8, 10, 12, 14, 16, 18, 20, 22. Beam = $43'' \times 51''$.

However, other tests are also needed to confirm this result.

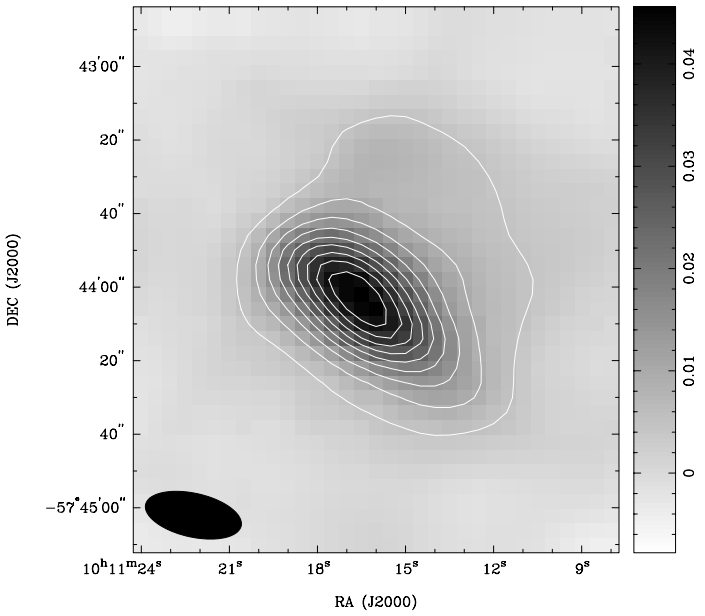

Figure 3.4 The ATCA image of G282.8-1.2. Pixel map image: min/max = -4 x 10^{-3} / 0.046; range -8 x 10^{-3} to 0.0456 Jy/beam (lin). Contour image: contours x 4 x 10^{-4} Jy/beam; contours: 10, 20, 30, 40, 50, 60, 70, 80, 90. The synthesised beam ($26.69'' \times 11.90''$) is shown on the left.

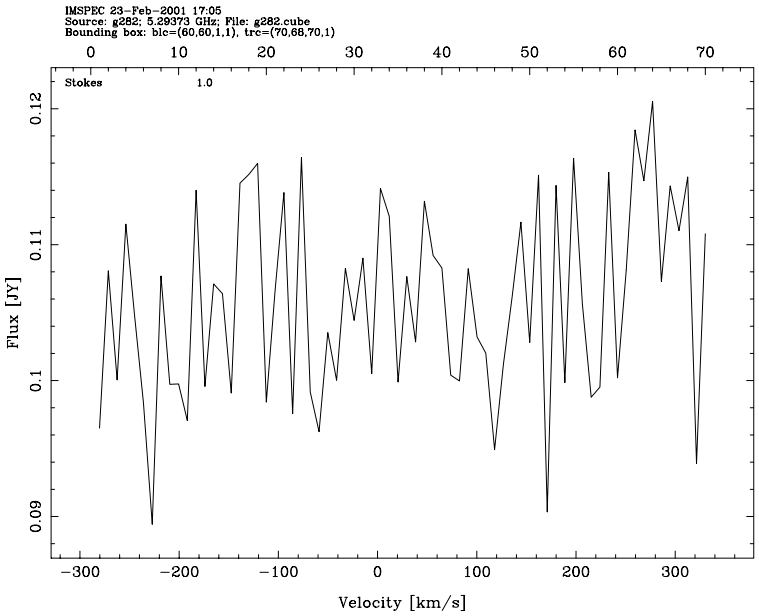

Figure 3.5 Integrated spectrum of G282.8-1.2. No line emission has been detected above the sensitivity limit of 22 mJy or $T_L < 0.2\ T_C$.

3.6.3 G302.4-0.1

No results of previous radio observations of G302.4-0.1 have been reported in the literature.

The MOST (843 MHz) image of this source is shown at Figure 3.6. The integrated flux density determined from the image is 370 mJy. After fitting by a Gaussian the deconvolved size of G302.4-0.1 has been estimated to be $1.4' \times 1.4'$.

The source has been identified with the IRAS source 12440-6242 (Figure 2.3) with an average non-colour corrected, spatially integrated flux density of 244 Jy at 60μm. Comparing the infrared and the 843 MHz radio emission, the ratio $R_{843\,\mathrm{MHz}}$ has been calculated to be 660.

The high-resolution MSX data have been used to calculate MIR/radio ratio of this source. There are two catalogued MSX point sources close to the position of G302.4-0.1 [$12^h47^m05^s$ $-62^o59'11''$ and $12^h47^m09^s$ $-62^o56'21''$ (J2000)] (Figure 2.8) and the total flux density of the infrared sources has been used to calculate $R = S_{8.3\mu m}/S_{843\,\mathrm{MHz}} > 4.9$. The value of $R = S_{8.3\mu m}/S_{843\,\mathrm{MHz}} = 27$ (with R in the range of 6.2 - 73.4) for Galactic HII regions found by Cohen and Green (2001) [27] is significantly greater but they used preliminary MSX data with $46''$ resolution, which better matched to the MOST data. Hence, the MSX data could classify this source as thermal, similarly to IRAS data.

The ATCA continuum image and spectrum of G302.4-0.1 are shown at Figure 3.7 and Figure 3.8, respectively. The integrated flux density measured from the continuum image is 150 mJy. No line emission has been detected above the sensitivity limit of about 24 mJy (16% of the continuum emission).

This source is extended and its flux density at 5 GHz has been measured only from the detected central region of the source. This prevents a determination of the total flux at 5 GHz and a global measurement of the spectral index. However, the spectral index of the brightest part of the source can be estimated since the 5 GHz observations do sample the scale of the MOST beam. For example, the mean flux density at 5 GHz averaged over an area of the MOST beam size, centred on the brightest part of G302.4-0.1, was measured to be 14 mJy/beam. This gives about 109 mJy integrated over the MOST beam area. Comparing this with the 843 MHz peak flux density of 105 mJy/beam the spectral index of the brightest part of the source was estimated to be $\alpha \sim 0$.

The FIR/radio and MIR/radio ratios and its flat spectrum could classify this source as thermal, probably Galactic HII region. However, as suggested by Arendt (1989) [4] and Chevalier (1982) [21] the ratio of far-infrared to radio emission increases as a SNR evolves, and can be as high as almost 1000 in SNRs as young as 2000 years. So, according to its size G302.4-0.1 could also be a 2000 year old Galactic SNR, but further, more sensitive RRL observations are needed to unambiguously determine thermal or non-thermal nature of this source (to detect the line emission or to confirm that there is no line emission above 2% of the continuum).

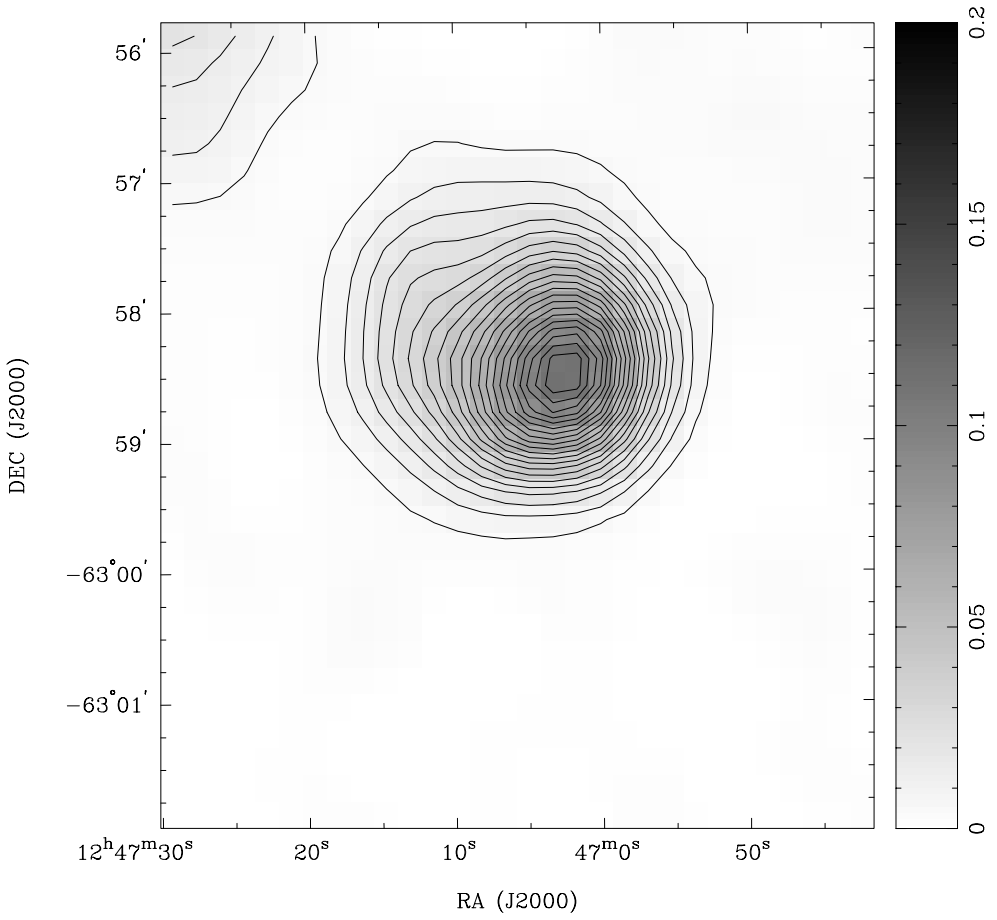

Figure 3.6 The MOST image of G302.4-0.1. Pixel map image: min / max=-2 x 10^{-3} / 0.110; range = 0 to 0.2, Jy/beam (lin). Contour image: contours x 2 x 10^{-3} Jy/beam; contours: 2, 4, 6, 8, 10, 12, 14, 16, 18, 20, 22, 24, 26, 28, 30, 32, 34, 36, 38, 40, 42. Beam = $43'' \times 48''$.

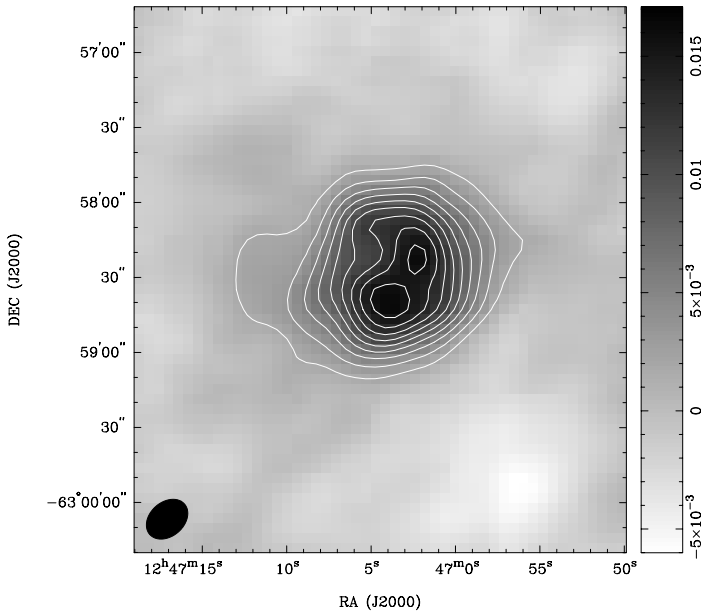

Figure 3.7 The ATCA image of G302.4-0.1. Pixel map image: min / max = -6 x 10^{-3} / 0.016; range -6 x 10^{-3} to 0.017 Jy/beam (lin). Contour image: contours x 2 x 10^{-4} Jy/beam; contours: 10, 20, 30, 40, 50, 60, 70, 80, 90. The synthesised beam ($18.56'' \times 13.68''$) is shown on the left.

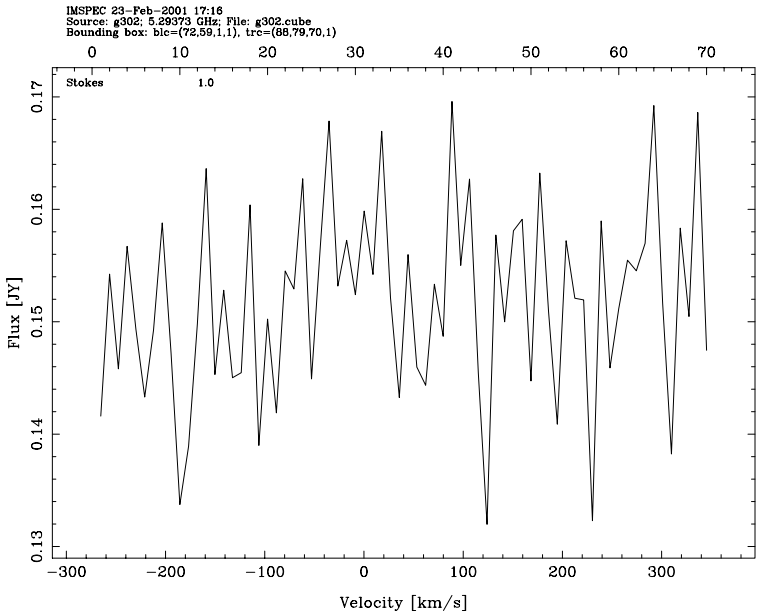

Figure 3.8 Integrated spectrum of G302.4-0.1. No line emission has been detected above the sensitivity limit of 24 mJy or $T_L < 0.16\ T_C$.

3.6.4 G304.5-0.1

No previous radio observations of G304.5-0.1 have been reported.

The MOST (843 MHz) image of this extended ($1.9' \times 1.6'$), low-brightness source is shown at Figure 3.9. The integrated flux density has been measured to be 760 mJy, with a peak at 148 mJy/beam, determined after fitting by a Gaussian.

Figure 3.10 and Figure 3.11 show the ATCA data. The flux density of 140 mJy, measured from the continuum image, is reduced because short baseline data are missing and the extended features of this object have not been fully imaged.

The 5 GHz integrated flux density, measured from the brightest part of the source was 100 mJy per MOST beam. Comparing this with the MGPS peak (148 mJy/beam) the spectral index of the central region of G304.5-0.1 was estimated to be $\alpha = -0.22$.

No $H107\alpha$ emission has been detected from this source, above the integrated channel sensitivity (3σ) of 24 mJy or above 17% of the continuum (Figure 3.11).

The far-infrared counterpart of this source (X1301-625) has been catalogued in the IRAS Small Scale Structure Catalogue (Helou and Walker 1988) [55]. The average non-colour corrected, spatially integrated flux density, measured at 100μm, is 1620 Jy (which gives $R = S_{100\mu m}/S_{843\,\mathrm{MHz}} = 2132$), but the 60 μm flux density of this extended infrared source is not listed in the catalogue.

There are four catalogued MSX point sources close to the position of this extended radio source. The total flux density of the infrared sources has been used to calculate $R = S_{8.3\mu m}/S_{843\,\mathrm{MHz}} > 2.7$. The morphology of the mid-infrared emission suggests a PAH halo surrounding the radio source (Figure 2.9), which is characteristic of HII regions (Cohen and Green 2001) [27].

However, further observations (more sensitive RRL, polarimetry, spectral index measurements) of this faint, extended source, are needed to determine if the source is thermal or non-thermal.

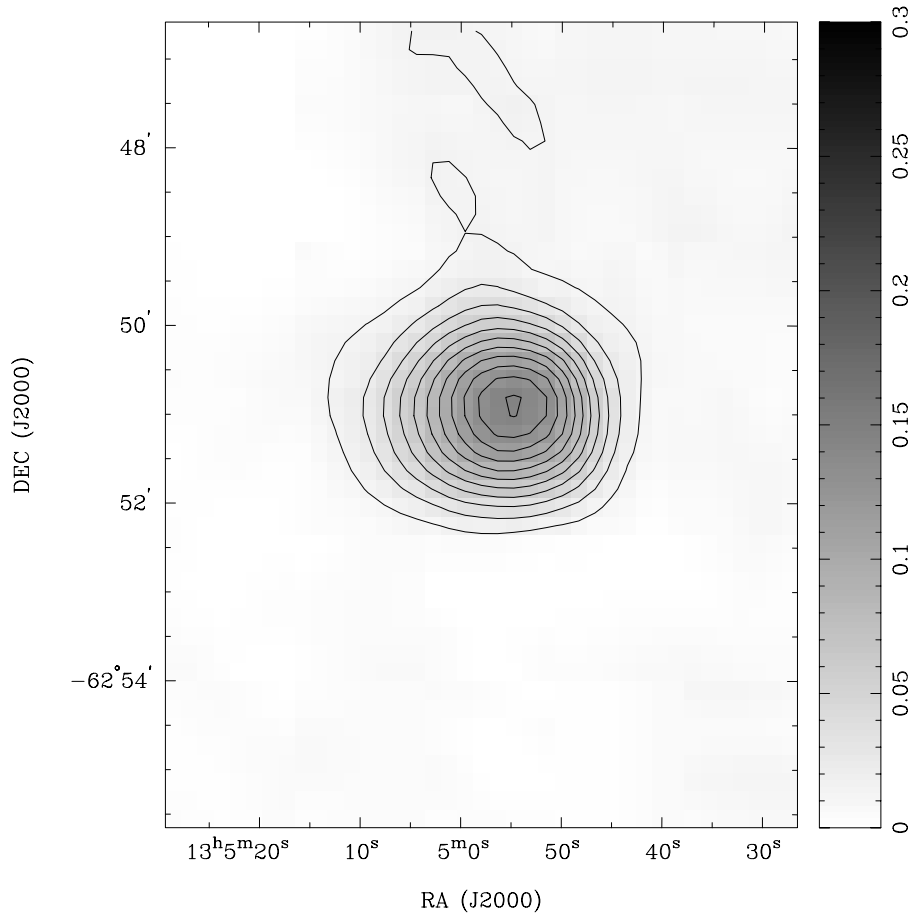

Figure 3.9 The MOST image of G304.5-0.1. Pixel map image: min / max = -0.010 / 0.140; range = 0 to 0.3, Jy/beam (lin). Contour image: contours x 6 x 10^{-3} Jy/beam; contours: 2, 4, 6, 8, 10, 12, 14, 16, 18, 20, 22. Beam = $43'' \times 48''$.

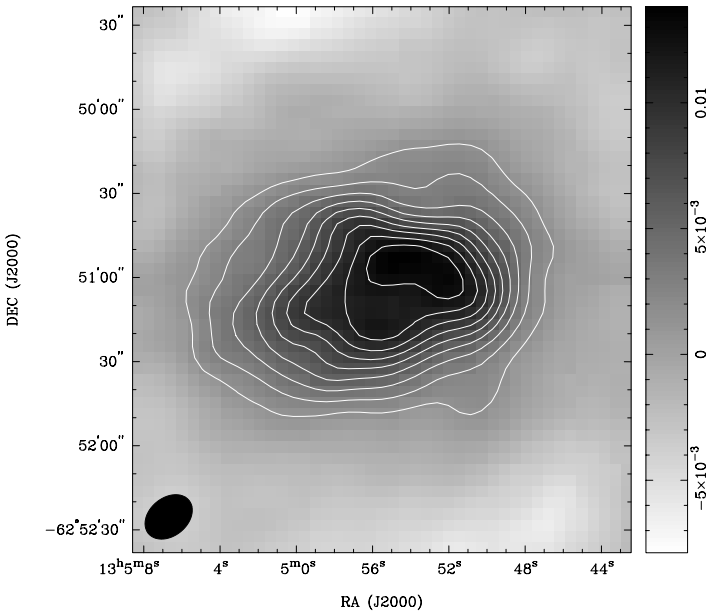

Figure 3.10 The ATCA image of G304.5-0.1. Pixel map image: min / max=-7 x 10^{-3} / 0.014; range -7 x 10^{-3} to 0.014 Jy/beam (lin). Contour image: contours x 1 x 10^{-4} Jy/beam; contours: 10, 20, 30, 40, 50, 60, 70, 80, 90. The synthesised beam ($18.75'' \times 13.62''$) is shown on the left.

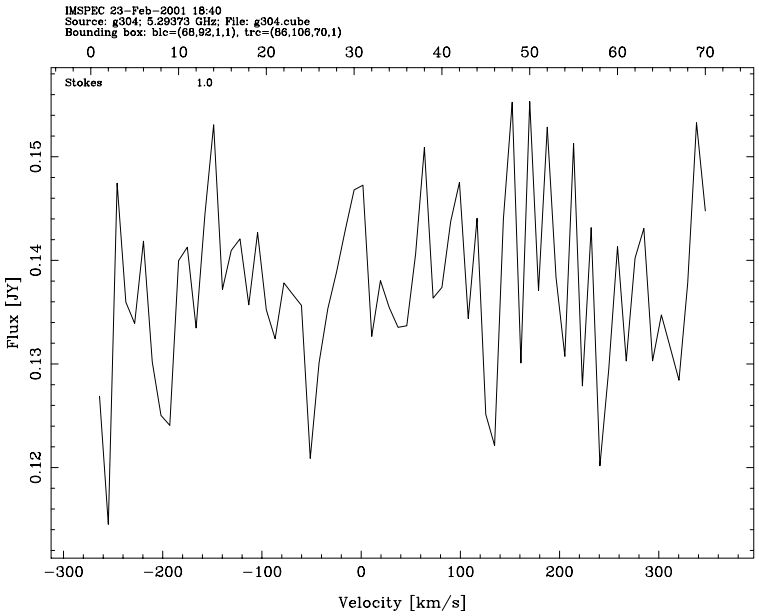

Figure 3.11 Integrated spectrum of G304.5-0.1. No line emission has been detected above the sensitivity limit of 24 mJy or $T_L < 0.17\ T_C$.

3.6.5 G313.8+0.7

This source has been listed in the Catalogue of 5 GHz Galactic Plane Sources (Haynes and Caswell 1979) [52] with a flux density of 650 mJy, and in the Parkes-MIT-NRAO 4.85 GHz (PMN) Southern Survey, with fluxes of 715 mJy or 626 mJy (measured using different methods) (Wright et al. 1994) [128].

The integrated flux of 660 mJy, at 843 MHz, measured from the MOST continuum image (Figure 3.12) suggests a flat spectrum radio source, with a spectral index $\alpha \sim 0$.

The 5 GHz integrated flux density, measured only from the detected central region of this extended source (Figure 3.13) is 390 mJy.

The integrated flux density at 5 GHz over an area size of the MOST beam (233 mJy) compared with the 843 MHz peak (239 mJy/beam) gives the spectral index of the brightest part of the source $\alpha \sim 0$.

The spectrum of G313.8+0.7 (Figure 3.14), integrated over the source area, shows relatively strong $H107\alpha$ line emission, centred at the velocity of -53.4 $\pm$5.2 kms^{-1}. This velocity indicates an HII region at the distance of 4.3 $\pm$ 0.8 or 7.4 $\pm$ 0.6 kpc, ambiguity being the result of its position within the solar circle (Schmidt 1965) [89]. The line to continuum ratio of 12.4%, and the linewidth of 26.5 km s^{-1} have been used to calculate quite a low electron temperature of only 3600 K. Such a low value of the electron temperature is characteristic of HII regions which are close to the Galactic Centre and can satisfactorily be fitted by the "galactic gradient" of T_e, derived from studies of Shaver et al. (1983) [94] or Caswell and Haynes (1987) [19]. The velocity of the non-thermal motion within the gas (micro-turbulence) has been estimated to be $v_t = 15$ km s^{-1}.

The source has been identified with the IRAS source 14170-6002, with the average non-colour corrected, spatially integrated flux density of 396 Jy, measured at 60μm (Figure 2.4).

There are three catalogued MSX point sources close to the position of G313.8+0.7. The total flux density of the infrared sources has been used to calculate $R = S_{8.3\mu m}/S_{843\,\mathrm{MHz}} > 4.7$, which is in agreement with the IRAS data.

The infrared (60μm) to radio (843 MHz) ratio of 600, together with its estimated flat spectrum, would classify this source as being most likely an HII region, which is unambiguously confirmed by the detection of the RRL emission in this survey.

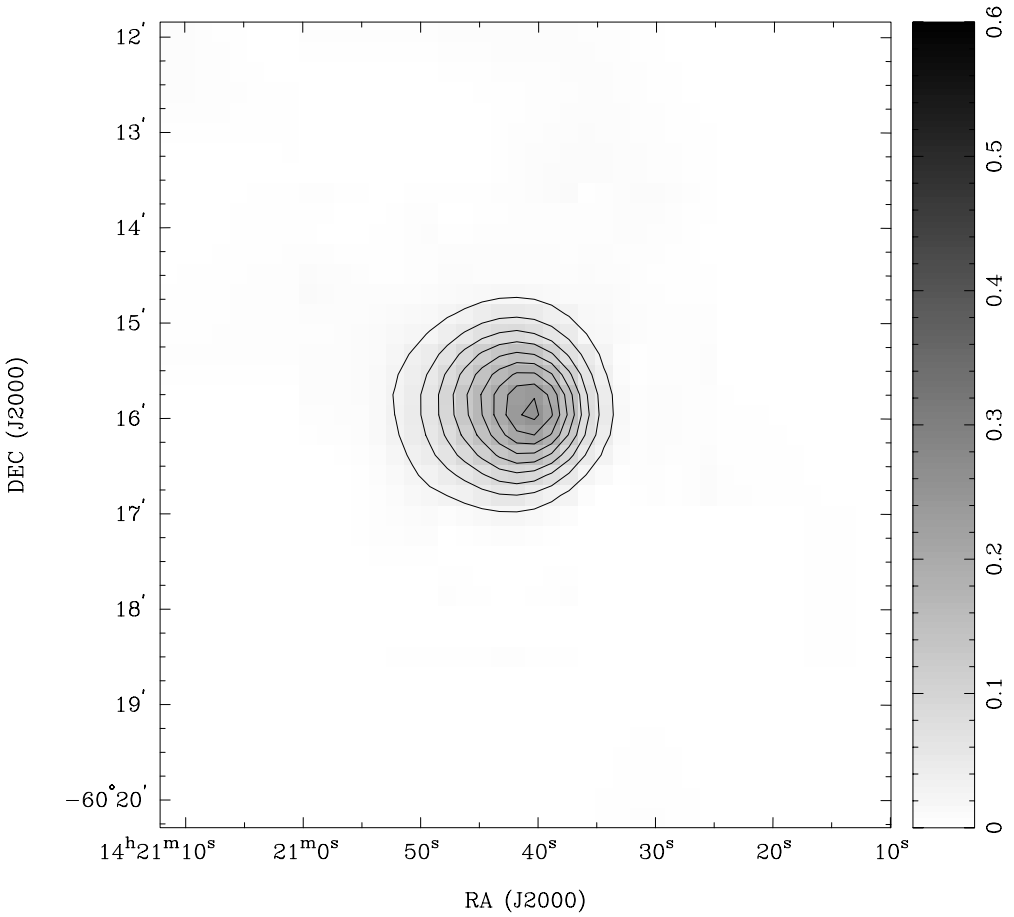

Figure 3.12 The MOST image of G313.8+0.7. Pixel map image: min / max = -8 x 10^{-3} / 0.25; range=0 to 0.6, Jy/beam (lin). Contour image: contours x 0.013 Jy/beam; contours: 2, 4, 6, 8, 10, 12, 14, 16, 18, 20. Beam = $43'' \times 50''$.

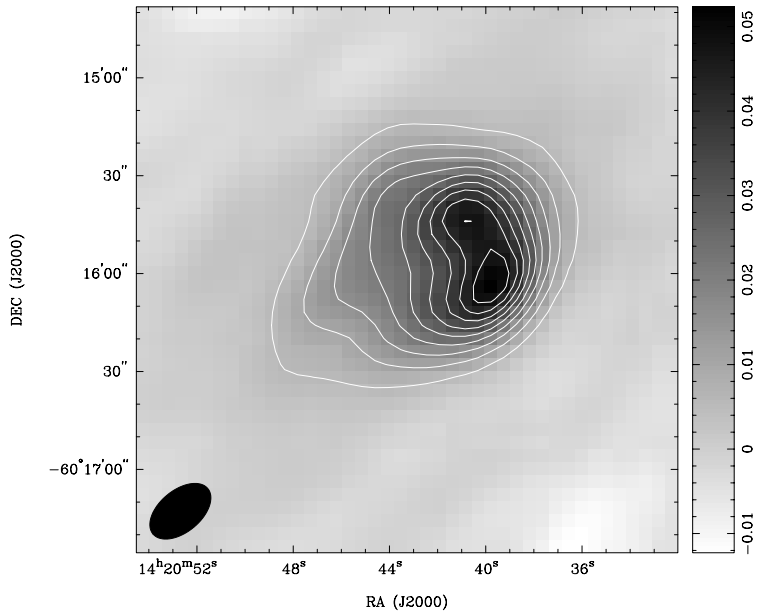

Figure 3.13 The ATCA image of G313.8+0.7. Pixel map image: min / max = -0.012 / 0.052; range -0.012 to 0.052 Jy/beam (lin). Contour image: contours x 5 x 10^{-4} Jy/beam; contours: 10, 20, 30, 40, 50, 60, 70, 80, 90. The synthesised beam ($21.93'' \times 12.85''$) is shown on the left.

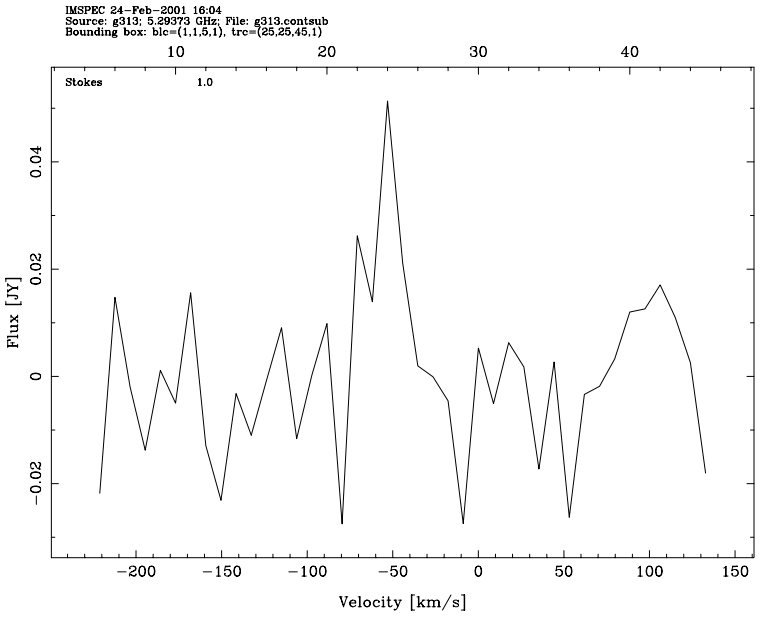

Figure 3.14 Integrated spectrum of G313.8+0.7, after the continuum subtraction, centred in the maximum of the H107α line emission. The line parameters determined after fitting by a Gaussian are listed in Table 3.5.

3.6.6 G323.8+0.0

No catalogued radio source has been found in the vicinity of $15^h31^m04^s$ $-56^o14'29''$ (J2000), the position of the peak emission of G323.8+0.0 at 843 MHz. The integrated flux density of this source measured from its MOST image (Figure 3.15) is 550 mJy.

The ATCA continuum image and spectrum of G323.8+0.0 are shown at Figure 3.16 and Figure 3.17, respectively. The integrated flux density measured from the detected central region of this extended source ($1.5' \times 1.3'$ at 843 MHz) is 250 mJy. The MOST and the ATCA image reveal the same morphology, showing an irregular brightness distribution with the brightest radio emission occurring in the north-western quarter of the source.

The integrated flux density at 5 GHz over an area size of the MOST beam (137 mJy) compared with the 843 MHz peak (176 mJy/beam) gives the spectral index of the brightest part of the source $\alpha = 0.14$.

No $H107\alpha$ line emission has been detected above the integrated channel (3σ) sensitivity limit of $\Delta S = 27$ mJy or above 10% of the integrated flux density of the continuum emission.

The infrared counterpart of G323.8+0.0, the IRAS source 15272-5604 (Figure 2.5), has a non-colour corrected, spatially integrated flux density of 295 Jy, measured at 60μm. The ratio $R = S_{60\mu m}/S_{843\,\mathrm{MHz}}$ of 530 indicates a thermal nature of this source, which is also suggested by its IRAS 60μm/12μm and 25μm/12μm flux density ratios larger than 19.3 and 3.7, respectively, which are believed to be characteristics of compact HII regions (Wood and Churchwell 1989) [127].

The thermal nature of this source has also been suggested by the MSX data (Figure 2.10). The lower limit of the ratio $R = S_{8.3\mu m}/S_{843\,\mathrm{MHz}}$ of 9.2 is the highest in the sample.

However, more sensitive RRL observations are required to detect line emission and determine properties of this Galactic HII region.

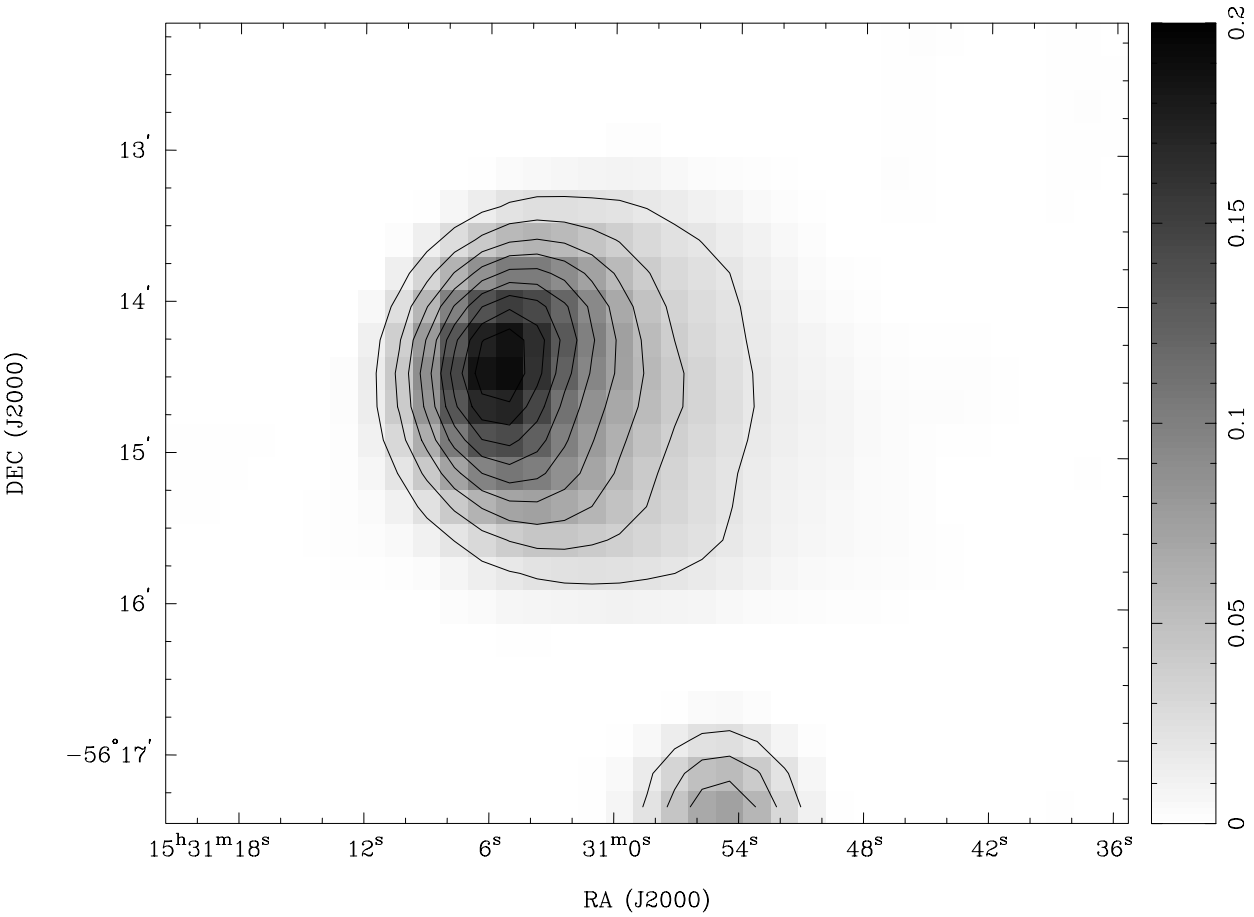

Figure 3.15 The MOST image of G323.8+0.0. Pixel map image: min / max = -8 x 10^{-3} / 0.190; range = 0 to 0.2, Jy/beam (lin). Contour image: contours x 10 x 10^{-3} Jy/beam; contours: 2, 4, 6, 8, 10, 12, 14, 16, 18, 20. Beam = $43'' \times 52''$.

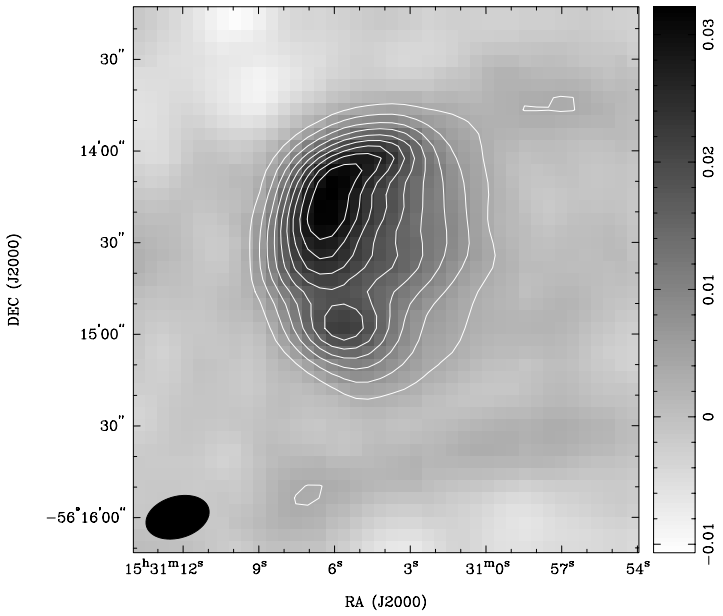

Figure 3.16 The ATCA image of G323.8+0.0. Pixel map image: min / max = -0.011 / 0.032; range -0.010 to 0.032 Jy/beam (lin). Contour image: contours x 3 x 10^{-4} Jy/beam; contours: 10, 20, 30, 40, 50, 60, 70, 80, 90. The synthesised beam ($21.32'' \times 13.56''$) is shown on the left.

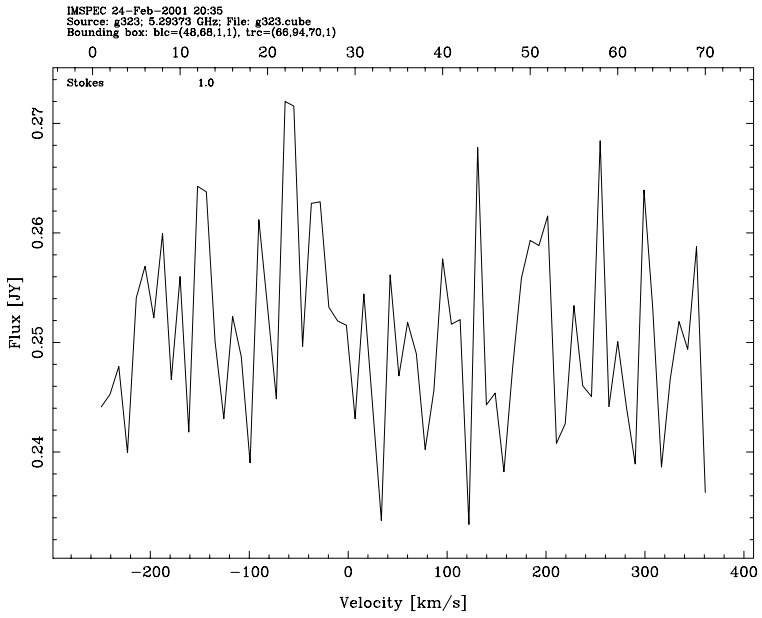

Figure 3.17 Integrated spectrum of G323.8+0.0. No line emission has been detected above the sensitivity limit of 27 mJy or $T_L < 0.10\ T_C$.

3.6.7 G331.7-0.1

No catalogued radio source has been found close to the position of G331.7-0.1. The MOST image of this source is shown at Figure 3.18. The 843 MHz integrated flux density of G331.7-0.1 is 390 mJy. After fitting the source by a Gaussian, its peak has been measured to be 297 mJy/beam, with the major and minor FWHM of $1.1' \times 1.0'$.

The ATCA image of G331.7-0.1 is shown at Figure 3.19. Fitting this image by a Gaussian gives the size of $40'' \times 26''$, with a peak emission at 25 mJy/beam. The integrated flux density at 5 GHz is 360 mJy. This small diameter source has been fully imaged at 5 GHz.

The 843 MHz and the 5 GHz flux densities of G331.7-0.1 have been used to estimate its spectral index $\alpha \sim 0$.

No $H107\alpha$ recombination line emission has been detected above the sensitivity limit of 36 mJy (10% of the continuum emission) (Figure 3.20). There is a very narrow feature, which looks like a narrow absorption line, at about 200 km s^{-1}. This could be the result of an artifact in the CLEANed map, probably due to low signal to noise ratio. That was confirmed after examining the "dirty map" (Figure 3.21) in which this narrow line is not present. However, there is a possible 2σ detection at about -90 kms^{-1} (not listed in Table 3.5), with a width consistent with the expected width for RRL emission. In addition, this velocity can be interpreted as the radial velocity of the Galactic rotation, which gives the distance to the source of about 5-10 kpc. However, more sensitive observations are needed to confirm this detection.

This source has been identified with the IRAS source 16093-5110, found in the IRAS Point Source Catalogue (Beichman et al. 1988) [7] with a flux density of 297 mJy at 60μm. Comparison with the 843 MHz flux density gives a ratio $R = S_{60\mu m}/S_{843\,\mathrm{MHz}}$=760, typically found in Galactic HII regions.

However, the high resolution MSX data are inconclusive. The lower limit of the MIR/radio ratio of 2.4 is significantly bellow the expected value for HII regions (Cohen and Green 2001) [27] but this may be due to the fact that the extended infrared emission was not fully imaged.

This flat spectrum source with a significant far-infrared emission is most probably a Galactic HII region. This is also suggested by a possible (2σ) RRL detection. However, the MSX data are inconclusive and more sensitive RRL observations and other tests are needed to confirm this result.

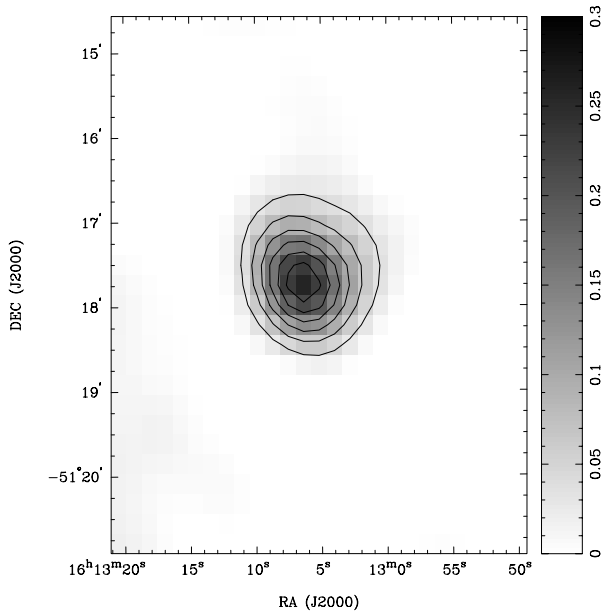

Figure 3.18 The MOST image of G331.7-0.1. Pixel map image: min / max = -0.034 / 0.257; range = 0 to 0.3, Jy/beam (lin). Contour image: contours x 0.037 Jy/beam; contours: 1, 2, 3, 4, 5, 6. Beam = $43'' \times 55''$.

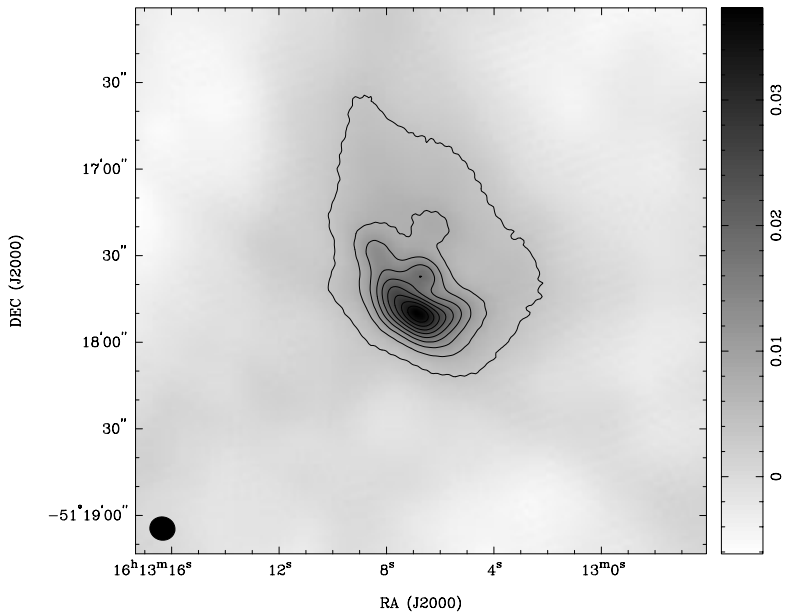

Figure 3.19 The ATCA image of G331.7-0.1. Pixel map image: min / max = -6 x 10^{-3} / 0.04; range -6 x 10^{-3} to 0.04 Jy/beam (lin). Contour image: contours x 4 x 10^{-4} Jy/beam; contours: 10, 20, 30, 40, 50, 60, 70, 80, 90. The synthesised beam ($8.79'' \times 8.03''$) is shown on the left.

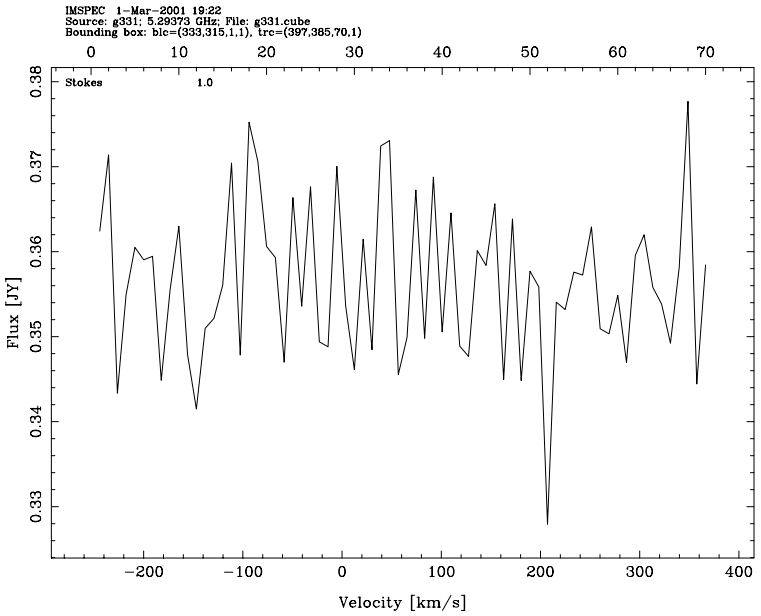

Figure 3.20 Integrated spectrum of G331.7-0.1. No line emission has been detected above the sensitivity limit of 36 mJy or $T_L < 0.10\ T_C$. The narrow line at about 200 km s^{-1} is, most probably, an artifact of CLEANing, due to low signal/noise ratio.

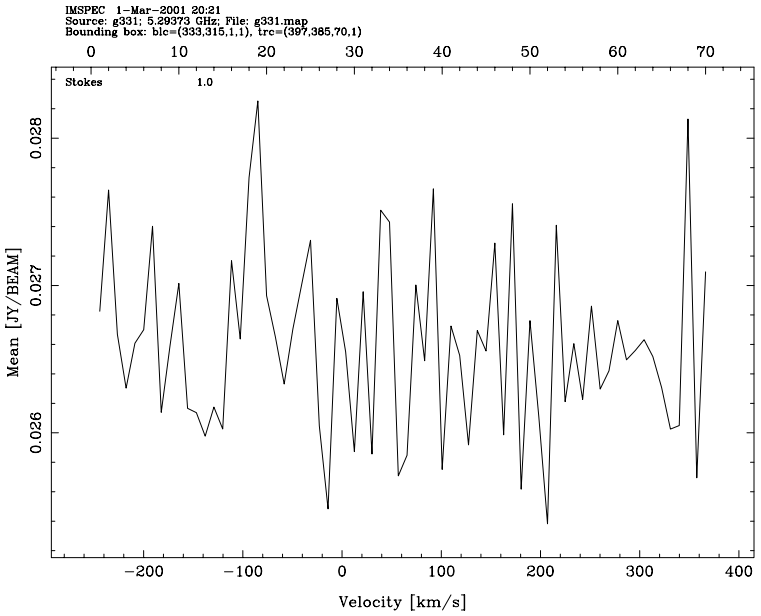

Figure 3.21 Spectrum of G331 showing the mean (mJy/beam) of the dirty map of G331.7-0.1. The narrow line is not present. There is a 2σ detection at about -90 km s^{-1}.

3.6.8 G337.4-0.4

Figure 3.22 shows the MOST (843 MHz) image of this extended ($1.7' \times 1.4'$) source, with an integrated flux density of 1270 mJy, and a peak emission of 426 mJy/beam at a position of $16^h38^m54^s$ $-47^o26'29''$ (J2000).

The ATCA image (Figure 3.23) shows the detected region of this source at 5.29 GHz around the ATCA pointing $16^h38^m57^s$ $-47^o26'55''$ (J2000). In the south-eastern part of the ATCA image there is a point-like source, not visible at the MOST image of G337.4-0.4. The point source has an integrated flux density of 94 mJy and a peak (91 mJy/beam) at $16^h38^m50^s$ $-47^o28'02''$ (J2000). Figure 3.24 shows the ATCA image of G337.4-0.4 with a point source, overlaid on the MOST (843 MHz) radio contours of G337.4-0.4. The ATCA image has been convolved with the MOST beam (Figure 3.25), showing the point source with a peak at the same position. So, if the point source has an approximately flat spectrum, it would be visible at the MOST image. However, considering the sensitivity of the MGPS (1σ = 1−2 mJy/beam), an extremely inverted spectrum ($\alpha > 1.5$) source would not be visible at 843 MHz. Alternatively, it has been suggested that the point source could be a transient radio source (an x-ray binary). In fact, the point source is very close to a known transient source 4U1630-47, which was active at the time of the ATCA observation (3 April, 1998) and the separation of the two sources was at the margin of the resolution limit of the BATSE (Hunstead 2001) [57].

The integrated flux density at 5 GHz over an area size of the MOST beam (164 mJy) compared with the 843 MHz peak (426 mJy/beam) gives the spectral index of the extended part of G337.4-0.4 $\alpha = -0.53$, which indicates a steep spectrum source.

No H107α line emission has been detected above the sensitivity limit of 27 mJy or above 10% of the detected integrated flux density of the continuum emission (259 mJy) (Figure 3.26).

Figure 2.6 shows the 60μm IRAS image of the IRAS PSC source 16352-4721, identified with G337.4-0.4. The ratio $R = S_{60\mu m}/S_{843MHz}$ of 2915 is the highest in the sample. Such high ratios of infrared to radio emission can be found in compact Galactic HII regions because a much larger fraction of the ionising radiation from the central star is absorbed by dust than in extended HII regions (Whiteoak et al. 1994) [125].

The source has been identified with five MSX point sources (Figure 2.11) with the total flux density of 9.51 Jy at 8.3μm. Comparing the infrared and the 843 MHz radio emission, the ratio $R = S_{8.3\mu m}/S_{843\,\mathrm{MHz}}$ has been calculated to be > 7.5, suggesting a thermal source.

Further observations are needed to determine the nature of this interesting source with relatively steep spectrum but high infrared to radio ratios, including the investigation of a transient or an extreme inverted spectrum source observed with the ATCA but not seen on the MOST image.

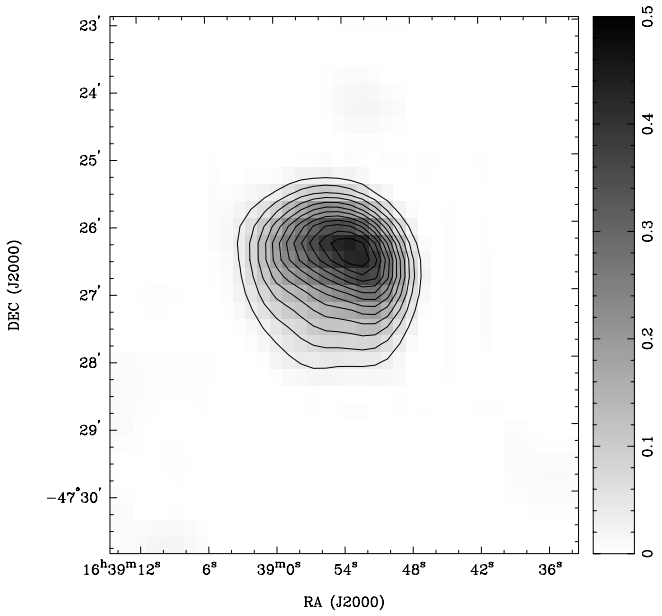

Figure 3.22 The MOST image of G337.4-0.4. Pixel map image: min / max = -0.035 / 0.440; range = 0 to 0.5, Jy/beam (lin). Contour image: contours x 0.034 Jy/beam; contours: 1, 2, 3, 4, 5, 6, 7, 8, 9, 10, 11, 12, 13,14. Beam = $43'' \times 58''$.

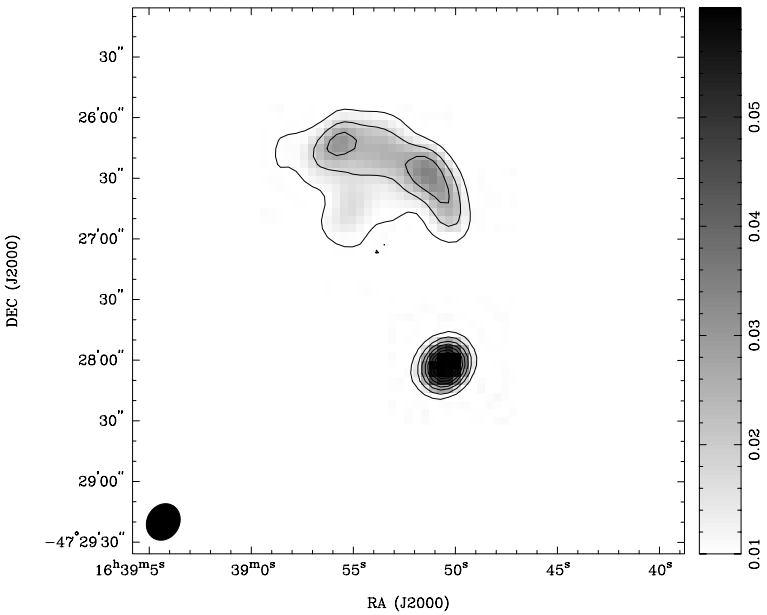

Figure 3.23 The ATCA image of G337.4-0.4. Pixel map image: min / max = -0.01018 / 0.08945; range 0.01 to 0.06 Jy/beam (lin). Contour image: contours x 8.945 x 10^{-4} Jy/beam; contours: 10, 20, 30, 40, 50, 60, 70, 80, 90. The synthesised beam ($18.76'' \times 16.03''$) is shown on the left.

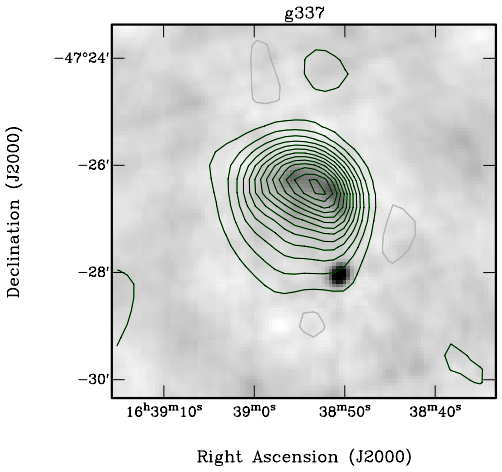

Figure 3.24 The ATCA image (5 GHz) of G337 overlaid on the MOST (843 MHz) radio contours of G337.4-0.4 (contour levels: 10, 40, 70, 100, 125, 150, 175, 225, 250, 300, 340, 390, 420 mJy/beam.

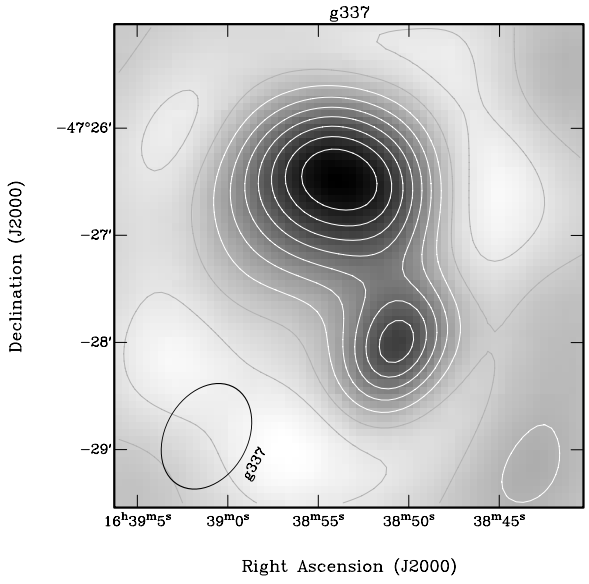

Figure 3.25 The ATCA image (5 GHz) of G337.4-0.4 convolved with the MOST beam (shown on the left). Contour levels: 25, 40, 65, 85, 105, 130 mJy/beam. The point source is clearly visible on this image.

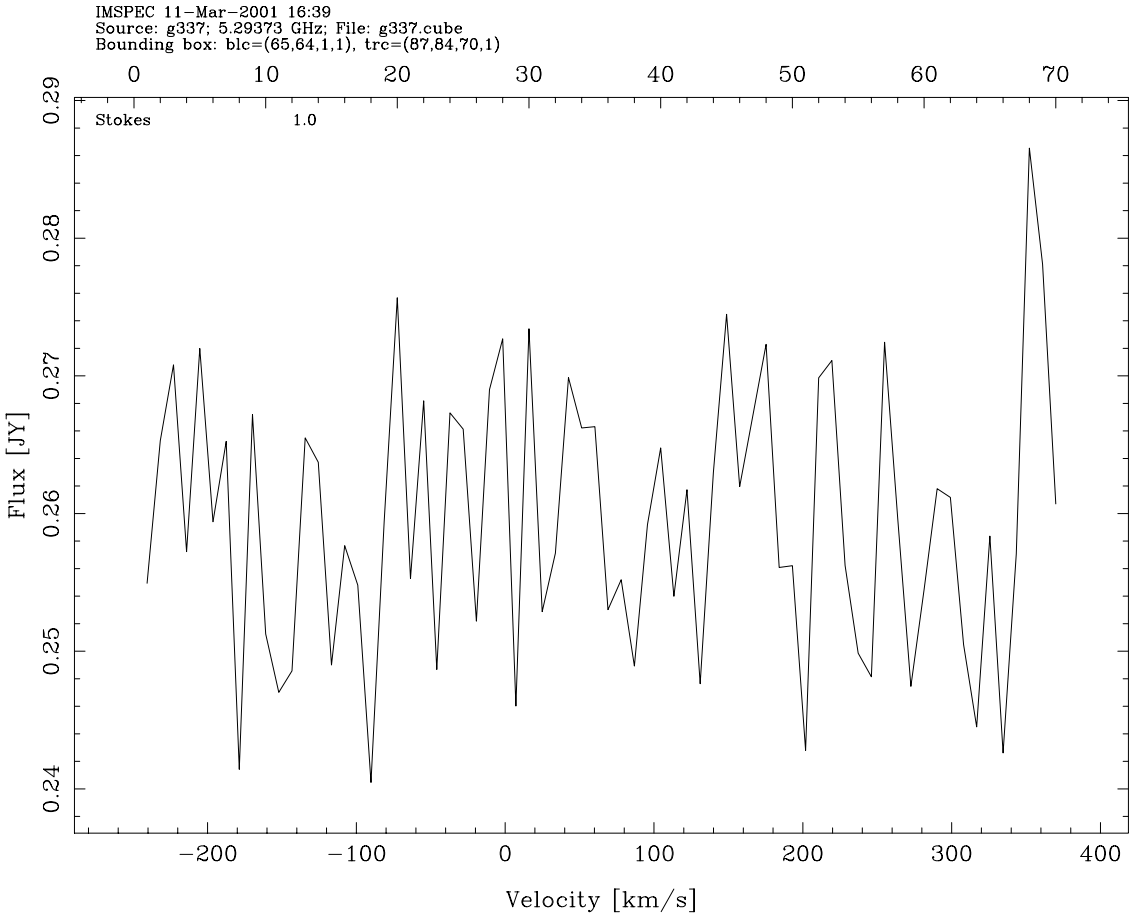

Figure 3.26 Integrated spectrum of G337.4-0.4. No line emission has been detected above the sensitivity limit of 27 mJy or $T_L < 0.10\ T_C$.

3.6.9 G358.6+0.1 (SgrE19)

G358.6+0.1 (SgrE19) is one of the discrete continuum radio sources from the SgrE cluster, believed to lie physically close to the Galactic Centre (Liszt 1992) [65]. Single-dish observations of RRL and molecular lines from this region have revealed emission at approximately -210 km s^{-1} (Caswell and Haynes 1987 [19], Liszt 1992 [65]). The SgrE region has been observed with the VLA in the $H92\alpha$ transition at 8.3GHz and RRL emission has been detected at about -205 km s^{-1} from the majority of the bright sources in the cluster. However, no significant line emission has been detected from SgrE19, in the inspected velocity range of -150 to -250 km s^{-1} (Cram et al. 1996) [28]. However, the ATCA $H107\alpha$ observations made in a considerably wider range of velocities (-300 to $+300$km s^{-1}) reveal a relatively strong radio emission at about 3.2 ± 3.6 km s^{-1}, confirming the thermal nature of this source, which does not seem to belong to the same cluster moving with v = -205 km s^{-1}, as the majority of the sources observed by Cram et al. (1996) [28].

Figure 3.27 shows the MOST image of this source, with the measured integrated flux of 380 mJy at 843 MHz. SgrE19 is only slightly resolved with the peak emission of 367 mJy/beam and the size of $(1.4' \times 0.8')$, determined after fitting the source by a Gaussian.

The ATCA continuum image of SgrE19 (Figure 3.28) has been fitted by a Gaussian with a peak of 147 mJy/beam, with deconvolved major and minor axis of $13.19'' \times 8.01''$. The integrated flux density of 370 mJy (measured from the fully imaged source) suggests a flat spectrum with $\alpha \sim 0$. This is also consistent with the value of 377 mJy at 8.3 GHz, measured by Cram et al. 1996 [28].

The spectrum of SgrE19 (Figure 3.29) shows a strong (38 mJy or 9.6% of the continuum emission) $H107\alpha$ recombination line at a radial velocity of $v_{LSR} = 3.2 \pm 3.6$ km s^{-1} and with a linewidth $\Delta v = 26$ km s^{-1}. Assuming near-LTE conditions, which can be applied to the majority of Galactic HII regions at frequencies $\nu > 1$ GHz (Shaver 1980 [93], Roelfsema and Goss 1992 [82]), the electron temperature of this HII region has been estimated to be about 4300 K. This temperature is considerably below the average temperature, expected in a typical HII region and might be a consequence of the uncertainty of the fitted line parameters, because of the low signal to noise ratio.

The distance to SgrE19, inferred from its radial velocity, in the range from -0.4 to 6.8 km s^{-1}, is less than 1.0 kpc, implying that the source is much closer than the SgrE cluster and not physically associated with this Galactic Centre region HII complex. This also agrees with the result of Liszt (1992) [65], who has imaged the CO molecular emission on the line of sight to SgrE19 at velocities of 0, -17, -50, and -60 km s^{-1}.

Finally, the infrared data is consistent with the ATCA result. The IRAS source 17388-3002, identified with SgrE19 is a strong FIR source (455 Jy) at 60μm, with $S_{60\mu m}/S_{843MHz}$ of 1266, typically associated with compact HII regions (Whiteoak and Green 1996) [126].

The source has been identified with two MSX point sources with the total flux

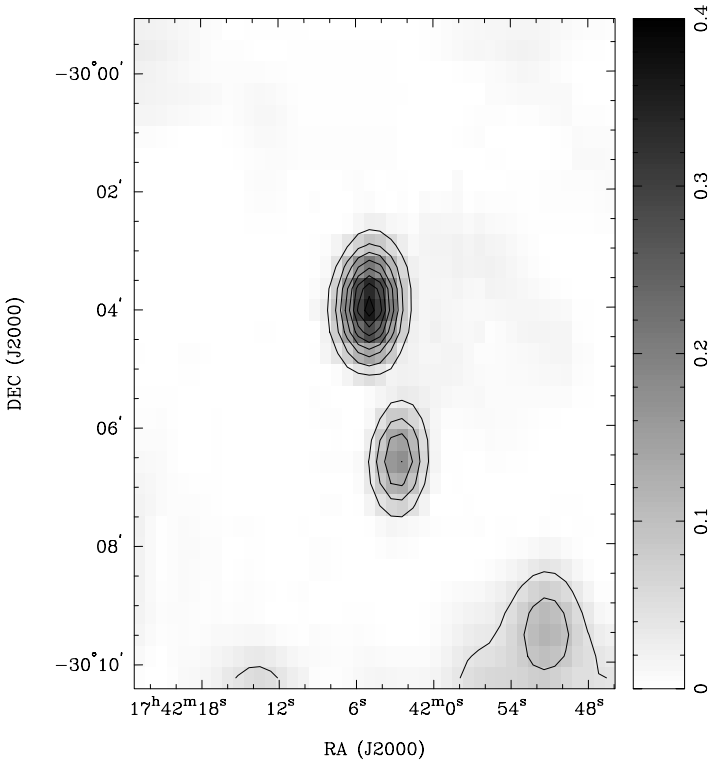

Figure 3.27 The MOST image of SgrE19 [$17^h42^m05^s$ $-30^o04'00''$ (J2000)]. Pixel map image: min / max = -0.02 / 0.36; range = 0 to 0.4, Jy/beam (lin). Contour image: contours x 0.04261 Jy/beam; contours: 1, 2, 3, 4, 5, 6, 7, 8. Beam = $43'' \times 86''$.

density of 2.55 Jy at 8.3μm (Figure 2.12). Comparing the infrared and the 843 MHz radio emission, the ratio $R = S_{8.3\mu m}/S_{843\,\mathrm{MHz}}$ has been calculated to be > 6.7, suggesting a thermal source.

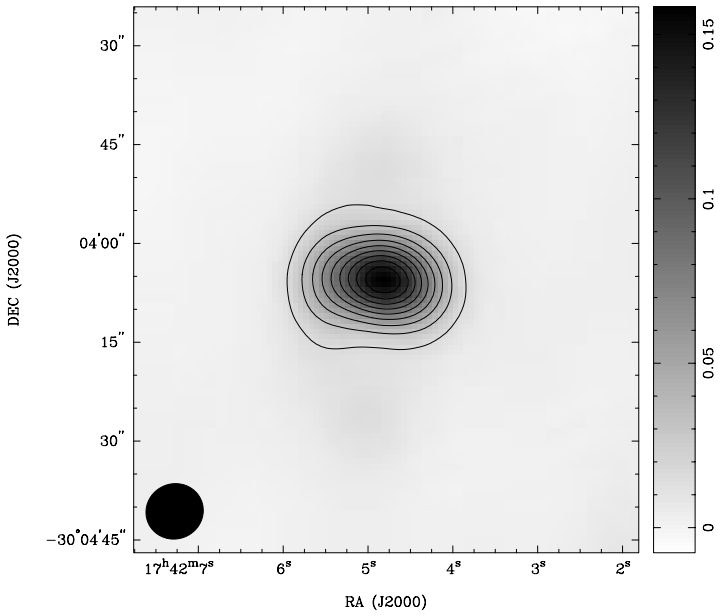

Figure 3.28 The ATCA image of SgrE19. Pixel map image: min / max = -3.21 x 10^{-3} / 0.159; range -7.633 x 10^{-3} / 0.1584 Jy/beam (lin). Contour image: contours x 1.6 x 10^{-3} Jy/beam; contours: 10, 20, 30, 40, 50, 60, 70, 80, 90. The synthesised beam ($8.81'' \times 8.36''$) is shown on the left.

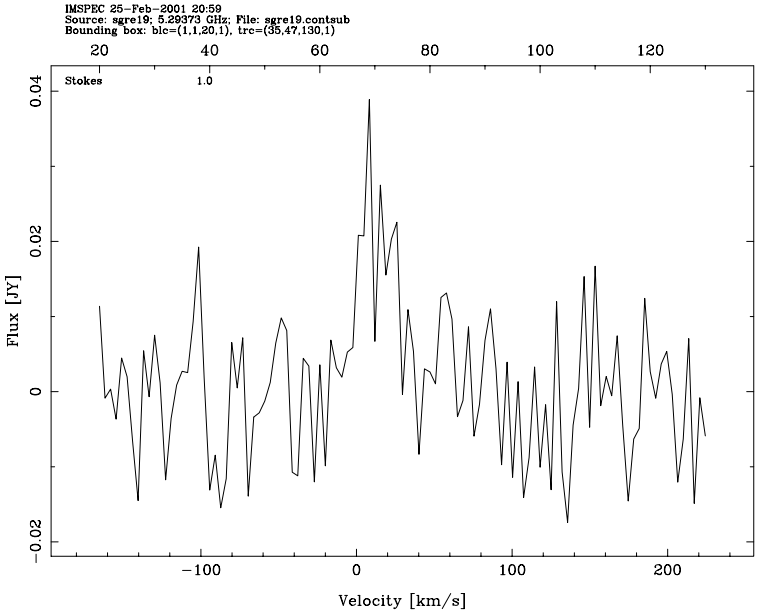

Figure 3.29 Integrated spectrum of SgrE19, after the continuum subtraction, centred in the maximum of the H107α line emission. The line parameters determined after fitting by a Gaussian are listed in Table 3.5.

3.7 The experimental design

The sample of 9 sources selected for this project and imaged with the ATCA at ∼5 GHz in H107α transition, have a wide range of properties. There are extended, low brightness objects as well as bright, only slightly resolved sources. Such a selection has been motivated by the necessity to test and refine parameters of the observation, before proceeding with the experiment and observing a large number of the MGPS sources. As a consequence, the estimated RRL strength of some of the selected sources was below the sensitivity limit of this survey. To image these sources in the RRL the observing technique would need to be modified.

As discussed in Chapter 1, to detect a RRL with a flux density of 2% of the continuum emission signal to noise ratio, before the continuum subtraction, has to be about 150. Hence, to image the extended, low surface brightness sources such as G282.8-1.2, G302.4-0.1, or G304.5-0.1, signal to noise ratio has to be improved by a factor of approximately 10. This can be done by decreasing the resolution (by increasing the value of the synthesised beam width), and/or by decreasing the noise in the single channel image.

Since the flux density per beam area of an extended emission is approximately proportional to the beam area, to increase the signal by a factor of N, the beam size would need to be made $\sqrt{N}$ times larger (by decreasing the array size by a factor of $\sqrt{N}$). Hence, by choosing a more compact array with a lower resolution the flux density per synthesised beam increases.

In addition, the noise in the individual channel image can be reduced by increasing the integration time on each source, and by increasing the channel width. According to 3.3 increasing the observing time and the channel width, each by a factor of N, would reduce the noise in the image by the same factor. However, the choice of the channel width is limited by the design of the ATCA spectral line correlator and also by the required total bandwidth (velocity range). Hence, the width of a single channel can be modified, most easily in imaging, by averaging and smoothing the data.

The selected ATCA configuration (0.750A) with a beam size of approximately 16″ (without antenna 6) is appropriate for imaging of bright (G267.9-1.1) or small, relatively bright sources (SgrE19, G313.8+0.0). However, to image G282.8-1.2, G302.4-0.1, G304.5-0.1 , or similar extended, low brightness sources, a more compact ATCA configuration (for example, 0.375A) would be more suitable. The beam size of the 0.375A array is about 32″ ($2 \times 16''$). Using this array configuration the flux density per beam area would increase by a factor of 4. In addition, by increasing the integration time per source and the channel width, each by a factor of 2−3, the rms noise in the single channel image would be reduced by the same factor. This would increase the signal to noise ratio by a factor of about 10, which would be enough to image low brightness, extended sources such as G282.8-1.2, G302.4-0.1 or G304.5-0.1.

In addition, a more compact array containing short baselines, would detect the extended features of the observed sources. For example, to image a 2′ source the

baselines as short as at least 45 m have to be present in the data and the 0.375A ATCA contains a 31 m baseline.

Chapter 4

Conclusion and suggestions for further work

A sample of 9 small diameter radio sources has been selected from the MGPS (Green et al. 1999) [42] and observed with the ATCA in the H107α transition at 5.92 GHz, in a search for young Galactic SNRs. In radio continuum images of the Galactic Plane, young SNRs are confused with other similar small-diameter compact radio sources, such as Galactic thermal sources (planetary nebulae and HII regions), or extragalactic sources. Since RRL emission is an unambiguous indicator of a thermal source, this method has been used to eliminate HII regions from the selected sample of compact Galactic radio sources. In addition, the IRAS and MSX infrared data have been used to estimate the infrared to radio flux density ratio, commonly used to distinguish thermal and non-thermal sources. The measured flux densities in the continuum at 843 MHz, 5 GHz, and the results of some previous studies, have been used to estimate the spectral indices of some of the selected sources.

One source (G282.8-1.2) has been identified as a possible young Galactic SNRs. This source has a low ratio of far-infrared to radio emission of $R = S_{60\mu m}/S_{1GHz} < 1$, the same value being found in all of the known young Galactic (historical) SNRs (Crab, Tycho, Kepler, CasA). In addition, the estimated spectral index of $\alpha = 0.31$ and a possible x-ray emission suggest that this source could be a small-diameter SNRs. Further studies (eg. polarisation, high-resolution radio observation to determine the morphology, x-ray emission) are needed to confirm this result.

Radio recombination line emission (H107α) has been detected in 3 of the selected sources (G267.9-1.1, G313.8+0.7, G358.6+0.1 (SgrE19)), eliminating them from the sample of SNR candidates. In addition, the properties (electron temperatures, distances, velocities of a turbulent motion within the gas) of these Galactic HII regions have been determined, using the measured line parameters. G267.9-1.1 is an HII region listed in the Catalogue of Southern Galactic HII regions (Caswell and Haynes 1987) [19], and this survey has confirmed the previous results. Previously unclassed sources G313.8+0.7 and G358.6+0.1 (SgrE19) have been included in the sample of Galactic HII regions. Previous RRL observations of SgrE19 (Cram et al. 1996) [28] suggested a possible non-thermal nature of this source. However, the H107α detec-

tion in this survey has classed this source as a Galactic HII region at a distance of < 1 kpc.

The ATCA RRL data are not conclusive for the remaining low brightness, extended sources in this sample. Further studies are needed to determine unambiguously the nature of these sources. However, some of these sources are most likely thermal HII regions: G331.7-0.1 has an approximately flat spectrum estimated from the 843 MHz and 5 GHz data, and $R = S_{60\mu m}/S_{843MHz}$ of 760. There is also a possible (2σ) RRL emission from this source, but the MSX data are inconclusive. Source G323.8+0.0 has also relatively high infrared emission and ratios of the IRAS emission at 12, 25, and 60μm characteristics of HII regions. An extremely high infrared emission of G337.4-0.4 had classed this source as a compact Galactic HII region.

The presented analysis of the ATCA RRL observations of 9 sources, selected for this pilot project has shown that this method can successfully be used to distinguish thermal and non-thermal compact radio sources in the Galactic Plane, in a search for young Galactic SNR candidates. Although, to image a weak RRL emission from low-brightness, extended sources is a challenging task, the selected ATCA configuration (0.750A) was appropriate for imaging of relatively bright, more compact sources. A slightly modified observing technique (the proposed 0.375A ATCA configuration) would successfully image low surface brightness, extended sources similar to G282.8-1.2, G302.4-0.1, or G304.5-0.1.

Radio recombination line studies of compact, small-diameter Galactic radio sources, combined with the available infrared, x-ray, and spectral index data, provide an excellent method to identify non-thermal, small-diameter (young) Galactic SNRs by distinguishing them from thermal Galactic sources (HII regions). There are many more untested small-diameter, compact, (apparent HII regions) in the southern Galactic Plane which are potential small-diameter (young) Galactic SNR. A visual inspection of the 37 MGPS mosaics shows about 4-6 suitable sources per mosaic which means 100-150 SNR candidates. A full project to examine all these sources would include:

- selecting all small-diameter sources from MGPS
- searching the IRAS and MSX catalogues for infrared counterparts and determining FIR/radio and MIR/radio ratios
- searching the x-ray catalogues for possible x-ray counterparts
- selecting all sources with FIR/radio < 500, and all sources with detected x-ray emission
- undertaking ATCA (or VLA) observations of these sources in RRL using a compact array (0.375A) and an integration time of $\sim$300 min per source
- undertaking polarisation imaging at 4 frequencies for the final candidates.

Bibliography

[1] Aller, L.H., Gaseous Nebulae, Chapman and Hall, London 1956

[2] Aller, H.D., Reynolds, S.P., 1985, ApJL, 293L, 73

[3] Altenhoff, W.J., Downes, D., Pauls, T., Schraml, J., 1979, A&AS, 35, 23

[4] Arendt, R.G., 1989, ApJS, 70, 181

[5] Becker, R.H., in: IUA Symp. No 101, Supernova Remnants and their X-Ray emission, J. Danziger and P. Gorenstein (eds.), Reidel, Dordrecht, 1983

[6] Becker, R.H., Helfand, D.J., 1984, ApJ, 283, 154

[7] IRAS Catalogues and Atlases Explanatory Supplement, 1988, ed. Beichman, C., Neugebauer, G., Habing, H.J., Clegg, P.E., Chester T.J., Washington, DC: GPO, NASA RP-1190, vol. 1

[8] Bertola, F., Mammano, A., Perinotto, M., Contr. Osservat. Astrophis. Univ. Padova Asiago, 1965

[9] Blair, W.P., Long, K.S., Vancura, O., 1991, ApJ, 366, 484

[10] Bridle, A.H., Synthesis Observing Strategies, in Synthesis Imaging in Radio Astronomy, eds. R.A. Perley, F.R. Schwab, A.H. Bridle, 1994

[11] Brocklehurst, M., Seaton, M.J., 1972, MNRAS, 157, 179

[12] Brown, R.L., 1980, The Importance of Non-LTE Effects to the Interpretation of Radio Recombination Lines, in Radio Recombination Lines, ed. P.A. Shaver, Reidel, Dordrecht, p53

[13] Brown, R.L., 1987, in Spectroscopy of Astrophysical Plasmas, ed. A. Dalgarno and D. Layzer, Cambridge University Press, Cambridge, p35

[14] Brown, R.L., Lockman, F.J., Knapp, G.R., 1978, Annu. Rev. A&AS., 16, 445

[15] Brown, R.L., Marscher, A.P., 1978, ApJ, 220, 467

[16] Cappellaro, E., Turatto, M., 1988, A&A, 190, 10

[17] Cappellaro, E., Turatto, M., Benetti, S., Tsvetkov, D. Y., Bartunov, O.S., Makarova, I.N., 1993, A&A, 273, 383

[18] Caswell, J.L., Haynes, R.F., Clark, D.H., 1975, AuJPh, 28, 633

[19] Caswell, J.L., Haynes, R.F., 1987, A&A, 171, 261

[20] Chanan, G.A., Helfand, D.J., Spinrad, H., Ebneter, K., 1986, Nature, 320, 41

[21] Chevalier, R.A., 1982, ApJ, 258, 790

[22] Chevalier, R.A., Kirshner, R.P., Raymond, J.C., 1980, AJ, 235, 186

[23] Clark, D.H., Andrews, P.J., Smith, R.C., 1981, Observatory, 101, 203

[24] Clark, D.H., Caswell, J.L. 1976, MNRAS, 174, 267

[25] Clark, D.H., Crawford, D.F., 1974, AuJPh, 27, 713

[26] Clark, D.H., Stephenson, F.R., The Historical Supernovae, Pergamon Press, Oxford, 1977

[27] Cohen, M., Green, A.J., 2001, MNRAS, in press

[28] Cram L.E., Beasley M.J., Gray A.D., Goss W.M., 1996, MNRAS, 280, 1110

[29] Crane, P.C., Napier, P.J., Sensitivity, in Synthesis Imaging in Radio Astronomy, eds. R.A. Perley, F.R. Schwab, A.H. Bridle, 1994, Astronomical Society of the Pacific, San Francisco

[30] Dickel, J.R., Jones, E.M., 1985, AJ, 288, 707

[31] Dickel, J.R., Sault, R., Arendt, R.G., Korista, K.T., Matsui, Y., 1988, ApJ, 330, 254

[32] Downes, D., 1971, AJ, 76, 305

[33] Downes, D., Wilson, T.L., Bieging, J., Wink, J., 1980, A&AS, 40, 379

[34] Egan, M.P., Price, S.D., Moshir, M.M., Cohen, M., Tedesco, E., Murdock T.L., Zweil, A., Burdick, S., Bonito, N., Gugliotti, G.M., Duszlak, J., The Midcourse Space Experiment Point Source Catalogue, Version 1.2 (June 1999), Air Force Research Lab. Technical Rep. AFRL-VS-TR-1999-1522, 1999

[35] Fabbiano, G., Doxsey, R.E., Griffiths, R.E., Johnston, M.D., 1980, AJ Lett. 235, L163

[36] Fich, M., Blitz, L., Stark, A.A, 1989, ApJ, 342, 272

[37] Fürst, E., Reich, W., Sofue, Y., 1987, A&AS, 71, 63

[38] Galas, C.M.F., Venkatesan, D., Garmire, G.P., 1982, ApJL., 22, 103

[39] Gaskell, C.M., Cappellaro, E., Dinerstein, H.L., Garnett, D.R., Harkness, R.P., Wheeler, J.C., 1986, ApJL, 306, L77

[40] Gray, A.D., 1994, MNRAS, 270, 861

[41] Green, A.J., 1974, A&AS Suppl. Ser., 18, 267

[42] Green, A.J., Cram, L.E., Large, M.I., Ye, T. 1999, ApJS 122, 207

[43] Green, D.A., 1984, MNRAS, 209, 449

[44] Green, D.A., 1985, MNRAS, 216, 691

[45] Green, D.A., 1988, Astrophys. Space Sci. 148, 3

[46] Green, D.A., 1989, AJ 98, 1358

[47] Green, D.A., 1991, A&AS, 88, 355

[48] Green, D.A., 2000, A Catalogue of Galactic Supernova Remnants (2000 August version), Mullard Radio Astronomy Observatory, Cavendish Laboratory, Cambridge, United Kingdom (available on the World Wide Web at: http://www.mrao.cam.ac.uk/surveys/snrs/)

[49] Green, D.A., Gull, S.F., 1984, Nature, 312, 527

[50] Goss, W.M., Viallefond, F. J., 1985, A&A, 6, 145

[51] Gregory, P.C., Vavasour, J.D., Scott, W.K., Condon, J.J., 1994, ApJS, 90, 173

[52] Haynes, R.F., Caswell, J.L., Simons, L.W.J., 1979, AuJPA, 48, 1

[53] Helfand, D.J., Becker, R.H., 1987, ApJ, 314, 203

[54] Helfand, D.J., Chance, D., Becker, R.H., White, R.L., 1984, AJ, 89, 819

[55] IRAS catalogues: The Small Scale Structure Catalogue, 1988, eds. G. Helou, D.W. Walker (Washington, DC: GPO), NASA RP-1190 , vol 7

[56] Henbest, S.N., 1980, MNRAS, 190, 833

[57] Hunstead, R.W., 2001, private communication

[58] Kardashew, N.S., 1962, Astron. Zh. 39, 393

[59] Kinugasa, K., Tsunemi, H., 1999, PASJ, 51, 239

[60] Kirshner, R.P., Chevalier, R.A., 1987, A&AS, 67, 267

[61] Klein, U., Emerson, D.T., Haslam, C.G., Salter, C.J., 1979, A&AS, 76, 120

[62] Kleinmann, S.G., Cutri, R.M., Young, E.T., Low, F.J., Gillett, F.C., 1986, Explanatory Supplement to the IRAS Serendipitous Survey Catalogue (Pasadena: JPL)

[63] Koyama, K., Petre, R., Gotthelf, E. V., Hwang, U., Matsura, M., Ozaki, M., Holt, S.S., 1995, Nature, 378, 255

[64] Lang, K., 1974, Astrophysical Formulae (Springer, New York, Heidelberg, Berlin)

[65] Liszt, H.S., 1992, ApJS, 82, 495

[66] Lockman, F.J., Brown, R.L., 1978, AJ, 222, 153

[67] Long, K.S., Blair, W.P., van den Bergh, S., 1988, ApJ, 333, 749

[68] Lozinskaya, T.A., 1980, Astron. Zh. 57, 707

[69] Lozinskaya, T.A., 1992, Supernovae and Stellar Wind in the Interstellar Medium (New York: AIP)

[70] Mathewson, D.S., Ford, V.L., Tuohy, I.R., Mills, B.Y., Turtle, A.J., Helfand, D.J., 1985, ApJS, 58, 197

[71] McKee, C.F., Cowie, L.L., 1975, AJ, 195, 715

[72] Menzel, D.H., 1937, AJ, 85, 330

[73] Mezger,P.G., Henderson, A.P., 1967, AJ, 147, 471

[74] Mills, B.Y., Turtle, A.J., Little, A.G., Durdin, J.M., 1984, AuJPh, 37, 321

[75] Milne, D.K., 1970, AuJPh, 23, 425

[76] Oemler, a., Tinsley, B.M., 1979, AJ, 84, 985

[77] Osterbrock, D.E., Astrophysics of Gaseous Nebulae, Freeman, San Francisco, 1974

[78] Pskovskii, Y.P., in: Neutrinos 77, Vol.1, Nauka, Moscow, 1978

[79] Pye, J.P., Pounds, K.A., Rolf, D.P., Smith, A., Willingale, R., Seward, F.D., 1981, MNRAS, 194, 569

[80] Reich, W., Fürst, E., Altenhoff, W. J., Reich, P., and Junkes, N. 1985, A&AS, 151, L10

[81] Rodgers, A.W., Campbell, C.T., Whiteoak, J.B., 1960, MNRAS, 121, 103

[82] Roelfsema, P.R., Goss, W.M., 1992, A&AS Rev., 4, 161

[83] Roger, R.S., Milne, D.K., Kesteven, M.J., Wellington, K.J., Haynes, R.F., 1988, ApJ, 332, 940

[84] Rohlfs, K., Tools of Radio Astronomy, Springer-Verlag, Berlin, Heidelberg, New York, 1986

[85] The Second ROSAT Source Catalogue of Pointed Observations, ROSAT Consortium, ROSAT News 72, 25/5/2000

[86] Rybicki, G.B., Lightman, A.P., Radiative Processes in Astrophysics, Wiley, New York, 1979

[87] Salem, M., Brocklehurst, M, 1979, AJ Suppl. Ser., 39, 633

[88] Sault, R., Killeen, N., Miriad Users Guide, 1998

[89] Schmidt, M., in Galactic Structure, eds. A. Blauuv, M. Schmidt, Univ. Chicago Press, 1965

[90] Seaton, M.J. Theory of Recombination Lines, in Radio Recombination Lines, ed. P.A. Shaver, Reidel, Dordrecht, 1980

[91] Sgro, A.C., 1975, AJ, 197, 621

[92] Shaver, P.A., 1979, A&AS, 78, 116

[93] Shaver, P.A., ed. Radio Recombination Lines, Reidel, Dordrecht, 1980

[94] Shaver, P.A., McGee, R.X., Newton, L.M., Danks, A.C., Pottasch, S.R., 1983, MNRAS, 204, 53

[95] Shklovskii, I.S., 1960, Astron. Zh., 37, 369

[96] Shklovskii, I.S., Supernovae and Related Problems, Nauka, Moscow, 1976

[97] Shklovskii, I.S., 1984, Adv. Space Rev. 3, 241

[98] Smith, A., Davelaar, J., Peacock, A., Taylor, B.G., Morini, M., Robba, N.R., 1988, AJ, 325, 288

[99] Sramek, R.A., Cowan, J.J., Roberts, D.A., Goss, W.M., and Ekers, R.D. 1992, AJ, 104, 704

[100] Sramek, R.A., Schwab, F.R., Imaging, in Synthesis Imaging in Radio Astronomy, eds. R.A. Perley, F.R. Schwab, A.H. Bridle, 1994, Astronomical Society of the Pacific, San Francisco

[101] Staveley-Smith, L., Manchester, R.N., Kesteven, M.J., Reynolds, J.E., Tzioumis, A.K., Killen, N.E.B., Jauncey, D.L., Campbell-Wilson, D., Crawford, D.F., Turtle, A.J., 1992, Nature, 355, 147

[102] Stephenson, F.R., Clark, D.H., Crawford, D.F., 1977, MNRAS, 180, 567

[103] Strom, R.G., Goss, W.M., Shaver, P.A., 1982, MNRAS, 200, 473

[104] Strom, R.G., Sutton, J., 1975, A&AS, 42, 299

[105] Subrahmanyan, R., Ekers, R.D., Wilson, W.E., Goss, W.M., Allen, D.A., 1993, MNRAS, 263, 868

[106] Tammann, G.A., Supernovae and Supernova Remnants, Reidel, Dordrecht, 1977

[107] Tammann, G.A., in: Supernovae: A Survey of Current Research, M.J. Rees and R.J. Stoneham (eds.), Reidel, Dordrecht, 1982

[108] Tammann, G.A., Loeffler, W., Schroeder, A., 1994, ApJS, 92, 487

[109] Tanimory, T., Hayami, Y., Kamei, S., Dazeley, S.A., Edwards, P.G., Gunji, S., Hara, S., Hara, T., Holder, J., Kawachi, A., Kifune, T., Kita, R., Konishi, T., Masaike, A., Matsubara, Y., Matsuoka, T., Mizumoto, Y., Mori, M., Moriya, M., Muraishi, H., Muraki, Y., Naito, T., Nishijima, K., Oda, S., Ogio, S., Patterson, J.R., Roberts, M.D., Rowell, G.P., Sakurazawa, K., Sako, T., Sato, Y., Susukita, R., Suzuki, A., Suzuki, R., Tamura, T., Thornton, G.J., Yanagita, S., Yoshida, T., Yoshikoshi, T., 1998, ApJL, 497L, 25

[110] Taylor, A.R., Goss, W.M., Coleman, P.H., van Leeuwen, J., Wallace, B.J., 1996, ApJS, 107, 239

[111] Tuohy, I.R., Nugent, J.J., Garmire, G.P., Clark, D.H., 1979, Nature, 279, 139

[112] van den Bergh, S., 1976, ApJL, 208L, 17

[113] van den Bergh, S., Maza, J., 1976, ApJ, 204, 519

[114] van den Bergh, S., in: ESO Workshop on the SN 1987; ESO Conference and Workshop Proceedings No. 26, I.J. Danziger (ed.), 1987

[115] Vartanian, M.N., Lum, R.S.R., Ku, W.H.M., 1985, ApJL, 288, L5

[116] Velusamy, T., 1984, Nature, 308, 251

[117] Velusamy, T., 1985, MNRAS, 212, 359

[118] Voges W., Aschenbach, B., Boller, T., Braeuniger, H., Briel, L., Burkert, W., Dennerl, K., Englhauser, J., Gruber R., Haberl, F., Hartner, G., Hasinger G., Pfeffermann, E., Pietsch, W., Predehl, P., Schmitt, J., Trumper, J., Zimmermann, U., 1999, A&A, 349, 389

[119] Voges W., Aschenbach, B., Boller, T., Braeuniger, H., Briel, L., Burkert, W., Dennerl, K., Englhauser, J., Gruber R., Haberl, F., Hartner, G., Hasinger G., Pfeffermann, E., Pietsch, W., Predehl, P., Schmitt, J., Trumper, J., Zimmermann, U., 2000, ROSAT All Sky Survey Faint Source Catalogue, IAUC, 7432, 3

[120] Weiler, K.W., Sramek, R.A., 1988, ARA&A, 26, 295

[121] Weisskopf, M.C., Silver, E.H., Kestenbaum, H.L., Long, K.S., Novick, R., 1978, ApJL, 220, L117

[122] Weisskopf, M.C., Hester, J.J., Tennant, A.F., Elsner, R.F., Schulz, N.S., Marshall, H.L., Karovska, M., Nichols, J.S., Swartz, D.A., Kolodziejczak, J.J., O'Dell, S.L., 2000, ApJL, 536L, 81

[123] Wheelock, S., Gautier, III., Chillemi, J., Kester, D., McCallon, H., Oken, C., White, J., Gregorich, D., Boulanger, F., Good, J., Chester, T., 1991, IRAS Sky Survey Atlas Explanatory Supplement, JPL Publication 94-11 (Pasadena: JPL)

[124] White, R.L., Long, K.S., 1983, ApJ, 264, 196

[125] Whiteoak, J.B.Z., Cram, L.E., Large, M.I., 1994, MNRAS, 269, 294

[126] Whiteoak, J.B.Z., Green, A.J., MOST Supernova Remnant Catalogue, 1996, A&AS, 118, 329 (http://www.physics.usyd.edu.au/astrop/wg96cat)

[127] Wood, D.O.S., Churchwell, E., 1989, ApJS, 69, 831

[128] Wright, A.E., Griffith, M.R., Burke, B.F., Ekers, R.D., 1994, ApJS, 91, 111

Appendix A

RRL emission from HII regions

A.1 Equation of radiative transfer

The equation of radiative transfer describes the change of *specific intensity* I_ν or *brightness* from a distant source. This change occurs because of absorption or emission along the line of sight. The equation of transfer is usually given as:

$$\frac{dI_\nu}{ds} = -\kappa_\nu I_\nu + \epsilon_\nu, \tag{A.1}$$

where κ_ν and ϵ_ν are coefficients of absorption and emission, respectively, which depend on the properties of the emitting material.

The solution of the differential equation (A.1) is especially simple in several limiting cases one of which is complete equilibrium of the radiation with its surrounding, $dI_\nu/ds = 0$. In this case the brightness distribution is described by the *Planck function* of the thermodynamic temperature of the surroundings *(Black-body radiation)*:

$$I_\nu = B_\nu(T) = \epsilon_\nu/\kappa_\nu, \tag{A.2}$$

where the Planck function is defined as:

$$B_\nu(T) = \frac{2h\nu^3}{c^2} \cdot \frac{1}{e^{h\nu/kT} - 1} \tag{A.3}$$

and gives the power per unit frequency interval, per unit area, and per unit solid angle. The second equality of (A.2), implied by the fact that in thermal equilibrium the intensity is given by the Planck function, holds more generally (Kirchoff's law).

Defining the *optical depth* $d\tau_\nu$ by

$$d\tau_\nu = -\kappa_\nu ds \tag{A.4}$$

the equation of transfer (A.1) can be written as

$$-\frac{1}{\kappa_\nu} \cdot \frac{dI_\nu}{ds} = \frac{dI_\nu}{d\tau_\nu} = I_\nu - B_\nu(T). \tag{A.5}$$

Assuming that the medium is isothermal, (T = constant) and since s and τ increase in opposite directions, the solution of (A.5) is given as:

$$I_\nu(s) = I_\nu(0)e^{-\tau_\nu(0)} + B_\nu(T)(1 - e^{-\tau_\nu(0)}). \quad (A.6)$$

For a large optical depth, $\tau_\nu(0) \to \infty$ (optically thick case), the observed brightness is equal to the Planck black-body brightness distribution, $I_\nu = B_\nu(T)$.

A.2 Rayleigh-Jeans law and the brightness temperature

In radio-frequency region $h\nu \ll kT$ and Planck function (A.3) can be approximated as:

$$B(\nu, T) = \frac{2\nu^2}{c^2}kT. \quad (A.7)$$

This expression *(the Rayleigh-Jeans law)* can be used for most thermal radio sources except for low-temperature objects in the millimetre wavelength range. The temperature which would result in the given brightness if inserted into (A.7):

$$T_b = \frac{c^2}{2k\nu^2}B_\nu \quad (A.8)$$

is called *the brightness temperature* and used to measure the brightness of an extended radio source. The brightness temperature gives the thermodynamic temperature of the source, which is independent of the frequency if B_ν is emitted by a black body. If there are some other processes responsible for the emission of the radiation the brightness temperature T_b will depend on the frequency.

Introducing the concept of brightness temperature into the equation of radiative transfer the solution for isothermal medium (A.6) becomes:

$$T_b(s) = T_b(0)e^{-\tau_\nu(0)} + T(1 - e^{-\tau_\nu(0)}). \quad (A.9)$$

Assuming that $T_b(0) = 0$ there are two limiting cases:

- $T_b = \tau_\nu T$, for optically thin case $\tau \ll 1$ and,
- $T_b = T$, for optically thick case $\tau \gg 1$.

A.3 Equation of radiative transfer for line emission

In the conditions of *local thermodynamic equilibrium* (LTE) the intensities of emitted and absorbed radiation are related to each other by (A.2). This applies not only for continuous radiation but is also valid for line emission. There are three different processes contributing to the intensity I_ν of the line emission:

- *spontaneous emission* - the result of atoms returning spontaneously from the energy level E_k to the energy level E_n ($k > n$), with probability A_{kn},
- *absorption* - the result of transitions from E_n to E_k, with probability B_{nk}, and
- *stimulated emission* - resulting from transitions from E_k to E_n, with probability B_{kn}.

The coefficients A_{kn}, B_{nk}, and B_{kn} are called *the Einstein coefficients.*

The Einstein coefficients are related to each other in a system in full thermodynamic equilibrium if the number of absorbed and emitted photons are equal (stationary state):

$$g_n B_{nk} = g_k B_{kn} \tag{A.10}$$

$$A_{kn} = \frac{8\pi h\nu^3}{c^3} \cdot B_{kn} \tag{A.11}$$

Using the Einstein coefficients the equation of transfer for the line emission can be written as:

$$\frac{dI_\nu}{ds} = -\frac{h\nu}{c}(N_n B_{nk} - N_k B_{kn}) I_\nu \varphi(\nu) + \frac{h\nu}{4\pi} N_k A_{kn} \varphi(\nu), \tag{A.12}$$

assuming complete redistribution. Comparing this with the equation of transfer (A.1) the coefficients of absorption and emission for line emission can be written as:

$$\kappa_\nu = \frac{h\nu}{c} N_n B_{nk} (1 - \frac{g_n N_k}{g_k N_n}) \varphi(\nu) \tag{A.13}$$

and

$$\epsilon_\nu = \frac{h\nu}{4\pi} N_k A_{kn} \varphi(\nu) \tag{A.14}$$

using the relationship between the Einstein coefficient given in (A.10). The term in brackets in (A.13) is the correction for stimulated emission.

Assuming the condition of LTE, the absorption coefficient becomes:

$$\kappa_\nu = \frac{c^2 g_k}{8\pi\nu^2 g_n} N_n A_{kn} (1 - e^{-\frac{h\nu}{kT}}) \varphi(\nu). \tag{A.15}$$

In this case the stimulated emission cancels most of the absorption in the radio range.

A.4 Line intensity under conditions of LTE

To find the intensity of a RRL under LTE conditions the absorption coefficient (A.15)) has to be calculated. This is done by putting $g_n = 2n^2$, for the statistical weight of the level n, and $A_{n+1,n} = (5.36 \cdot 10^9)/n^5) s^{-1}$ for the transition probability[1] for hydrogen into (A.15). In addition, the density of atoms in the state n is assumed

[1] This probability has been determined by many authors eg. Lang 1974 [64].

to be given by the Saha-Boltzman equation. The optical depth in the centre of a line is now calculated to be:

$$\tau_L = 1.92 \cdot 10^3 (\frac{T_e}{K})^{-5/2} (\frac{EM}{cm^{-6} \cdot pc}) (\frac{\Delta\nu}{kHz})^{-1}. \quad (A.16)$$

For optically thin case the brightness temperature is $T_L = \tau_L T_e$, and hence:

$$T_L = 1.92 \cdot 10^3 (\frac{T_e}{K})^{-3/2} (\frac{EM}{cm^{-6} \cdot pc}) (\frac{\Delta\nu}{kHz})^{-1}. \quad (A.17)$$

A.5 Line intensity under non-LTE conditions

The ratio of the optical depth for two RRLs, which have approximately the same frequency but correspond to different quantum levels is:

$$\frac{\Delta\nu T_L}{\Delta\nu^1 {T_L}^1} = \frac{g_k A_{ki}}{{g_k}^1 {A_{ki}}^1} \quad (A.18)$$

using the expression for the line optical depth (A.15) and the Boltzmann distribution, which holds under LTE conditions. The right-hand side of this equation can be computed theoretically, while the left-hand side contains only observable quantities. If the observations give a result that is not in agreement with the theory then LTE does not apply. However, a different combination of non-LTE effects can force the fulfilment of (A.24), as discussed by Seaton (1980) [90].

Deviations from LTE will affect the RRL radiation, which is expressed by *the departure coefficients b_n and β*, introduced by Menzel (1937) [72] and defined as:

$$b_n = \frac{N_n}{{N_n}^*} \quad (A.19)$$

and

$$\beta = 1 - 20.836 (\frac{T_e}{K}) (\frac{\nu}{GHz})^{-1} \frac{dlnb_n}{dn} \Delta n, \quad (A.20)$$

where ${N_n}^*$ is level population for LTE, N_n the actual population of level n, and k is the principal quantum number of the upper level. Coefficients of absorption κ_ν, and emission ε_ν can now be written as:

$$\kappa_\nu = {\kappa_\nu}^* b_k \beta \quad (A.21)$$

and

$$\varepsilon_\nu = b_k {\varepsilon_\nu}^* \quad (A.22)$$

where subscript * denotes LTE conditions.

The departure coefficients have been tabulated by Salem and Brocklehurst (1979) [87] and Brown (1987) [13] for a broad range of densities and temperatures as found in HII regions. The departure coefficient b_n for most densities is close to the LTE value

1, while β can attain large negative values, which mainly depend on the density of the ionised gas.

Substituting these values for coefficients of absorption and emission into the equation of transfer and making appropriate approximations and simplifying assumptions, it is possible to derive:

$$\frac{r}{r^*} = \frac{T_L}{T_L{}^*} = b_k(1 - \frac{1}{2}\tau_c\beta) \tag{A.23}$$

where $r = T_L/T_c$ and $r^* = T_L{}^*/T_c$ are *line to continuum ratios* for non-LTE and LTE conditions, respectively.

In order to apply these concepts to the real measurements the departure coefficients for sa given HII region must be known, which requires the investigations of all important processes affecting the level population such as radiative capture cascade down to the ground level, collisional excitation and de-excitation, collisional ionisation and three-body recombination etc.

The relative importance of non-LTE effects, pressure broadening and non-zero optical depth has been discussed by Roelfsema and Goss (1992) [82]: the non-LTE effect is almost completely counteracted by pressure broadening so that RRL radiation appear to be emitted under near-LTE conditions. In addition, for the 5 orders of magnitude range in emission measures[2] observed in the majority of the galactic HII regions RRLs at frequencies $\nu \geq 1\ GHz$ are, in fact, emitted under near-LTE conditions (Shaver 1980) [93] and no non-LTE correction needs to be applied to obtain physical parameters from the observed line radiation.

[2]Typically, $EM = 10^3 - 10^8\ pc\ cm^{-6}$